LIQUID SODIUM HEAT TRANSFER BEHAVIOR AND INSTRUMENTATION TECHNIQUES IN PROTOTYPIC SODIUM FAST REACTOR SYSTEMS

By

Nicholas James Thoreson

A dissertation submitted in partial fulfillment of

the requirements for the degree of

Doctor of Philosophy

(Nuclear Engineering & Engineering Physics)

at the

UNIVERSITY OF WISCONSIN–MADISON

2026

Date of final oral examination: April 29th, 2026

This dissertation is approved by the following members of the Final Oral Committee:

Mark H. Anderson, Professor, Mechanical Engineering
Gregory F. Nellis, Professor, Mechanical Engineering
Ben A. Lindley, Assistant Professor, Nuclear Engineering and Engineering Physics
Riccardo Bonazza, Professor, Mechanical Engineering
Paul P.H. Wilson, Professor, Nuclear Engineering and Engineering Physics

Executive Summary

Understanding and predicting heat transfer behavior in liquid metal systems is a critical requirement for the design and analysis of sodium fast reactor (SFR) core assemblies and other heat transfer components. However, the unique thermal transport properties of liquid metals, characterized by their extremely low Prandtl numbers, introduce challenges in first-principles predictions, experimental measurement, and modeling for design decisions. This dissertation addresses these challenges through the development of advanced temperature measurement techniques, the generation of high-resolution experimental data, and the integration of computational modeling to interpret and support observed thermal and heat transport behavior.

A central component of this work is the development and implementation of distributed fiber optic temperature sensor (FOTS) fabrication and deployment methods for use in high temperature liquid sodium environments. Novel fabrication and installation techniques were established to use FOTSs in and around a prototypic wire wrapped fuel pin simulator; including integration within a helical hollow “wire wrap” capillary tube, embedding within the heater rod, and placement across the surrounding annular sodium flow channel. These methods enabled temperature measurements with a spatial resolution of 2.6 mm in both the solid and fluid domains, while maintaining compatibility with high temperature sodium operation.

Using this instrumentation, a comprehensive experimental investigation of liquid sodium heat transfer was conducted around a geometry representative of SFR fuel elements. Measurements were obtained over Peclet numbers ranging from approximately 40 to 400, capturing detailed axial and radial temperature distributions within the sodium flow as well as temperature variations along the helical wire wrap path. The resulting dataset provides a level of spatial detail not typically available in liquid metal heat transfer experiments. Analysis of the

measured temperature profiles showed that local temperature variations arise from geometric effects, variable internal conduction pathways, and measurement location uncertainty. Despite these local features, it was demonstrated that the overall heat transfer behavior can be reliably characterized through appropriate spatial averaging, with resulting Nusselt numbers in good agreement with established correlations, including those of Seban & Shimazaki and Bailey [1], [2], [3], [4].

These experimental findings motivated further analysis using computational fluid dynamics (CFD) to better interpret the measured temperature fields. A full scale CFD model of the test section was created using Reynolds-averaged Navier-Stokes (RANS) methods, and the results were found to be in good agreement with experimental temperature measurements. The simulations provide important insight into the physical meaning of the measured temperatures, demonstrating that the temperature recorded within the hollow wire wrap corresponds closely to a local circumferentially averaged surface temperature of the fuel pin simulator. In addition, the modeling results show that positional variability of the fiber optic sensor within the wire wrap can produce temperature variations partially representative of those observed experimentally, supporting the interpretation that the measured fluctuations arise from physical solid conduction effects rather than measurement error.

In parallel with the heat transfer investigation, a hydraulic characterization of the same geometry was performed through pressure drop measurements of liquid sodium flow around the wire wrapped fuel pin simulator as a secondary objective of this research. A friction factor dataset was developed and used to construct a correlation for this geometry. Comparison with established correlations for annular channels and wire wrapped bundles showed that the measured behavior falls between these limiting cases, as expected. Implementation of the

resulting correlation in the Pronghorn SC system analysis code demonstrated modest sensitivity of predicted assembly pressure drop for a representative reactor configuration, providing additional context for hydraulic modeling of SFR systems.

Taken together, this work demonstrates the value of combining advanced instrumentation, high-resolution experimental measurements, and computational modeling to improve understanding of liquid metal heat transfer as it applies to SFR design and development. The experimental dataset generated in this work provides a high-fidelity resource for validation of computational models, while CFD analysis supports interpretation of the measurements and evaluation of the modeling techniques themselves. These results contribute to improved predictive capability for heat transfer and flow behavior in wire wrapped fuel assemblies and related sodium heat transfer systems, supporting the design and analysis of advanced nuclear power plants and informing ongoing and future experimental investigations at larger scales.

Acknowledgements

Financial support for this work was provided by TerraPower LLC subject to DOE cooperative agreement No. DE-NE0009054 and in part by the Department of Energy Office of Nuclear Energy (DOE-NE) Nuclear Energy University Program (NEUP) under Award Number DE-NE0008902, project 19-16811, along with support from the DOE-NE University Nuclear Leadership Program (UNLP) graduate fellowship. This work also made use of Idaho National Laboratory's High Performance Computing systems located at the Collaborative Computing Center and supported by the Office of Nuclear Energy of the U.S. Department of Energy and the Nuclear Science User Facilities under Contract No. DE-AC07-05ID14517. The views and

opinions of the author expressed herein do not necessarily state or reflect those of the United States Government or any agency thereof.

I would like to thank Professor Mark Anderson for his advice and support as a research mentor, teacher, advisor, and lab director throughout my time as an undergraduate and graduate student in the Thermal Hydraulics Laboratory. I would also like to extend special thanks to Paul Brooks. Without his extensive practical engineering knowledge, help with design and fabrication, and willingness to share his time and perspective when challenges arose, this research would not have been possible.

I am also thankful for my colleagues and friends in UW-Madison's THL for their support and extremely generous help with fabrication and operation of experimental facilities and instruments: Caleb Simons, Dr. Alastair Luna, Dr. Tiago Moreira, Dr. Ian Jentz, Seth Jones, and many others not listed here.

The assistance of Dr. Darius Lisowski at Argonne National Laboratory with the wire wrapping of the simulated sodium fast reactor fuel rod used in this work was much appreciated as was the mentorship and generosity of Dr. Mauricio Tano Retamales and Dr. Piyush Sabharwall during my internship at Idaho National Laboratory. I would also like to thank my collaborators at Oregon State University: Prof. Guillaume Mignot, Hugo Barthod, and Stefan Vietz, whose work developing computational fluid dynamics models of my experimental test section was indispensable.

Finally, I would like to thank Dr. Shaun Aakre, Dr. Karl Britsch, and Professor Wendy Crone for their mentorship and advice during my time as an undergraduate student getting started in engineering research.

Nomenclature

Symbols

A, B, C	Correlation coefficients
A_{cs}	Cross-sectional area
A_{c1}	Interior bundle channel cross-sectional area
Adj	Spectral shift keying adjustment parameter [GHz]
A_f	Flow area
B	Magnetic field magnitude
b	Correlation coefficient
C_{fT1}	Friction factor correlation coefficient for interior bundle channels
D, d	Diameter
$d_{ann,inner}$	Annulus inner diameter
$d_{ann,outer}$	Annulus outer diameter
D_e	Hydraulic diameter
f	Darcy friction factor
f_{T1}	Friction factor for interior bundle channel with turbulent flow
g	Gravitational acceleration
H	Wire wrap pitch
h	Heat transfer coefficient
k	Thermal conductivity
K_f	Thermal conductivity of the fluid
K_1, K_2, K_3, K_4	Electromagnetic flow meter coefficients
L	Length between differential pressure taps
ln	Natural logarithm
$\log_{10}$	Base 10 logarithm
$\dot{m}$	Mass flow rate
μ	Dynamic viscosity
Nu	Nusselt number
[Oxygen]	Dissolved oxygen limit in sodium in weight parts per million
P	Pressure or hexagonal rod bundle pin pitch
ΔP	Pressure difference
Pe	Peclet number
per_{w1}	Wetted perimeter for interior bundle friction factor correlations
$\dot{q}$	Heat transfer rate
$\dot{q}''$	Heat flux
$\dot{q}_{avg}$	Average heat transfer rate
Re	Reynolds number
ρ	Density
S	Spectral shift [GHz]
σ	Standard uncertainty
σ_{refTC}	Standard uncertainty of the calibration reference thermocouple
T	Temperature [ºC]
ΔT	Temperature difference
T_{bulk}	Bulk mean fluid temperature or mixing cup temperature

T_{cal}, T_{uncal}	Calibrated and uncalibrated temperature measurement
T_{in}/T_{inlet}, T_{out}/T_{outlet}	Test section inlet and outlet sodium temperature
T_0, T_{key}	Fiber optic temperature sensor key/rekey temperature
T_{room}	Room temperature
T_{sat}	Saturation temperature [K] for given oxygen concentration in sodium
T_{surf}, $T_{surface}$	Surface temperature
T_{WW}, $T_{wire\ wrap}$	Wire wrap fiber optic temperature sensor temperature
u	Velocity
u_{mean}	Mean velocity
V	Voltage/potential
$\dot{V}$	Volumetric flow rate
V_{cal}, V_{uncal}	Calibrated and uncalibrated voltage/potential/signal measurement
h	Heat transfer coefficient
z_{HL}	Upward axial coordinate indexed at beginning of heated length

Abbreviations

AC	Alternating current
ANL	Argonne National Laboratory
CFD	Computational fluid dynamics
CFM	Coriolis flow meter
DAQ	Data Acquisition System
DC	Direct current
DBHE	Diffusion-bonded heat exchanger
DOE	United States Department of Energy
DOE-NE	United State Department of Energy Office of Nuclear Energy
DNS	Direct Numerical Simulation
EBR-II	Experimental Breeder Reactor-II
EMFM	Electromagnetic flow meter
FFTF	Fast Flux Test Facility
FOTS	fiber optic temperature sensor
ID	Inside diameter
IFR	Integral fast reactor
IHX	Intermediate heat exchanger
INL	Idaho National Laboratory
LES	Large Eddy Simulation
LWR	Light water reactor
NEUP	Nuclear Energy University Program
OD	Outside diameter
OFDR	Optical Frequency Domain Reflectometry
OSU	Oregon State University
PCHE	Printed circuit heat exchanger
PRT	Platinum resistance thermometer
PWR	Pressurized water reactor
RANS	Reynolds-Average Navier-Stokes
RMSE	Root mean square error

SFR	Sodium Fast Reactor
SHTL	Sodium Heat Transfer Test Loop
TC	Thermocouple
TFOTS	Transverse fiber optic temperature sensor
THL	Thermal Hydraulics Laboratory
UCTD	Upgraded Cheng and Todreas correlation
UNLP	University Nuclear Leadership Program
UW, UW-Madison	University of Wisconsin - Madison
VFM	Venturi flow meter
VSFM	Vortex shedder flow meter

List of Figures

List of Tables

Table of Contents

Chapter 1 – Introduction & Research Motivation

Global electricity demand continues to grow as economic development accelerates, and energy access expands worldwide. Sustained economic growth, increasing electrification of transportation and industry, and rising standards of living all contribute to a long-term increase in electricity consumption. Meeting this demand requires reliable and affordable electricity generation technologies capable of operating at large scales while maintaining stable and resilient power systems.

Nuclear power already provides a substantial portion of global low carbon electricity and remains one of the few technologies capable of delivering continuous, large scale, power generation without greenhouse gas emissions and a relatively small land footprint. As concerns over climate change and land use intensify, nuclear energy has the potential to expand its role in the future electricity grid. When the true environmental and societal costs of fossil fuel consumption, called negative externalities in environmental economics, are properly accounted for, low-carbon technologies such as nuclear become significantly more competitive with conventional fossil fuels [1], [2].

The future growth of nuclear power may also depend on continued improvements in reactor technology and public confidence in nuclear power plant reliability and safety. Very few new large light water reactors (LWRs) have been constructed in the United States over the past ~40 years, partially due to the construction cost and schedule overruns that have plagued these large gigawatt-scale plant projects. Emerging (or re-emerging) reactor designs and innovative technologies offer the opportunity to address these concerns, allowing new nuclear generating stations to be inherently safer and more adaptable to modern market demands while expanding nuclear generation to meet global demand for reliable low-carbon electricity.

Several such *advanced* or *Gen IV* designs have been identified, namely, through the Gen IV International Forum, initiated in January 2000. These reactor designs seek to address some of the weaknesses associated with existing commercial light water reactor plants and exploit new markets and applications in various ways. Broadly, many Gen IV reactor concepts prioritize smaller scales with lower capital costs of construction, modularity (flexibility in sizing), load following capability, inherent safety features, and fuel cycles that can address stockpiles of existing long lived spent LWR fuel. These features could also allow nuclear plants to complement variable renewable energy sources such as wind and solar without requiring massively overbuilt generating capacity.

A subset of the Gen IV designs target these objectives by using liquid metals as heat transfer fluids. Liquid metals present many advantages from a heat transfer perspective. They are extremely efficient at removing heat from solid surfaces because, like familiar solid metals, they have high thermal conductivity (liquid sodium, for example, has a thermal conductivity of ~70 W/m-K, approximately 100 times higher than that of liquid water). The liquid metals of interest to nuclear designers, like sodium, also have very large liquid ranges. That is, they have a boiling point much higher than their melting point (98 - 883 °C for sodium). This means that nuclear reactor systems can operate at higher temperatures (and therefore higher thermodynamic efficiencies) without needing to pressurize the coolant and deal with large thick-walled pressure vessels, making many components more compact. High operating temperatures are also desirable in industrial process heat applications, which are also increasing along with electricity demands. The high thermal conductivity of liquid metals also contributes to decay heat removal during a loss of flow accident.

In addition to these thermal benefits, for sodium in particular, the neutron absorption cross-section is very low compared to water. Lack of neutron interaction with the primary coolant allows for a fast neutron spectrum rather than moderated thermal neutrons. This fast neutron spectrum means higher enriched fuel is typically needed, but a higher power density and smaller core are possible. The fast neutron spectrum is also suitable for uranium breeding, and the name "fast breeder reactor" is commonly used to refer to sodium-cooled reactors (figure 1) [3]. The nuclear industry has been using sodium since the 1950s in these types of reactors to breed nuclear fuels, and this feature may be very useful for "burning" the high level nuclear waste accumulating from the current reactor fleet; converting long lived radioisotopes to nuclides with much shorter half-lives [4].

These features make sodium a heat transfer fluid of interest to power plant and reactor designers in the nuclear industry. Liquid sodium is a pure metal with very high thermal conductivity (~70 W/m-K), low viscosity (~0.05 cP), and a density comparable to liquid water (~0.826 g/cm^3). Its specific heat capacity (~1300 J/kg-K) is less than that of liquid water (~4200 J/kg-K) [5]. The heat transfer behavior of liquid sodium can be characterized by its extremely low Prandtl number. This means it is more effective at diffusively transporting energy (heat) than it is at transporting energy by momentum [6]. The alkali metal is also famously reactive and will readily combine with oxygen or moisture in the air, producing heat and hydrogen gas. Consequently, there are important safety considerations to keep in mind when handling and working with the fluid, and systems must remain sealed, complicating fuel handling operations and plant maintenance. Despite these concerns, the excellent heat transport properties, neutronics, and inherent safety during off-normal operation make sodium fast reactors (SFRs) an

attractive technology for targeting new electricity markets and meeting ever growing demand for clean zero carbon energy.

For these reasons, SFRs have been identified as a promising concept that is seeing renewed interest in the commercial electricity generation sector. While classified as one of several *advanced* nuclear reactor types, SFRs have been in development since the 1950s, and several research and commercial reactors have been operated by the United States and other countries such as Japan, France, and USSR/Russia. Notably, the first nuclear reactor to produce usable electricity in December 1951 was cooled with a liquid sodium alloy (EBR-I). This reactor was followed up with the long running Experimental Breeder Reactor II (EBR-II) (1964-1994), operating at higher power levels and cooled with pure sodium metal in a pool type configuration. The US DOE national laboratories have operated these and other SFR research reactor projects such as the Fast Flux Test Facility (FFTF) and the Integrated Fast Reactor (IFR), successfully demonstrating passive "walk away" safety and fuel reprocessing/recycling.

Additional pool type SFRs have been employed for commercial power production throughout the second half of the twentieth century in France (Phenix, Superphenix) and Russia (BN series), and loop type reactors have also been operated at generating stations in Japan (Joyo, Monju), with varying degrees of success and project longevity.

The modern designs under development, such as the Versatile Test Reactor, PRISM (GE Hitachi), ARC-100 (Arc Clean Technologies), and currently most significantly Natrium (TerraPower and GE Hitachi), employ the advanced pool type design, with many of the same basic components [7], [8], [9], [10]. These rectors consist of a core containing the nuclear fuel, submerged in a circulating pool of primary liquid sodium coolant. This primary coolant then transfers its heat to a secondary closed loop of liquid sodium through an intermediate heat

exchanger (IHX), which is also submerged in the pool and often uses a shell-and-tube design. This secondary sodium loop then interfaces with the plant's power cycle through a power cycle heat exchanger, where the thermal energy is used to generate steam in a traditional modified Rankine cycle or to heat other working fluids (such as supercritical CO_2) in, for example, a closed loop Brayton cycle. This power cycle heat exchanger may also couple the secondary sodium loop to a thermal energy storage medium (as is done with molten nitrate salts in the Natrium design) to allow the plant to adjust its power output to follow daily electricity demand without affecting core power level.

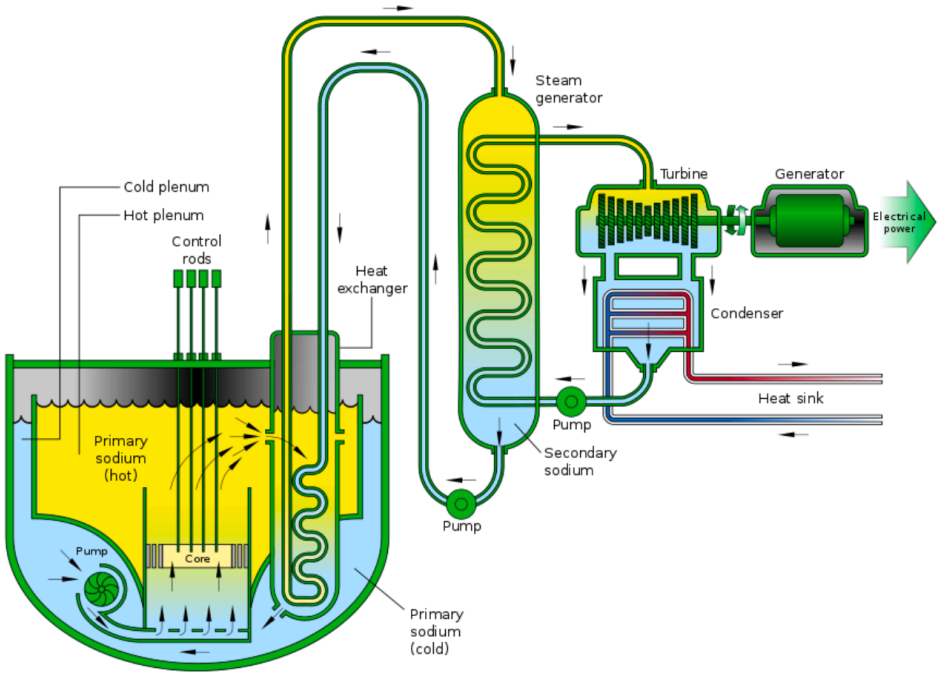

Figure 1-1: A pool type sodium fast reactor diagram.

The fuel assemblies in SFRs typically consist of close-packed hexagonal bundles of fuel pins, which are separated by helical *wire wraps* affixed to the fuel pin surfaces. These wire wraps

allow the primary sodium coolant to flow through each assembly while promoting turbulent mixing and generation of vortices as the sodium travels up the core.

Understanding the heat transfer behavior of liquid sodium under representative reactor conditions is a key requirement for accurate thermal hydraulic modeling of SFR systems. Predicting heat transfer under these conditions, however, is complicated by the unique thermal transport properties of liquid metals. Their extremely low Prandtl numbers lead to regimes where conductive and advective heat transport occur on comparable scales (i.e. low Peclet numbers) at flow velocities up to and including those present in SFR systems.

The selection of a Peclet number range of approximately 40–400 for the present experiments is motivated by its direct relevance to these SFR systems and related heat transport components. In operating reactor core subassemblies such as EBR-II, FFTF, and Phénix/Superphénix, characteristic Peclet numbers are on the order of 100–300 [11]. Similar conditions are encountered in SFR intermediate heat exchangers, where both shell-side and tube-side flows span a broad low-to-moderate Peclet range (approximately $30 < Pe < 500$), as well as in power cycle heat exchangers and other auxiliary reactor systems [12], [13]. Consequently, the chosen Peclet number range of 40–400 captures the dominant transport regimes of practical interest and allows experimental data to be generated under conditions directly representative of prototypical reactor applications.

Experimental characterization of heat transfer behavior in liquid metal systems is inherently difficult. Because liquid metals remove heat very efficiently from heated surfaces, relatively large heat inputs are required to produce measurable wall-to-bulk temperature differences. Under such conditions, local surface heat flux and measured temperature can become influenced by small variations in internal conduction thermal resistances, complicating

the interpretation of experimental data. These variations may arise from construction tolerances in electrical heaters, nonuniform internal conduction paths, and contact resistances. These sensitivities are well recognized in computational and experimental studies of sodium bonded metallic fuel pins, where detailed thermal analyses reveal that local variations in fuel-cladding gap geometry and bonding conditions can strongly affect the resulting cladding surface temperature distribution [14], [15], [16], [17].

Many historical and current SFRs, especially in the US, use metallic fuel, wear the fissionable uranium is in its metallic state either as a pure metal or alloying element. In typical reactor fuel pins, these are metallic fuel slugs of U-Zr or U-Pu-Zr alloys. These are cast and inserted into ferritic/martensitic stainless steel cladding with a small radial gap which is subsequently filled with liquid sodium to ensure high and ideally uniform thermal conductance across the annulus (a *sodium bond* construction). Although sodium bonding significantly reduces circumferential variations in heat transfer, post-fabrication examinations of sodium bonded pins have shown that slight eccentricity of the fuel slug is common, leading to measurable asymmetry in the annulus thickness and regions of incomplete or heterogeneous wetting of the sodium bond. These geometric and bonding variations necessarily produce corresponding azimuthal variations in cladding surface temperature. While published studies do not report a single quantified range for this effect in sodium-cooled metallic fuel pins, both sodium bond defect investigations and heavy liquid metal bundle experiments demonstrate that such asymmetries can produce meaningful azimuthal temperature differences. This is consistent with expectations for systems in which very small geometric variations induce observable thermal nonuniformities under high conductivity liquid metal cooling conditions [18], [19].

Beyond the challenges associated with fuel pin or heater construction and measurements of low Peclet number liquid metal flows in general, the presence of wire wrap spacers introduces a conjugate heat transfer problem that further complicates experimental investigation and modeling. While wire wraps enhance coolant mixing and convective heat transfer by inducing secondary flows at a fuel assembly bundle scale, they also provide an additional solid heat conduction pathway. Heat generated in the fuel pin is transferred to the sodium not only through direct convection at the pin surface, but also indirectly through conduction into the wire wrap, followed by convection from the wire wrap surface into the coolant (in both directions) [20]. This coupled conduction-convection process alters local temperature distributions, particularly in low Peclet number regimes where thermal diffusion effects are significant. Understanding this conjugate heat transfer behavior and its effect on local measurements is therefore essential for accurately characterizing and modeling heat transfer in wire wrapped fuel assemblies operating under representative SFR conditions.

In addition to the heat transfer and spacing benefits, the wire wraps also present an interesting opportunity for instrumentation of both experiments and potentially actual fuel. Their geometry provides a nonintrusive pathway for inserting temperature instrumentation deep within a pin bundle without disrupting the surrounding sodium flow. This work applies the technique to a single wire wrapped pin, also serving as a proof-of-concept for future deployment in larger bundle experiments, an approach of interest to both nuclear industry professionals and experimental researchers.

Chapter 2 – Liquid Metal Heat Transfer Literature Review

Understanding the heat transfer behavior of low Prandtl number fluids like liquid sodium is inherently challenging and relies heavily on experimental data. With a Prandtl number as low as 0.005 at 500 °C, classical analogies such as the Reynolds and extended Chilton-Colburn analogies are not applicable for predicting local turbulent heat fluxes. This means the Nusselt number, the friction factor, and the Reynolds number of the flow cannot be related simply [6], [21]. As a result, semiempirical correlations between the Nusselt number and the Peclet or Reynolds number have been developed through a combination of experimental measurements and modified analytical approaches [6], [21], [22], [23].

There are many existing experimental and computational studies of heat transfer to liquid metal flows and models for predicting this behavior. These studies range from very early correlations rooted in analytical thermal hydraulics physics to more recent investigations of flow behavior in multi-pin bundles using computational fluid dynamics (CFD) tools and high-performance computing.

The theoretical study of general turbulent convection lead by Reynolds in the early 1900s further progressed with the work of Prandtl and Taylor and their introduction of the idea of a viscous or laminar sublayer of fluid flow close to the wall in a turbulent flow where the frictional effects of the wall are still felt by the fluid and overcome the chaotic mixing of turbulent eddies [24]. However, velocity profiles in turbulent flows were still not well understood and hadn't been investigated at length experimentally until a complete study was undertaken by J. Nikuradse (a student of Prandtl) in 1932 [22]. The results of this work lead Von Karman to introduce a "buffer region" regime of flow between the viscous sublayer close to the wall and the "fully turbulent" core of the flow. Both molecular diffusion (thermal conduction) and advective fluid motion are

considered important in this buffer region, and the physics here are described by a *law of the wall* formulation. However, the work up to this point still assumed that diffusive transport (conduction) was negligible in the fully turbulent core of the internal flow and only advective mixing dominated.

Importantly, this is often not the case for liquid metals with their very high thermal conductivities driving significant conductive transport throughout the flow field. In a sense, even at turbulent Reynolds numbers above the transition regime, the heat transfer side of the convection problem doesn't necessarily conform to the conventional structure of turbulent internal flow that is familiar. Efforts to apply these analytical convection concepts to liquid metal flows began with work by Martinelli, which was published in a 1947 paper "Heat Transfer to Molten Metals," followed by Lyon with papers in 1949 and 1951, after seeing that just extrapolating previous convective heat transfer work would probably not be accurate for liquid metals [22], [25], [26].

These early liquid metal heat transfer studies, extending the work of Prandtl and others, established correlations of the form $Nu = A + BPe^{C}$, recognizing the Peclet number as the key flow parameter describing combined conductive and advective heat transport [22], [24]. This formed the basis for early experimental research from Martinelli (1947), Lyon (1949), Seban and Shimazaki (1951), and others [25], [26], [27]. Many of these early experimental data sets agree well, but the low Pe regime presents some problems. This is largely due to the nature of low Peclet number flows – where both molecular conduction and advection both play significant roles in heat transport. This dual influence complicates the characterization of heat transfer and may render simple dimensionless correlations insufficient for describing behavior across varying channel geometries and boundary conditions [20], [28]. Experimental data sets at low Peclet

numbers (Pe ~< 100) have shown inconsistent trends, with differing predictions of Nusselt number behavior [29], [30], [31], [32], [33], [34], [35], [36].

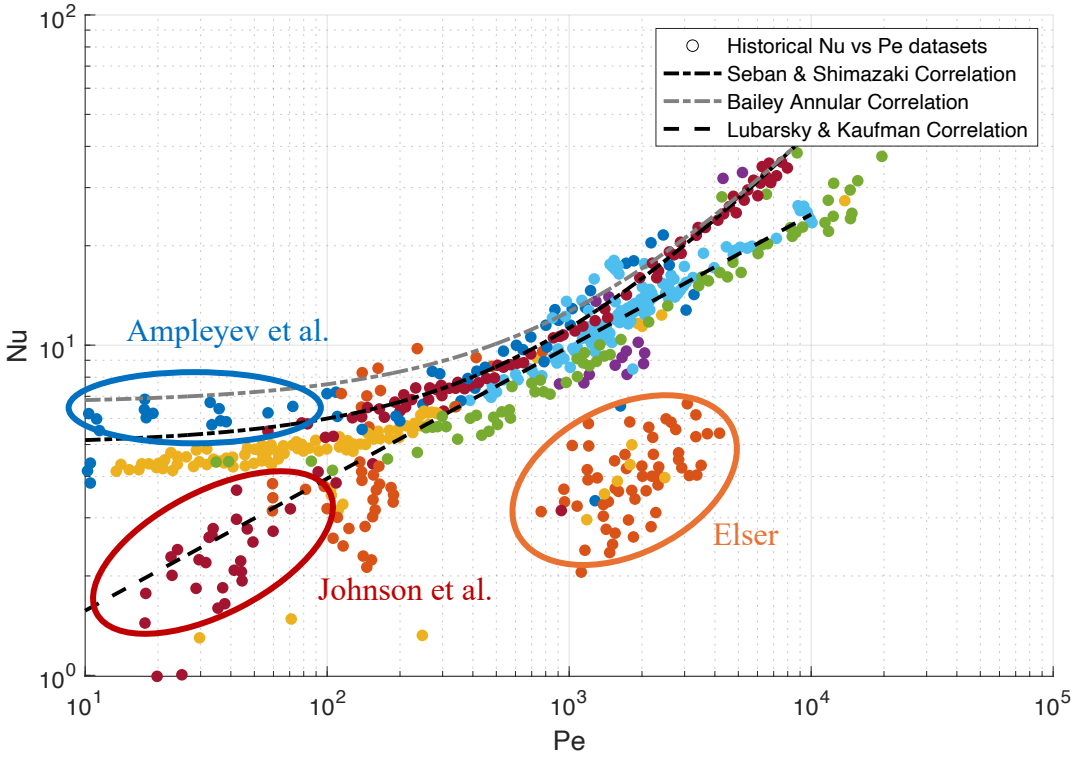

Figure 2-1: Historical liquid metal heat transfer data (modified from Mochizuki, 2018) [36].

The chart in figure 2-1 overlays a large number of historical Nu vs Pe data sets for liquid metal heat transfer, and the disagreement between the data sets in the low Peclet regime can be seen [36]. Particularly, the experiments of Johnson et al. (1953), Ushakov et al. (1963), and Subbotin (1963) show Nusselt numbers much lower than the data collected by others at Pe < 100 [29], [30], [31], [32]. The data sets of Skupinski et al. (1965), Ampleyev et al. (1969) and Ono et al. (2016), for example, basically agree with the early correlations from Lyon and Seban and Shimazaki [33], [34], [35]. They find that the Nusselt number approaches around 5 to 7 in the low Peclet number range, whereas the Johnson et al. (1953) and Subbotin (1963) experiments put

the Nusselt number much lower, trending to 1 as the Peclet number approaches about 30 [29], [32], [36].

The Nusselt number data from Elser for Peclet numbers around 10^3 in figure 2-1 also looks problematic [37]. This experiment was done with liquid mercury in round tubes of several diameters. The mercury flow was cooled by water in a surrounding annulus. Four thermocouples, two in the tube wall and two in the fluid, were used to take data for the region of fully developed flow. Elser states that the depth of the thermocouples in the wall is unknown. The data presented in figure 2-1 represents the re-evaluation of Elser's data by Lubarsky and Kaufman [38]. By altering the temperature assumptions used to compute the heat transfer coefficient, Lubarsky and Kaufman were able to increase Elser's Nusselt numbers by 40-60%. It is also shown that, depending on the depth of the wall thermocouple, the Elser data could actually be even higher [38]. This analysis comports with the earlier discussion on high sensitivity to internal conduction paths at the high heat flux, low convection resistance conditions of liquid metal experiments in chapter 1. Evidently, there are some problems in the setup and data analysis in the Elser experiment, and this data is contradicted by the bulk of the data for liquid metal flows over this Peclet number range. This Elser data is truly an outlying set that has not been replicated by other experimenters, and a consensus regarding the errors in the original work has been reached [36].

Three correlations for liquid sodium are also overlaid on the chart in figure 2-1. The Lubarsky and Kaufman correlation ($Nu = 0.025Pe^{0.4}$) was developed in the 1955 paper, "Review of Experimental Investigations of Liquid-Metal Heat Transfer," [38]. Much of the existing work on liquid metal heat transfer at the time was analyzed, and the correlation was created as a compromise that only comes within 60-80% of many data points, but it represents a good average over the entire data range [36], [38]. At low Peclet numbers, the Seban and Shimazaki

(1951) correlation (equation 2-1) is generally representative of much of the available data, and there is strong consensus regarding its validity [27], [39]. However, once again, a significant number of historical data points indicate much lower Nusselt numbers at low Peclet values.

$$Nu = 5 + 0.025Pe^{0.8} \qquad (2-1)$$

Measurements made inside the intermediate heat exchanger of the Monju sodium-cooled nuclear reactor during operation also showed much lower Nusselt numbers at low Peclet conditions. These findings renewed questions regarding which correlation is most appropriate for predicting heat transfer under low Peclet number regimes [40]. While many of these concerns were addressed with numerical analyses and explanations of possible errors in review papers by authors such as Mochizuki and Takano, there are still some lingering questions about the heat transfer behavior of liquid sodium flows at low Peclet numbers and there is agreement that additional experimental work is needed [36], [40], [41]. It should be noted that much of the historical experimental work focused on a variety of liquid metals and alloys flowing inside externally heated tubes or "figure eight" tube-in-tube liquid-metal-to-metal configurations, often with uncertainty of instrumentation [36]. The present work seeks to investigate liquid metal heat transfer in a format more consistent with those expected in sodium fast reactor cores; with a wire wrapped pin and a cosine-shaped axial heat flux profile.

Beyond the general liquid metal experimental work discussed above, several studies have specifically investigated heat transfer behavior in annular channels and within bundles of wire wrapped pins. Heat transfer correlations developed for thick annuli by Werner et al. (1949) and Bailey (1950), followed by Dwyer (1963) and Todreas (1994), are relevant for this work [11],

[42]. The Bailey correlation (equation 2-2) is shown in figure 2-1. In addition to these correlations, some experimental studies have examined heated wire wrapped pin *bundles* in liquid sodium, including experiments performed in PNC's SIENA sodium loop at Oarai, Japan using a heated 7-pin bundle [43]. Operational experience from sodium fast reactors such as EBR-II and FFTF has also provided valuable benchmarking datasets for evaluating heat transfer behavior in wire wrapped assemblies.

$$Nu = 0.75\left(\frac{d_{ann,outer}}{d_{ann,inner}}\right)^{0.3}(7 + 0.025Pe^{0.8}) \qquad (2-2)$$

In parallel with these experimental efforts, computational investigations using CFD methods including Reynolds-Averaged Navier-Stokes (RANS), Large Eddy Simulation (LES), and Direct Numerical Simulation (DNS) have been used to study flow and heat transfer in wire wrapped pin geometries. These simulations provide insight into the complex vortex structures induced by the wire wraps and their influence on local heat transfer [20], [44], [45], [46], [47]. However, robust, high-resolution experimental data suitable for validating such models remains limited, particularly for sodium flows in the low to moderate Peclet number regime.

Chapter 3 – Sodium Test Facility and Experimental Apparatus

3.1 - Overview of Sodium Heat Transfer Test Loop and Components

To enable SFR-relevant heat transfer testing in liquid sodium, a dedicated test facility was designed and constructed. The system features a vertical test section with upward sodium flow through an annular channel surrounding an electrically heated prototypical SFR fuel element simulator procured from Stern Laboratories. The simulator produces a cosine-shaped axial heat flux profile with total power up to ~40 kW and peak heat fluxes approaching 950 kW/m² over a 2 m heated length. To remove the added heat, the Sodium Heat Transfer Test Loop (SHTL) was coupled to a closed nitrogen loop via a printed circuit heat exchanger (PCHE). Sodium flow was driven by a moving magnet pump and nitrogen flow was driven by two two-piston compressors in parallel, enclosed in a vessel with a system pressure of ~1100 psi. The nitrogen loop was in turn coupled to a building chilled water/glycol system that acted as the final heat sink.

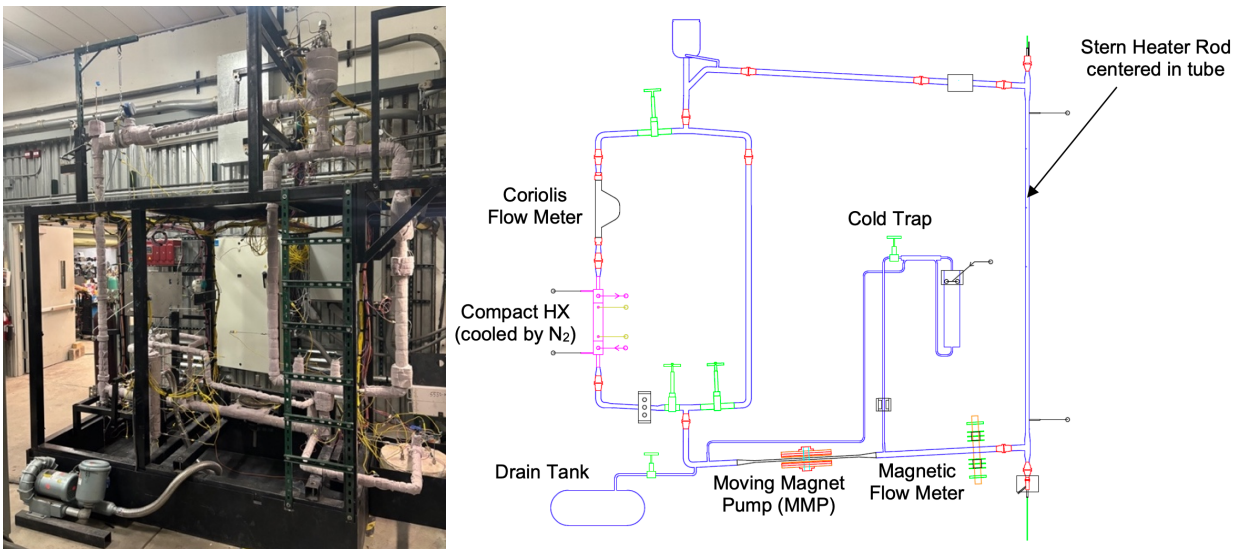

Figure 3-1: Sodium Heat Transfer Test Loop facility.

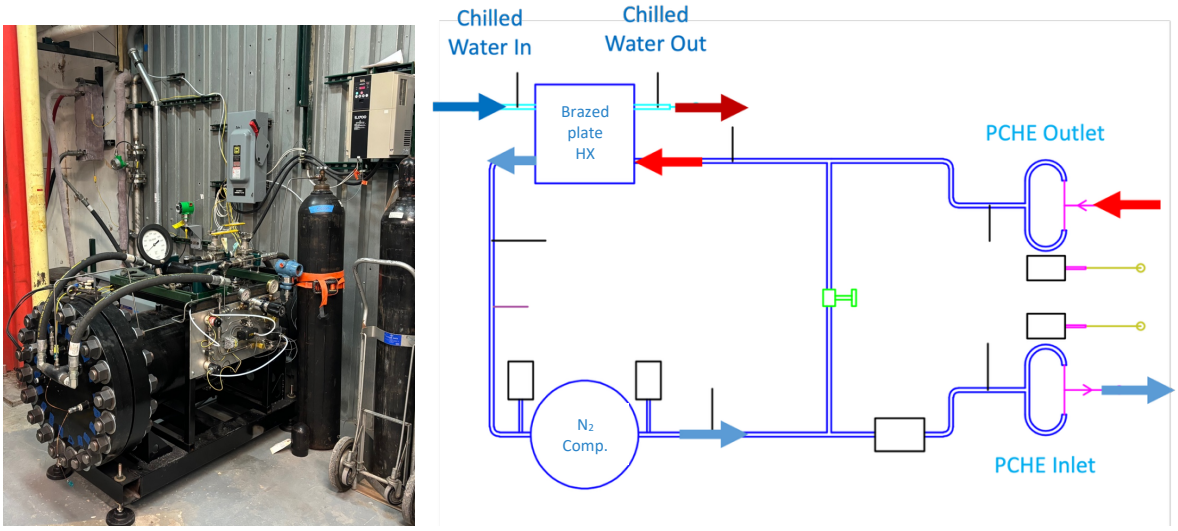

Figure 3-2: Nitrogen cooling compressor/loop.

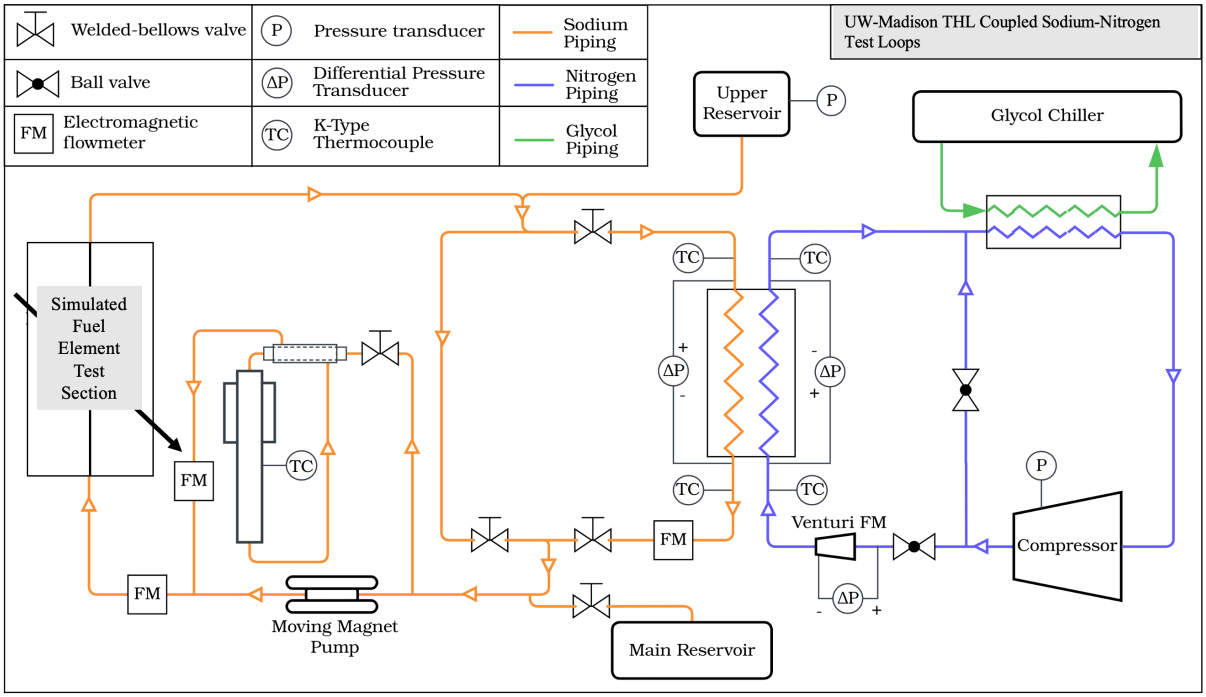

Figure 3-3: Piping and instrumentation diagram for coupled sodium and nitrogen loops in test facility (modified from Simons, 2025) [48].

The zig-zag channel diffusion-bonded sodium-to-nitrogen PCHE also allowed for the investigation of cooling mode liquid sodium heat transfer over a similar low Pe range in geometries that are of interest for SFR power conversion systems. The instrumentation and

testing of the PCHE were done in collaboration with Caleb Simons, and the results of the heat exchanger investigation can be found in his 2025 master's thesis.

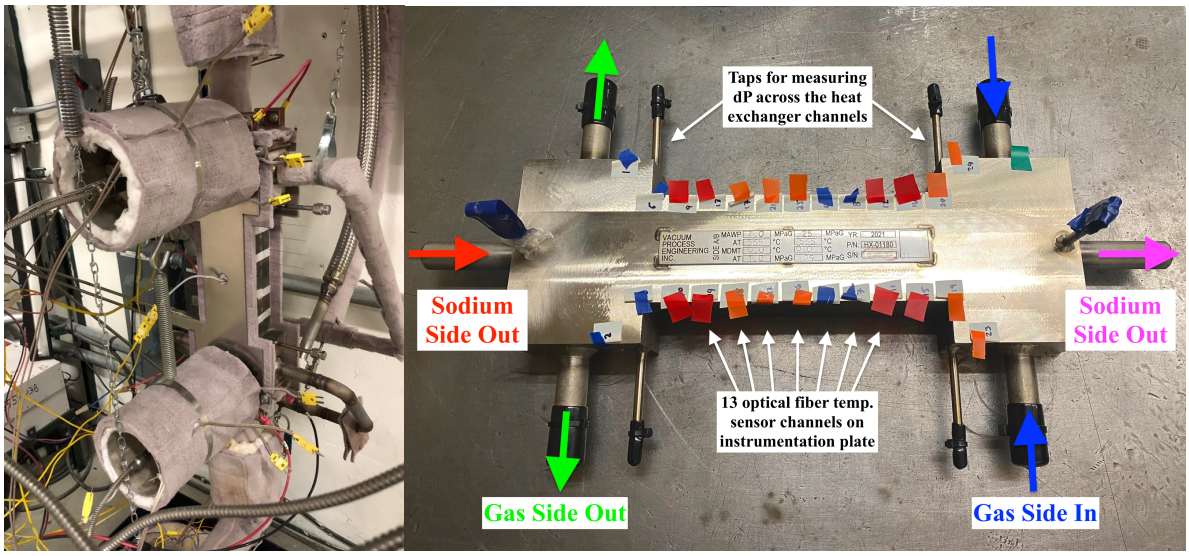

Figure 3-4: Sodium-nitrogen printed circuit heat exchanger.

A cold trap was used during all sodium loop operation and testing to pull off some of the sodium flow and locally cool it to 139 °C in a matrix of stainless steel wool, such that dissolved sodium oxides (with well-known temperature-dependent solubility, see equation 3-1) precipitate out. This ensures that all sodium inventory has < 2 wppm oxygen ("reactor grade") after sufficient cold trapping time [49]. While sodium impurity control in SFR systems is critical due to prevalent oxygen-dependent corrosion mechanisms, especially with Cr stainless steels, the measurement of oxygen level was not considered critical for the heat transfer analysis in this work.

$$log_{10}([Oxygen][wppm]) = 6.239 - \frac{2447}{T_{sat}[K]} \qquad (3-1)$$

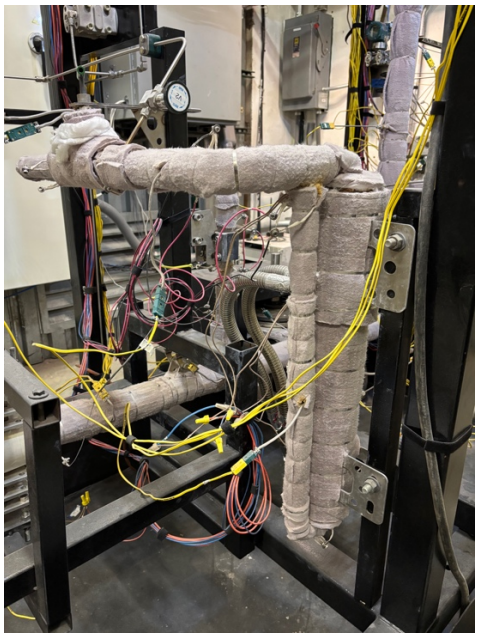

Figure 3-5: Sodium Heat Transfer Test Loop cold trap.

3.2 - Test Section

The test section's fuel simulator rod is clad in a 0.020 inch thick layer of 316 stainless steel and has a finished outer diameter of 0.376 inches (9.54 mm). It was centered within a test section tube of 0.834 inch inner diameter (ID) and 1.00 inch outer diameter (OD). The fuel simulator rod features a helically wrapped hollow 316 stainless steel capillary tube of 0.056 inch OD and 0.0335 inch ID affixed to its outer surface to house a fiber optic temperature sensor (FOTS). This tube is hereafter referred to as the "wire wrap" to distinguish it from other capillaries in the apparatus. The FOTS installed in the wire wrap consisted of a 0.016 inch OD by 0.010 inch ID 316L stainless steel tube which housed a 240 µm OD by 180 µm ID glass capillary tube. This tube enclosed the 125 µm diameter bare silica glass optical fiber. In addition to the wire wrap fiber optic temperature sensor, two axial FOTSs were embedded inside the Stern rod, running along its length, and a transverse FOTS was installed such that it cut across the test section perpendicular to the flow. The transverse sensor measured sodium temperatures at three elevations, capturing data at seven radial locations per pass (see table 3-1). Each pass of

the transverse FOTS (125 μm optical fiber) ran through a 0.0313 inch OD by 0.016 inch ID capillary tube that spanned across the test section laterally with its outer surface 0.050 inches off the heater rod surface, on the side opposite to where the wire wraps pass and opposite the test section inlet and outlet pipes. These high temperature FOTSs were fabricated using methodologies established as part of the instrumentation research and technology development objective of this project, which is the subject of chapter 4 [50], [51], [52], [53], [54], [55], [56].

Figure 3-6 shows cross-sectional and side profile diagrams of the fuel rod simulator and test section, with temperature measurement locations annotated. A sampling of X-ray images that show each internal thermocouple (TC) probe's location with respect to the wire wrap and heater filament position are also given. The wire wrap was applied at a pitch of one complete wrap per 18 cm along the rod, with the wrap direction being like that of a righthand thread, and close-up images of the wire wrapped rod are provided in figure 3-7.

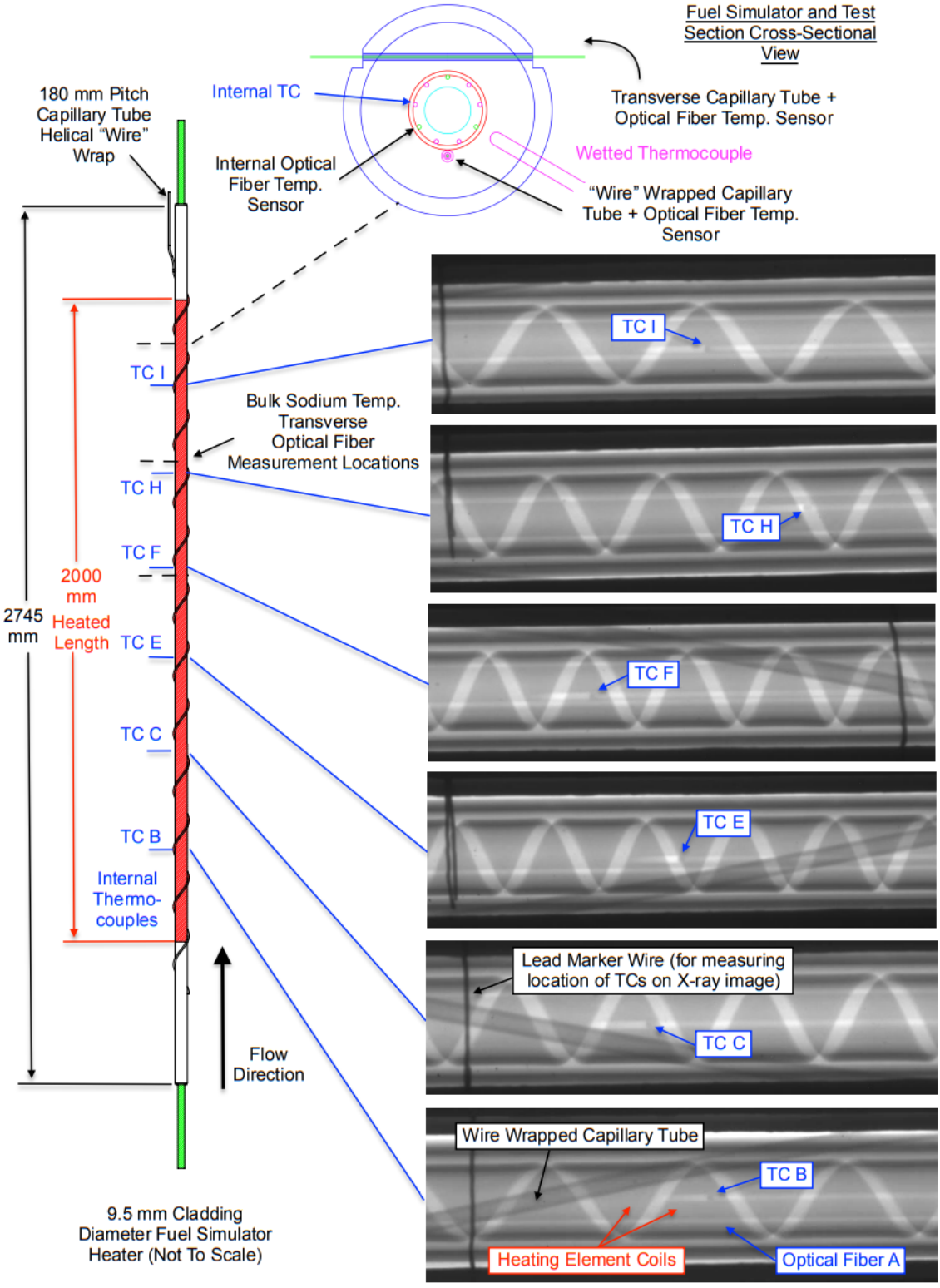

Figure 3-6: Fuel simulator rod and test section diagrams with instrumentation locations and rod X-ray imaging.

Figure 3-7: Helically wrapped capillary tube on fuel simulator rods (left) and test section capillary tubes for transverse fiber optic temperature sensors (right).

The fuel simulator's wire wrap was laser welded to the rod cladding at the top and bottom of the wrapped region, and the wrap was applied at the precise 18 cm pitch required with the help of Dr. Darius Lisowski and equipment at Argonne National Laboratory. This wire wrapping process, with a unique hollow capillary tube instead of a solid wire, was developed through a trial-and-error process using small rod sections and mock fuel simulators. For the final wrap, a preload of 10 lbs of tension was applied based on thermal expansion and thermal stress calculations for the Stern heater rod and wire wrap under expected operating conditions. A 0.0015 inch feeler gauge did not slip between the wire wrap and rod surface. The final technique was documented in detail and represented another project outcome of interest to the sponsor.

Following the application of the hollow wire wrap, the geometry of the rod was characterized in detail using X-ray imaging and normal photography. A series of 48 pictures of the rod as indexed were stitched together and compared to an AutoCAD drawing of the nominal 18 cm wrap pitch. The wrap pitch was found to match the prescribed pitch to within the resolution of our imaging. The orientation of the wrap (top and bottom welds and dead end) relative to the embedded capillary tubes and thermocouples was also recorded, as was the indexing of the entire wrapped rod relative to the surrounding test section tube and inlet/outlet from the sodium loop. These indexing parameters differed slightly from the design values, but

as-built measurements were recorded and used for future analysis. A report on the conformity and positioning of the wrapped heater rod was also delivered to the project sponsor and collaborators at Oregon State University.

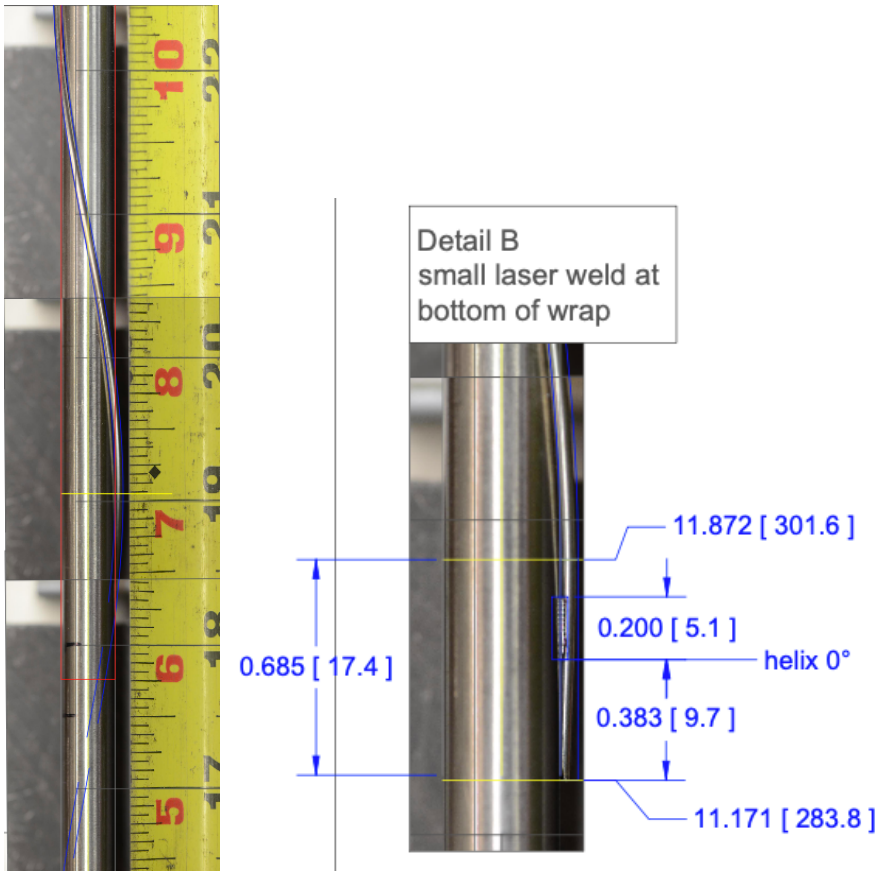

Figure 3-8: Demonstration of wire wrap conformity and as-built analysis (image overlays courtesy of Ian Jentz).

There are 12.5 complete wraps between the upper and lower welds affixing the wire wrap to the fuel simulator with the closed bottom end of the wrap positioned 1.314 inches vertically below the test section sodium inlet. The wire wrap closed end was indexed 74° clockwise relative to the inlet and outlet tube centerlines, as viewed looking downstream along the longitudinal axis from the top of the test section. The 2 m long heated length begins 5.065 inches vertically above the sodium inlet. Sodium exited the test section through a tube at the top of the

test section at the same angular position as the inlet, 86.965 inches above the inlet. The fuel simulator's chopped-cosine-shaped axial heat flux profile is described by the following equation for the ratio of local power or heat flux to average power or heat flux:

$$\frac{\dot{q}(z_{HL})}{\dot{q}_{avg}} = 0.8187458177 + 0.6812541823 \cos\left(2 * 2.436354311 * \frac{z_{HL}}{2\,m} - 2.436354311\right) \quad (3-2)$$

Where z_{HL} represents the axial coordinate relative to the beginning of the heated length.

The test section pipe includes graphite-packed seals on each end of vertical tube, sealing to the fuel simulator rod, and, in the case of the top seal piece, allowing the wire wrap to exit the sodium volume so the fiber optic sensor can be installed. The bottom seal piece also utilizes a 316 stainless welded expansion bellows to couple the rod seal to the rest of the test section tube wall. This allows for differential thermal expansion between the heater and the rest of the test section during operation. Both seal bodies were cooled with copper cooling blocks and Paratherm NF heat transfer oil circulating through a cooling bath.

A calibrated permanent magnet electromagnetic flow meter (EMFM) was used to measure the sodium flow rate through the test section [57]. Fluid temperatures were measured by calibrated thermocouple probes located at the inlet, outlet, and an intermediate location of the test section. Six additional thermocouples embedded beneath the cladding of the fuel rod simulator measured the internal temperature distribution, in addition to the FOTS sensors. The axial locations of each of the thermocouples and transverse FOTS passes in the test section are listed in table 3-1, relative to the sodium inlet to the test section and increasing with the upward flow direction.

Table 3-1: Axial locations of test section instruments.

LabVIEW label (#)	Stern TC label (letter)	Axial location [m]
TC4	- (test section inlet)	0
TC26	B	0.415
TC28	C	0.704
TC29	E	0.989
Lower trans. FOTS	-	1.095
TC42	F	1.276
Middle trans. FOTS	-	1.455
TC47	H	1.558
TC52	I	1.815
TC10	- (test section intermed.)	1.815
Upper trans. FOTS	-	1.815
TC12	- (test section outlet)	2.210

3.3 - Sodium Loop Instrument Calibration

The critical thermocouples and EMFM were calibrated against ISO 17062 certified NIST-traceable reference instruments, and additional instruments and their data acquisition system (DAQ) channels were calibrated and/or verified with reference signals provided by instrument transmitters or a traceable process calibrator.

3.3.1 - Thermocouple Calibration

Of the SHTL facility's 76 total control and measurement K-type thermocouples, 16 critical thermocouple probes were identified and subjected to calibration against an ISO 17025 certified Fluke platinum resistance thermometer (PRT) in a furnace designed for this purpose. The furnace is wrapped with AC heaters and houses a silicon carbide block with four 6 inch deep wells bored into it to hold batches of up to four thermocouple probes and the PRT. This furnace has been used in calibration of TCs for other experiments and verified to have no significant thermal gradients between wells at steady state operation over the temperature range of interest [58], [59]. The TC calibration setup is shown in figure 3-9. The TCs were calibrated as a

complete system *while installed in the SHTL DAQ,* in the same configuration to be used in all further reported testing with the sodium loop.

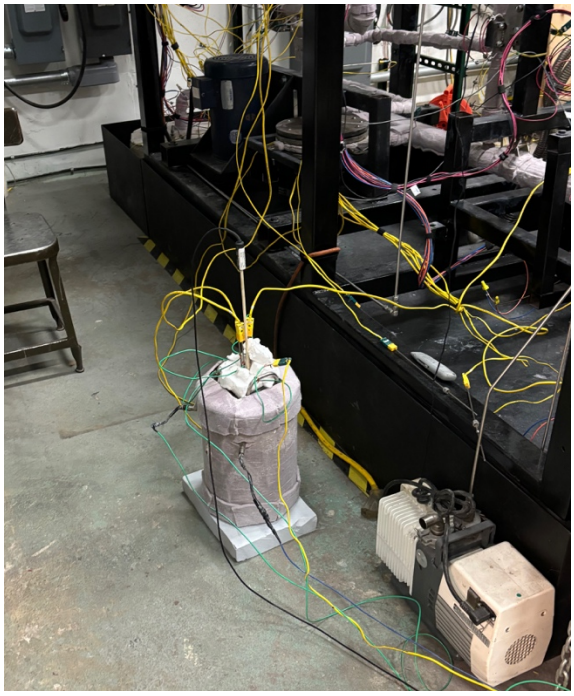

Figure 3-9: Thermocouple probe calibration furnace setup with platinum resistance thermometer (PRT).

Between four and seven steady state nominal temperature calibration points were identified for the furnace operation, across the range of the TC probe being calibrated. Data was recorded from the TCs and PRT for 20 seconds per point at a frequency of 10 Hz. The calibration range was cycled through at least three times, with calibration data saved for each cycle. The furnace was determined to be at steady state when the temperature drifted at a rate of < 0.03 °C over the 20 second recording interval, as measured by the PRT. The data were time averaged after recording. The six internal thermocouples embedded throughout the heated length of the nuclear fuel simulator rod were calibrated with a similar process via isothermal operation of the loop with a sodium flow at five temperature points over the 200 °C – 550 °C range using the calibrated test section inlet and outlet TCs as a reference. An example plot showing

calibration data for one thermocouple probe is given in figure 3-10. Similar plots and calibration data tables were generated for each probe and reported.

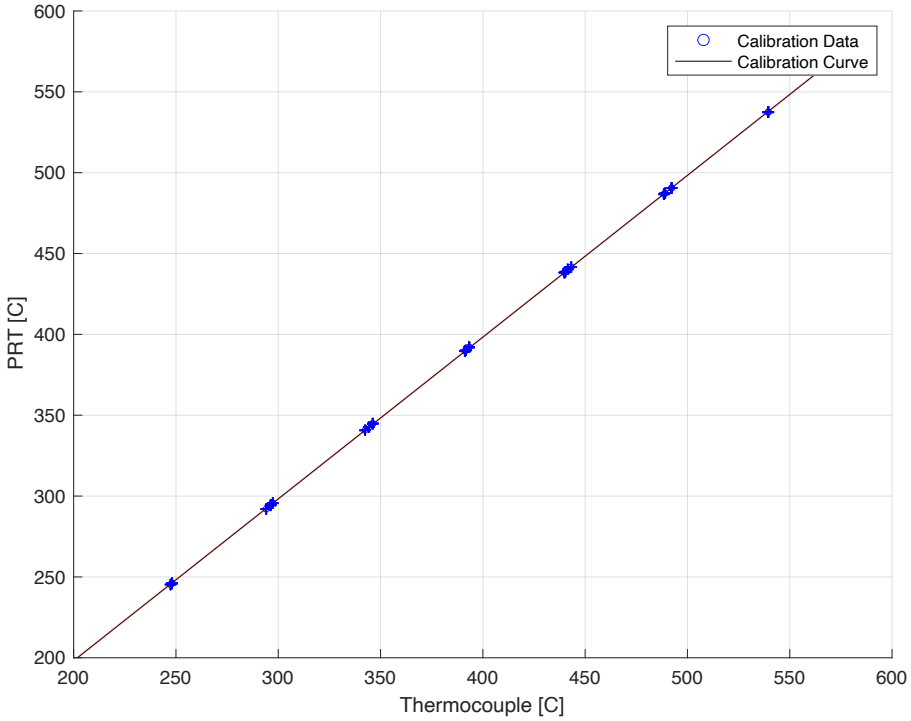

Figure 3-10: Thermocouple probe calibration data for TC12 (test section outlet).

The calibration data was processed to obtain uncertainties and calibration curves by applying a Deming linear regression technique. A jackknife statistical technique was used to calculate 95% *prediction* intervals, and the independent reference PRT was included by summing in quadrature. The A and B coefficients in the calibration curve equations that were applied to correct each TC's measurement signal (form $T_{cal} = AT_{uncal} + B$) are given in table 3-2. Limits of $0.98 < A < 1.02$ and $-2\ °C < B < 2\ °C$ were used to determine that each thermocouple probe was wired to the cRIO correctly and operating as intended. The *calibrated uncertainties* of each critical TC as installed in the experimental apparatus are given in table 3-2.

Table 3-2: Critical thermocouple uncertainties and calibration information. Calibration was performed over the 200 °C – 550 °C temperature range.

LabVIEW Label	Stern Label	TC Location	Calibrated Temperature Range	A	B	TC Uncertainty
TC4	-	Test section inlet	200 °C - 550 °C	0.9990	-1.620 °C	± 0.652 °C
TC10	-	Test section top TFOTS height	200 °C - 550 °C	0.9952	1.285 °C	± 0.731 °C
TC12	-	Test section outlet	200 °C - 550 °C	1.0005	-1.908 °C	± 0.518 °C
TC26	B	Internal Stern rod TC B	200 °C - 550 °C	1.0022	-0.268 °C	± 0.642 °C
TC28	C	Internal Stern rod TC C	200 °C - 550 °C	1.0023	-0.095 °C	± 0.568 °C
TC29	E	Internal Stern rod TC E	200 °C - 550 °C	1.0024	-0.160 °C	± 0.580 °C
TC42	F	Internal Stern rod TC F	200 °C - 550 °C	1.0016	0.1284 °C	± 0.590 °C
TC47	H	Internal Stern rod TC H	200 °C - 550 °C	1.0031	0.2759 °C	± 0.563 °C
TC52	I	Internal Stern rod TC I	200 °C - 550 °C	1.0013	0.4098 °C	± 0.639 °C
TC2	-	Fluid TC EMFM1	250 °C - 550 °C	0.9992	-1.78 °C	± 0.549 °C
TC33	-	PCHE sodium inlet	250 °C - 550 °C	0.9979	-1.143 °C	± 0.386 °C
TC39	-	PCHE sodium outlet/EMFM2	250 °C - 550 °C	0.9973	-0.874 °C	± 0.349 °C
TC73	-	Cold trap isothermal top	100 °C - 250 °C	0.9892	1.173 °C	± 1.246 °C
TC74	-	Cold trap isothermal mid (upper)	100 °C - 250 °C	0.9894	1.186 °C	± 1.242 °C
TC75	-	Cold trap isothermal mid (lower)	100 °C - 250 °C	0.9901	1.218 °C	± 1.222 °C
TC76	-	Cold trap isothermal bottom	100 °C - 250 °C	0.9901	1.264 °C	± 1.223 °C

3.3.2 - Electromagnetic Flow Meter Calibration

In addition to thermocouples, two of the permanent-magnet electromagnetic flow meters were also deemed critical equipment. As such, they were calibrated against a ISO 17025 certified Emerson Micro Motion F025A Coriolis style flow meter (CFM) [60]. Because the CFM's operation was limited to < 350 °C, calibration data was only recorded up to 325 °C, and a second vortex shedder style flow meter (VSFM) was plumbed into the sodium loop in series and used to confirm the EMFM calibration up to its operating limit of 400 °C. Previous experience calibrating this design of permanent magnet flow meters in the THL was drawn upon [61], [62], [63].

EMFMs make use of the metallic nature of the sodium fluid, applying a magnetic field B across the loop pipe of inner diameter d, perpendicular to the flow direction. This magnetic field, coupled with the velocity of the liquid sodium metal, causes the free electrons in the sodium to migrate to one side of the pipe and a potential difference akin to a Hall effect voltage is developed. This voltage V is measured by the data acquisition system and translated back to a sodium velocity or flow rate through equation 3-3.

$$\dot{V} = u_{mean} A_{cs} = \frac{K_4 \pi V d}{4 B K_1 K_2 K_3} \qquad (3-3)$$

The coefficients K_1, K_2, and K_3 in equation 3-3 are calculated using the electrical conductivity of the sodium and the 316 stainless pipe wall, and the pipe inner and outer diameter; accounting for wall effects. The magnetic field between the yoked 2 inch N52 neodymium cube magnets was measured with a magnetometer prior to their install on the loop, to serve as a check on the calibration result (table 3-3). This arrangement is shown in figure 3-11. Ultimately the signal was calibrated anyway in its final configuration in the loop via calibration coefficient K_4.

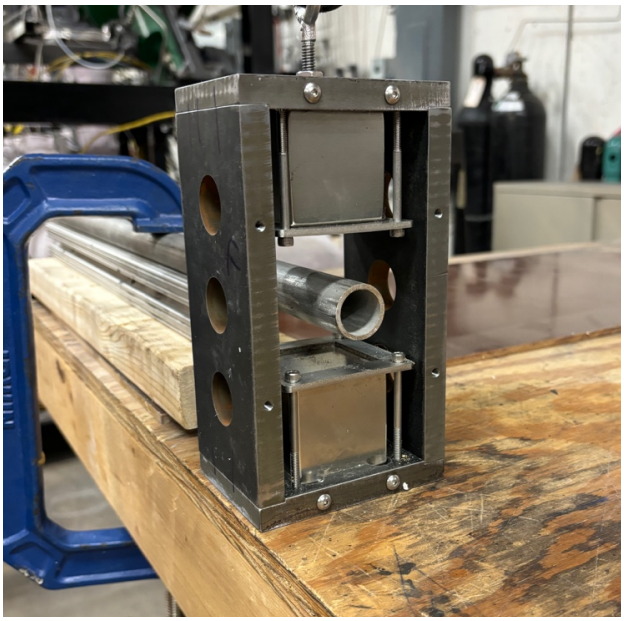

Figure 3-11: Electromagnetic flow meter being assembled and prepared for magnetic field measurement.

Table 3-3: Magnetic field B measurements via magnetometer.

Flow Meter	Measured Mag. Field (w/ tube)	Measured Mag. Field (w/out tube)
EMFM 1	2.32 kGauss ± 0.02 kGauss	2.56 kGauss ± 0.02 kGauss
EMFM 2	2.32 kGauss ± 0.02 kGauss	2.56 kGauss ± 0.02 kGauss
EMFM 3	1.927 kGauss ± 0.005 kGauss	1.951 kGauss ± 0.005 kGauss

Calibration of the two EMFMs (the printed circuit heat exchanger EMFM and the main loop EMFM) was performed in series at eight steady state flow conditions ranging between 0.5 gpm and 15 gpm. The sodium loop was filled, and the cold trap was operated to drive oxygen impurity concentration down to the 2 wppm level. The loop was operated for a period of 96 hours, including 36 hours at 325 °C, and the raw uncalibrated EMFM signals were monitored to ensure wetting of the pipe walls by sodium was achieved. This process ensures any pre-existing oxide layers on the pipe wall are dissolved into the sodium and subsequently deposited in the cold trap, such that the sodium is in good stable electrical contact with the pipe walls and ultimately the voltage measurement on each EMFM DAQ channel, and it is an important step when a new liquid sodium loop is fabricated, filled, and operated for the first time. The eight

flow rate points over the calibration range were swept through at temperatures of 150 °C, 200 °C, 250 °C, and 325 °C with the CFM installed in the loop and the raw voltage signal from each EMFM was recorded along with the CFM measurement in kg/s and gpm. The data was recorded at 10 Hz for 20 seconds and time averaged in post-processing. A EMFM signal (V) vs CFM measured mass flow rate (kg/s) plot of the calibration data obtained for both critical EMFMs at 325 °C is given in figure 3-12. Similar plots were generated for each calibration temperature point and possible temperature effects were also evaluated.

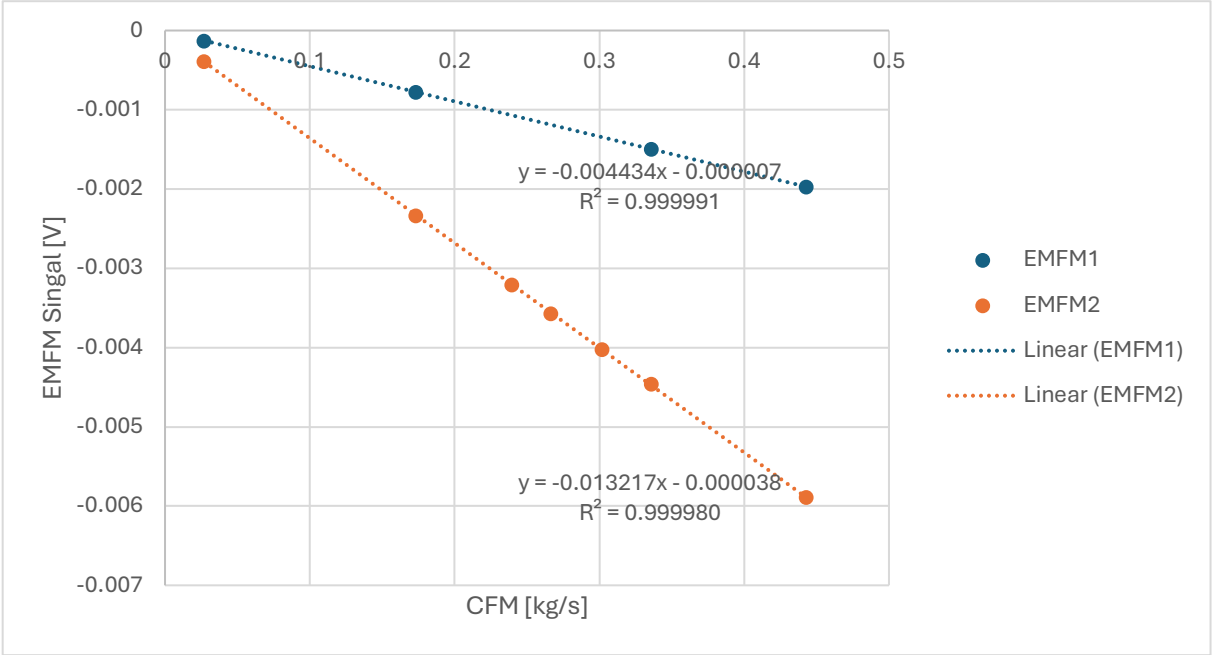

Figure 3-12: Electromagnetic flow meter calibration data for 325 °C condition. EM flow meter signal (V) is plotted against measured Coriolis flow meter mass flow rate (kg/s).

The raw voltage recordings for each calibration point were put through equation 3-3 with nominal geometry and field values for each flow meter, and the Coriolis flow meter measurements were converted to volumetric flow rate. According to a THL lab procedure, THL-OCL-PROC-1801, a reverse ordinary least squares linear regression was used to calculate a scaling coefficient for the flow rates at each temperature, and these coefficients were averaged to

obtain a single K_4 multiplicative coefficient that corrects the measured magnetic field for each flow meter [64]. With the CFM removed from the loop, a calibration case relative to the VSFM was performed at 400 °C to confirm the calibration held within uncertainty for higher temperatures. The K_4 coefficients resulting from the calibration at each temperature point, and the average K_4 values applied in LabVIEW are given in table 3-4, along with the uncertainties calculated for each flow meter. Uncertainties were obtained by calculating the standard error of the estimate of the corrected calibrated EMFM measurements in reference to the Coriolis flow meter measurements. This standard error was then compounded with the measured DAQ channel uncertainty for the CFM and the calibrated stated accuracy of the CFM of ± 0.2%. The K_4 calibration coefficients were applied with the EMFM equation (equation 3-2) in the SHTL NI LabVIEW control system's block diagram.

Table 3-4: K_4 calibration coefficients and estimated EMFM uncertainties.

EM Flow Meter	Temperature	K4	Average K4	Uncertainty (95%)
EMFM 1	150 °C	1.0703	1.0690	± 0.1395 gpm
	200 °C	1.0748		
	250 °C	1.0755		
	325 °C	1.0555		
EMFM 2	150 °C	1.0625	1.0707	± 0.1623 gpm
	200 °C	1.0768		
	250 °C	1.0789		
	325 °C	1.0648		

3.3.3 - Data Acquisition System Verification

In addition to instrument calibration, the measurements of DAQ channels were also verified in reference to supplied source signals. The reference signals were supplied from either an ISO 17025 certified Fluke 726 process calibrator or an instrument's transmitter via interfacing with the transmitter's settings or attaching a HART communicator. Three nominal signal

operating points were identified for each DAQ channel, spanning the instruments' range. Typically, the lower range signal, upper range signal, and center of the range signal were supplied (4 mA, 12 mA, and 20 mA for a 4 mA – 20 mA instrument). These mA signals were read by using a NI-9205 module to measure voltage across a 250 Ohm resistor. In this configuration, 4 mA, 12 mA, and 20 mA signals correspond to ~1 V, ~3 V, and ~5V measurements. Thus, the equivalent voltage measurements are used as the DAQ verification units in the following plots since this is the signal read into the DAQ system. Data was recorded for 20 seconds at each signal point, at a frequency of 10 Hz, and the range of signal operating points was swept through at least three times, with data recorded at each point. An example plot showing verification data for one DAQ channel is given in figure 3-13. Similar plots and verification data tables were generated for each channel and reported.

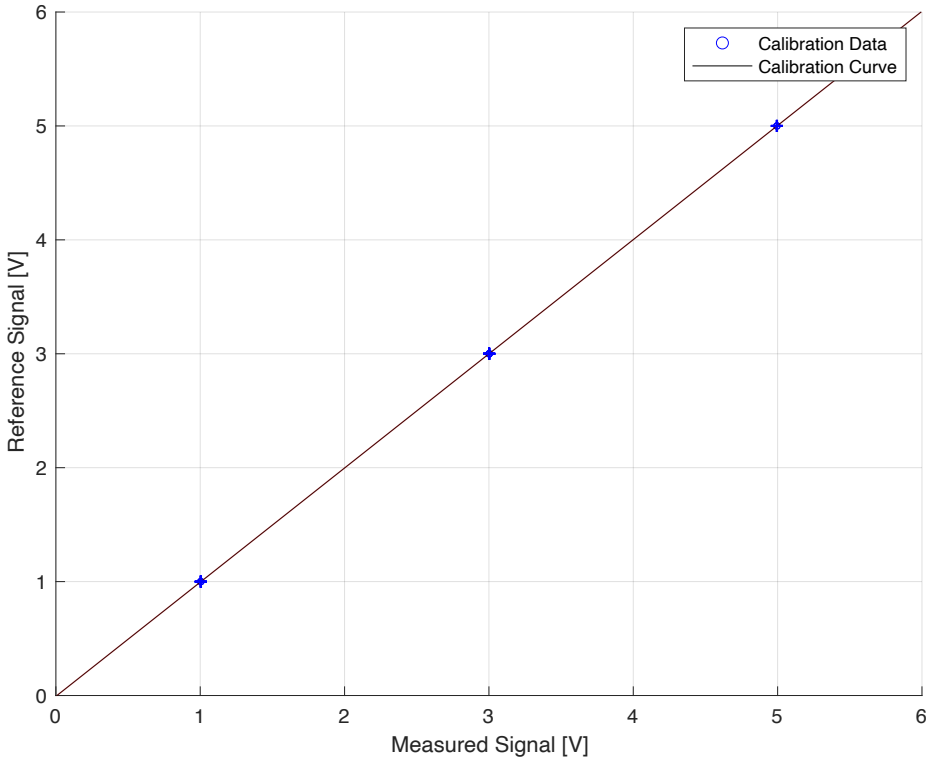

Figure 3-13: Data acquisition system channel verification data for upper reservoir gauge pressure transducer.

The verification data was processed to obtain equivalent uncertainties and signal correction curves by applying a Deming linear regression technique, as was done for thermocouple calibration in 3.3.1. A jackknife statistical technique was used to calculate 95% *prediction* intervals, and the independent reference signal uncertainty was included by summing in quadrature. The A and B coefficients in the signal correction curve equations that were applied to correct each channel's measurement signal (form $V_{cal} = AV_{uncal} + B$) are given in table 3-5. Limits of $0.98 < A < 1.02$ and $-0.02\ V < B < 0.02\ V$ were used to determine that each instrument was wired to the cRIO correctly and operating as intended. The *signal corrected uncertainties* of each instrument as installed in the experimental apparatus are given in table 3-5, although these DAQ channels were not necessarily considered critical equipment for the experiment.

Table 3-5: Signal correction curve coefficients ($V_{cal} = AV_{uncal} + B$) and corrected uncertainties for data acquisition system channels.

LabVIEW Ins. Label	Instrument Location	A	B	Corrected Signal Uncertainty
CFM	Coriolis flow meter (EMFM cal. ref.)	1.0036	0.0096 V	± 0.017 V
DCSCR Load kW	Stern rod DC load in kW	1.0017	-0.0074 V	± 0.000 V
DCSCR Load V	Stern rod DC load in V	1.0012	-0.0019 V	± 0.000 V
LwrRsvr	Lower reservoir pressure	1.0004	-0.0044 V	± 0.000 V
MMPMotor	MMP motor speed	1.0001	-0.0032 V	± 0.000 V
UprRsvr	Upper reservoir pressure	1.0022	-0.0072 V	± 0.000 V
VSFM1	Sodium vortex shedder flow meter	1.0004	-0.0042 V	± 0.000 V
dP1	Sodium test section dP	1.0005	-0.0036 V	± 0.000 V
dP2	Nitrogen side PCHE dP	1.0008	-0.0044 V	± 0.000 V
dP3	Sodium side PCHE dP	1.0003	-0.0037 V	± 0.000 V
PN2	Nitrogen loop vessel pressure	0.9999	-0.0041 V	± 0.000 V
VSFM2	Nitrogen vortex shedder flow meter	1.0005	-0.0037 V	± 0.000 V
dP4	Nitrogen compressor dP	1.0011	-0.0045 V	± 0.000 V
VFM1	Nitrogen Venturi flow meter	1.0009	-0.0051 V	± 0.000 V

The signal correction curves were systematically applied to their corresponding DAQ channels in the LabVIEW block diagram and the raw DAQ verification was recorded and reported.

3.4 - Fiber Optic Temperature Sensor Validation

The fiber optic temperature sensors themselves were calibrated in a tube furnace according to a THL documented laboratory procedure developed for this task [50], [51]. FOTS sensors fabricated from the same lot or spool of optical fiber have been shown to be very consistent and a single correlation is used in data post-processing to translate measured spectral shift (GHz) to temperature (°C) at each gage location along a fiber probe. A cubic polynomial correlation and key temperature correction step were applied, and a total estimated 95% prediction interval bound of ± 5.80 °C was established for the temperature measurements [52]. The fabrication methods and calibration/uncertainty analysis of the fiber optics temperature sensors are discussed in detail in chapter 4.

A Luna ODiSI-6104 laser interrogator system was used to record spectral shift data from the FOTSs during the experiment for up to four sensor channels at a time. Spectral shift/temperature measurements were made every 2.6 mm along the length of each fiber, at frequencies of 4 – 12.5 Hz. The complete SHTL system with installed FOTSs is shown in figure 3-14.

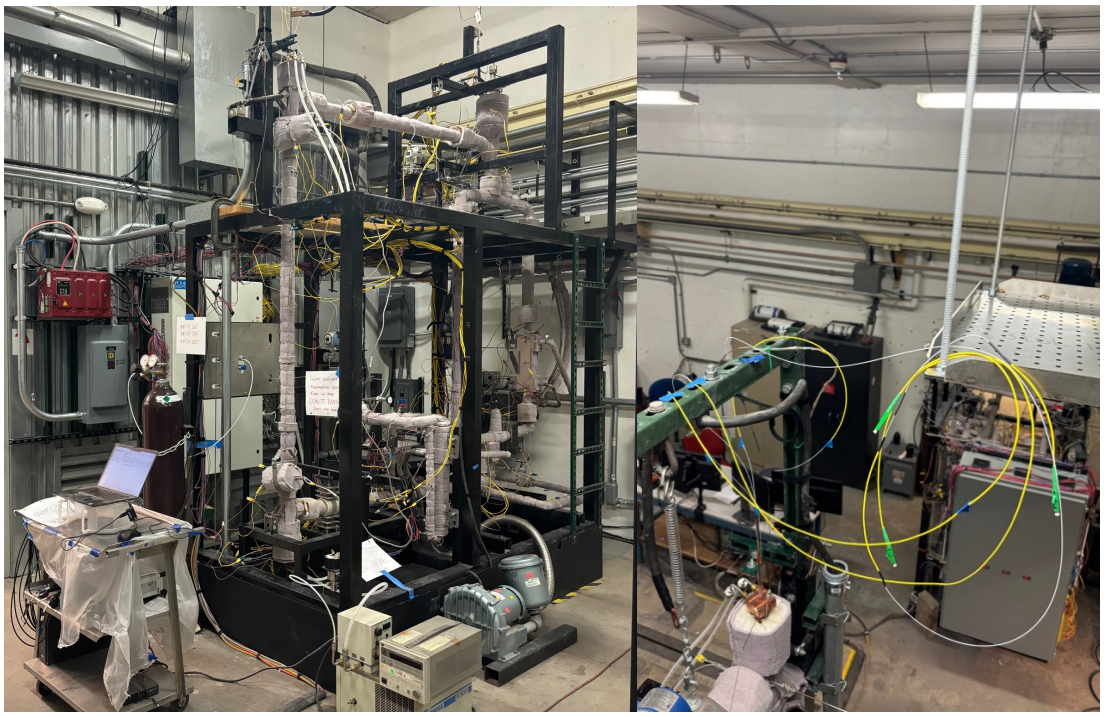

Figure 3-14: Complete Sodium Heat Transfer Test Loop with installed fiber optic temperature sensors (left) and FOTS exiting atop the test section (right).

Sensor validation was performed under isothermal conditions from 200 °C to 550 °C and sodium flow rates between 1 and 12 gpm (9,000 < Re < 70,000). These tests confirmed the FOTS measurements, as installed, were accurate within the combined uncertainty of the FOTS calibration correlation and that of the calibrated thermocouples. Data collected by the helical wire wrap FOTS during this *validation* testing are displayed in figure 3-15, with the solid black lines representing the fiber temperature measurements. Additional validation test data are presented on plots in appendix A. The fiber measurements agreed with the reference thermocouples within the uncertainty bounds for all tests and sensors.

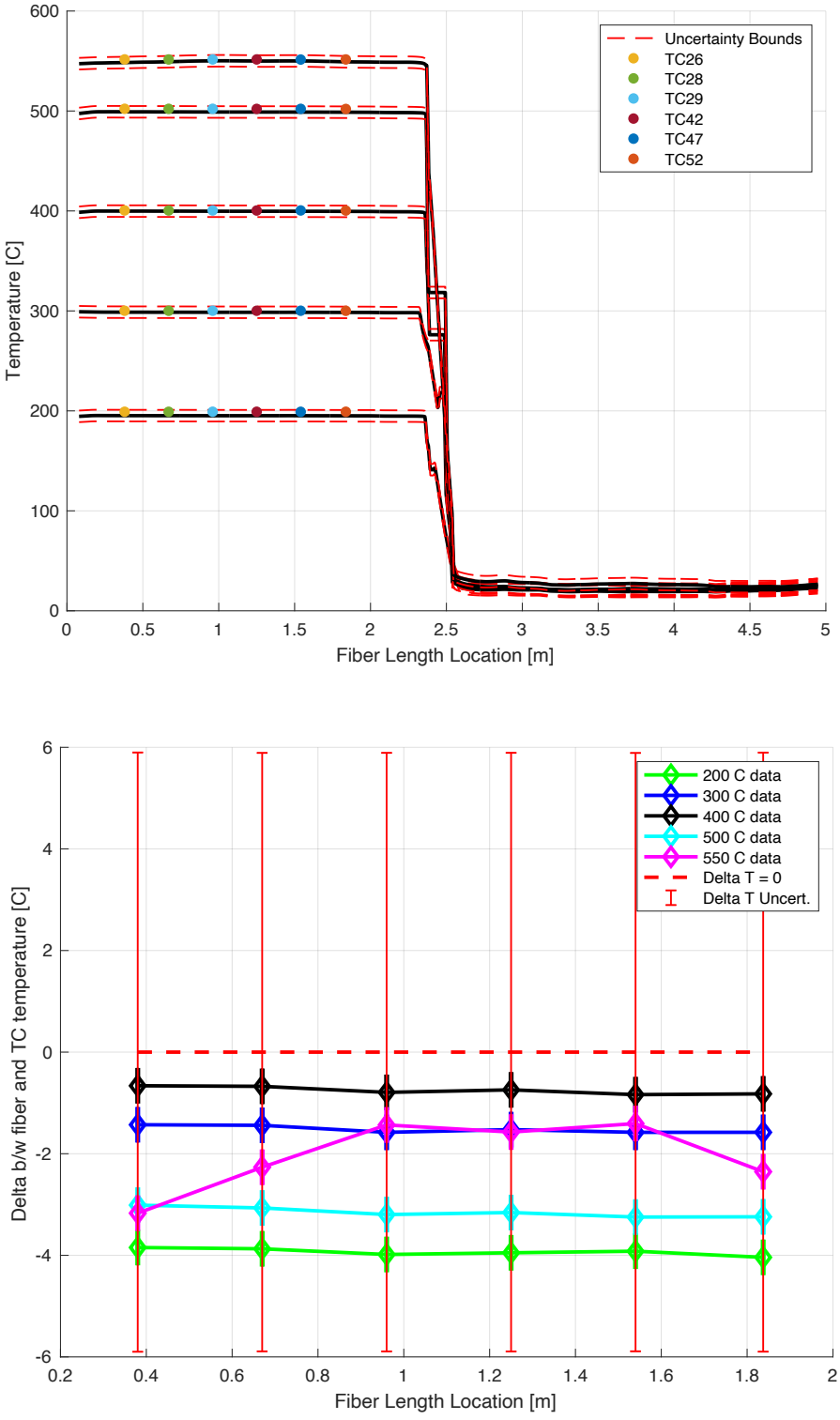

Figure 3-15: Wire wrap FOTS example validation testing plot (top) with FOTS and reference thermocouple measurements from 200 °C - 550 °C and FOTS to reference thermocouple temperature difference plot ($\Delta T = T_{FOTS} - T_{TC}$) (bottom) with uncertainty bounds.

Chapter 4 – High Temperature Distributed Fiber Optic Temperature Sensor Development

4.1 – Overview and Background

The primary objective of this research was to investigate the fundamental heat transfer behavior of liquid metal flows under conditions representative of sodium fast reactor (SFR) cores and related heat exchange components, and a key goal was the generation of highly resolved experimental datasets that could be used for validation of computational tools employed in nuclear systems design. In particular, such data could be valuable for benchmarking CFD simulations and other thermal hydraulic analysis codes used to model heat transfer in SFR systems. Achieving these objectives required the development and deployment of specialized high-resolution distributed fiber optic temperature sensor instrumentation capable of resolving temperature fields within the experimental test section.

Several of these sensors were used to obtain spatially resolved temperature measurements throughout the test section, as discussed along with the rest of the experimental setup in chapter 3. These sensors enabled detailed characterization of temperature fields within the wire wrap structure, inside the cladding of the heated fuel simulator, and within the surrounding annular flow channel. The resulting measurements aim to provide a uniquely detailed dataset for studying liquid metal heat transfer phenomena under reactor relevant conditions.

In addition to supporting the heat transfer investigation itself, the development of techniques for fabricating, installing, and operating optical fiber temperature sensors in high temperature liquid sodium environments represented a significant component of the research effort. The sensors had to be integrated into a novel experimental geometry (hollow wire wrap) while maintaining measurement accuracy and survivability under elevated temperature

conditions. As a result, considerable research and development was required to design appropriate sensor assemblies, fabrication methods, and installation procedures. For this reason, characterization of the FOTSs was also an important deliverable of this work. The fabrication techniques, along with development of a calibration method by Dr. Alastair Luna, and other investigations, resulted in a 2026 publication in the IEEE Sensors Journal, titled "Distributed Temperature Sensing Optical Fiber Resolution, Accuracy, and Response Time for High-Temperature Applications," co-authored by Dr. Tiago Moreira and others [52].

Distributed fiber optic temperature sensors represent an instrumentation technology that can provide high spatial and temporal resolution datasets in a minimally intrusive form factor. These qualities make these sensors highly desirable and valuable in engineering research in experimental thermal hydraulics and advanced nuclear reactor research. However, while this technology is well developed for low temperature use, applying these sensors in the high temperature (up to 800 ºC), high heat flux environments present in this liquid metal heat transfer study required pushing the boundaries of current materials and fabrication processes. Conventional sensor materials, especially the coatings and resins used in off-the-shelf sensors, begin to degrade at temperatures ~> 300 ºC. Additionally, the existing literature offered limited quantifications of the uncertainty, accuracy, and precision of absolute temperature measurements obtained with FOTSs, and there was no clear consensus on best practices for analyzing and reporting these errors prior to the performance analysis discussed in relation to this work and the work of others in the THL [50], [52], [53], [54], [55].

The optical fiber temperature sensors used in this research work use standard telecom fiber (typically lengths up to 10 m per channel) that is interrogated with a swept wavelength laser and interferometer system (Luna Systems ODiSI-6104). When the laser light propagates down

the fiber, some of the light can reflect off of *scattering sites* consisting of small regions in the fused silica glass with different refractive indices (e.g. water molecule impurities). Despite the extremely high purity of these glass fibers, these microscopic scattering sites exist everywhere throughout a fiber's length. The reflection mechanism at play is Rayleigh scattering (elastic scattering without change in the energy, and therefore wavelength, of the incident light). Some of this reflected light can remain trapped in the fiber core and propagate backwards toward the source (Rayleigh backscatter). This interaction is shown as a diagram in figure 4-1.

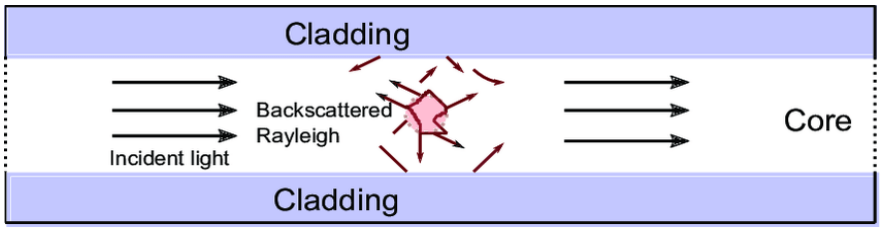

Figure 4-1: Diagram showing optical fiber with Rayleigh backscatter [65], [66].

Because the wavelength of the incident light (from the swept wavelength laser) was known at the time of emission and the wavelength does not change by scattering, the backscattered light propagating back to the source can interfere with a current reference beam in an interferometer configuration. This interference pattern is unique to a particular fiber's distribution of scattering sites, and is called the *key* of the sensor when taken at a known (typically room) temperature recorded with a reference instrument.

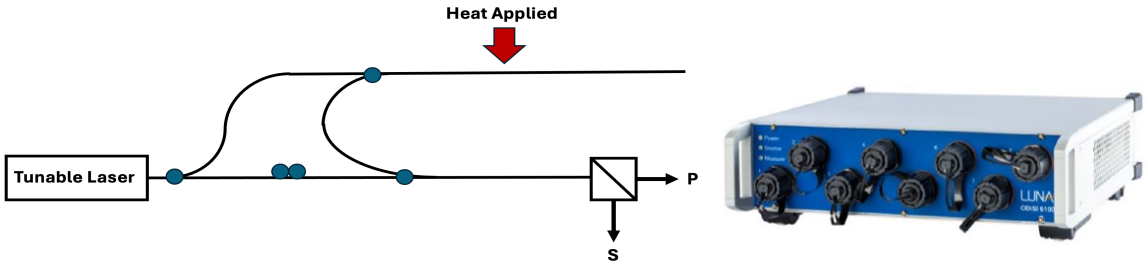

Figure 4-2: Basic swept wavelength interferometry setup diagram (left) (modified from Wolfe et al., 2005) [67] and Luna Systems ODiSI-6104 interrogator (right).

When the length of fiber is heated (or cooled) relative to the key, the scattering sites change via thermal expansion and change in electronic polarizability (thermo-optic effect). Interference patterns can again be monitored and recorded in the new elevated temperature state. The new pattern is then compared to the original key and a series of frequency-domain *spectral shift* data is generated. This spectral shift can then correlated back to local temperature at individual gage locations along the fiber's sensing length. Further background information and explanations of the optical physics used in optical fiber temperature and strain sensing methods can be found in the literature [51], [66], [67], [68].

4.2 - Fiber Optic Temperature Sensor Fabrication

The FOTS installed in the Sodium Heat Transfer Test Loop and discussed throughout this work are built using Corning SMF-28 Ultra single mode optical fiber. Each section of fiber requires an LC-APC connector at one end where it connects to the Luna ODiSI-6104's remote module and a *termination* at the other end. The fiber is shipped with an acrylate coating that is rated for < 85 °C and therefore must be stripped off for high temperature applications. A "deadended" FOTS was chosen for use in the capillary tube wire wrap due to the need to insert it into a closed ended wire wrap in this and future experimental facilities employing wire wrapped rods. The three additional internal FOTSs embedded in small 0.020 inch OD capillary tubes

under the cladding of the Stern Laboratories simulated nuclear fuel pin heater were not deadended, and the fibers were allowed to exit both the top and bottom. These three fibers were labeled SR2, SR3, and SR4. The ability to have the termination outside of the small capillaries allows for a longer and more robust termination.

FOTS construction methods were documented in new internal lab procedure documents and in reports delivered to the project sponsor. More background on optical fiber temperature sensors and their applications is available in the literature, including several papers relevant to high temperature heat transfer testing [50], [53], [54], [68].

A 10 foot long full hardened straight 316L stainless steel 0.016 inch OD x 0.010 inch ID hypodermic tube was used as the outer layer of the FOTS to be installed into a 0.056 inch OD x 0.0335 inch ID capillary tube used as the wire wrap on a simulated fuel pin. The straight hardened hypodermic tube makes sensor fabrication and insertion into the wire wrap experiment easier and more consistent compared to annealed tubing which can be easily kinked. The inside of the 0.016 inch tube was cleaned with acetone followed by 200-proof ethanol under argon gas pressure, and the ends are cut with a ceramic cutter and deburred. This outer layer stainless steel capillary also functioned as a guide tube to support the rest of the assembly process.

SMF-28 Ultra fiber was fed from a spool (#100559802565) through the 316 hypodermic tube, with an excess of 11 feet 3 inches of fiber pulled through the far side of the tube (15 inches longer than the tube). This excess length of fiber was mechanically stripped of its acrylate coating using an optical fiber stripping tool, and the *bare fiber* was carefully cleaned with acetone to ensure no fragments of the acrylate remain on the fiber. The end of the bare fiber was cleaved and a 5 mm section of bare *coreless fiber* (#fg125LA) was spliced on to the end. A thin layer of fine dried boron nitride powder is applied to the bare fiber to increase lubricity. The bare

fiber with the boron nitride lubricant is pulled back through the 316 stainless tube such that the remaining coated portion of the fiber is approximately 1/4 inch inside the 316 tube. Close-up pictures of the process of feeding the fiber through the stainless capillary tube and stripping the coating are shown in figure 4-3 (top), and cleaving and splicing on the coreless termination can be seen in figure 4-3 (bottom).

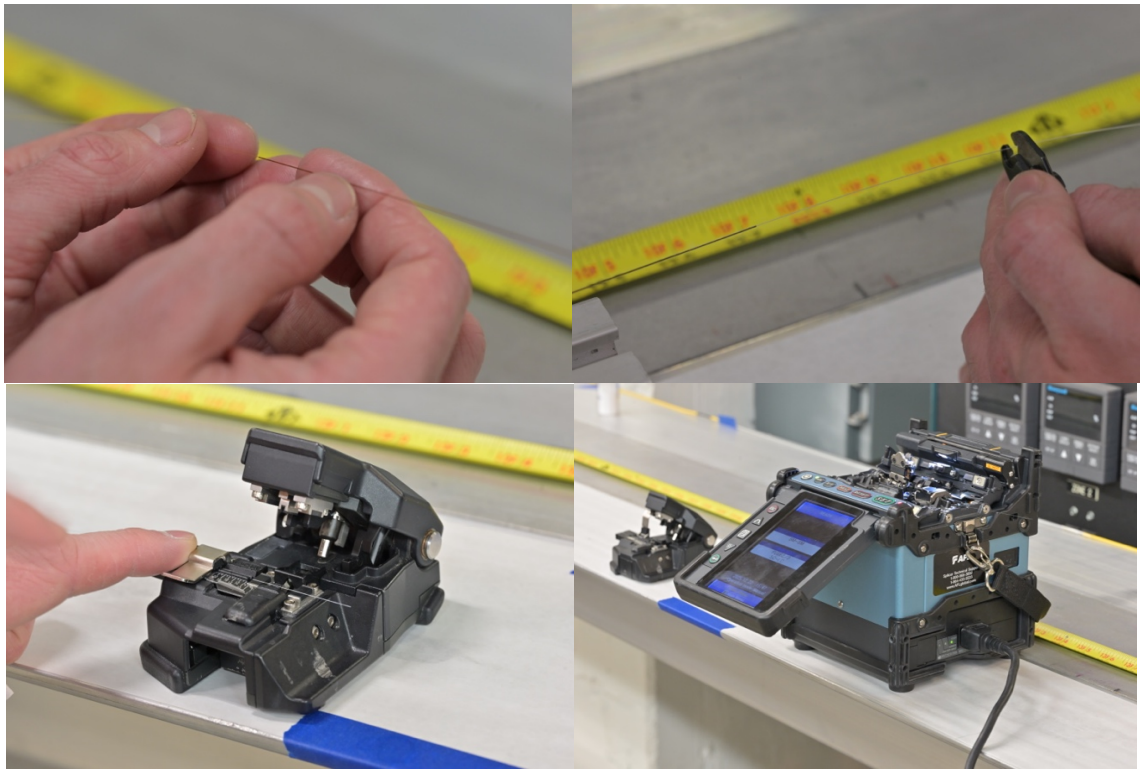

Figure 4-3: Feeding, stripping, cleaving, and splicing steps with fiber during FOTS fabrication.

An 11 foot length of Polymicro 0.0095 inch OD x 0.006 inch ID fused silica *glass capillary tube* was cut from its spool. This tube had a polyimide coating rated for < 350 °C, so that must also be removed for high temperature applications. The coating was burnt off in a tube furnace for ~15 minutes at 600 °C, and the surface of the bare glass capillary was carefully cleaned with acetone. The glass capillary is shown with its coating being stripped in figure 4-4 (left). The surface was carefully visually inspected to ensure no residue from the burnt coating

remains. The glass capillary was then fed over the exposed 15 inches of bare fiber + coreless and into the annular gap between the bare fiber and the 316 tube until the glass capillary contacts the coated part of the fiber at the end of the tube. This step is also shown in figure 4-4.

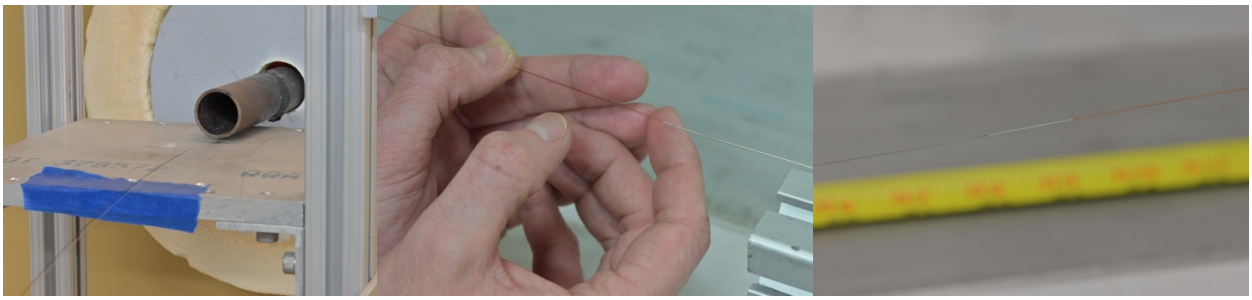

Figure 4-4: Glass capillary tube having its polyimide coating burnt off in furnace before being fed between 316 capillary tube and bare fiber.

The exposed coreless termination was polished at an angle of 9° to achieve an effective deadend termination. The mechanical angle polisher is shown in figure 4-5 (left). Lapping papers with grits between 30 µm and 0.1 µm were used, and the polishing process was refined through trial and error in order to yield the best termination quality. The quality of the termination was monitored with the Luna ODiSI-6104 during polishing. A typical successful Optical Frequency Domain Reflectometry (OFDR) trace is shown in figure 4-5 (right).

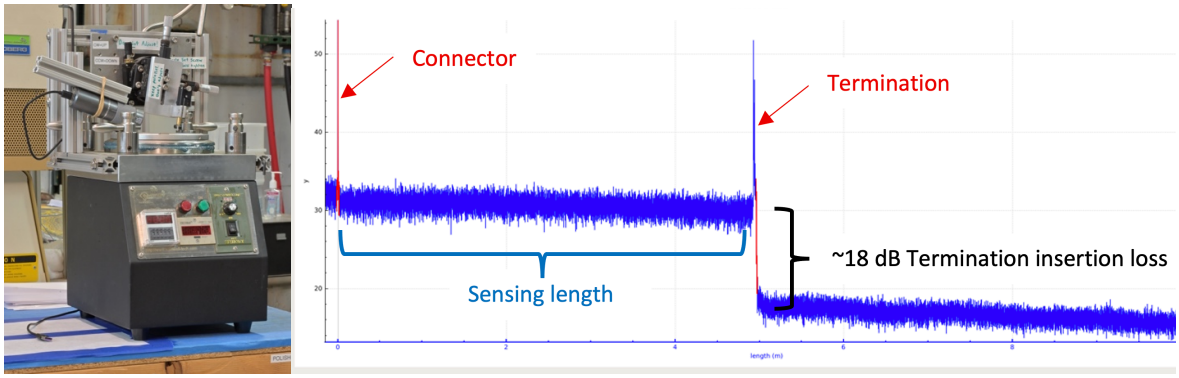

Figure 4-5: Angle polisher for terminating fiber optic temperature sensors (left) and Optical Frequency Domain Reflectometry (OFDR) plot (right) showing a good signal and termination during FOTS fabrication (a drop of at least 10db should be achieved at termination).

Figure 4-5 (right) shows reflection magnitude vs length along the fiber. The two red peaks indicate the beginning (connector) and end (termination) of the sensor. A good termination is marked by a flat profile between the connector and termination (without ripples) and a sharp step decrease in reflection magnitude after termination followed by a relatively flat profile. The step decrease should be at least 10 dB.

The sensor was completed by pulling the glass capillary over the end of the termination and sealing it by melting the end of the capillary closed with a butane torch. The two inner layers of the sensor (fiber and glass capillary) were then pulled inside the end of the 316 hypodermic tube and fixed at the opposite end with a polyimide or UV-cure resin. This step is shown in figure 4-6. The temporary connector was removed, and a permanent connector was installed with breakout tubing to protect the exposed silica capillary and fiber. The finished sensor configuration is illustrated in figure 4-7.

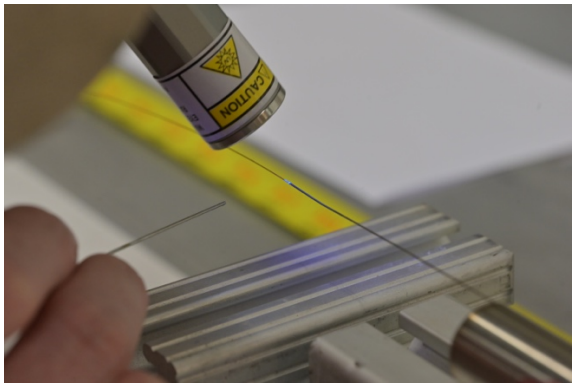

Figure 4-6: Sealing/gluing top end of FOTS during sensor fabrication.

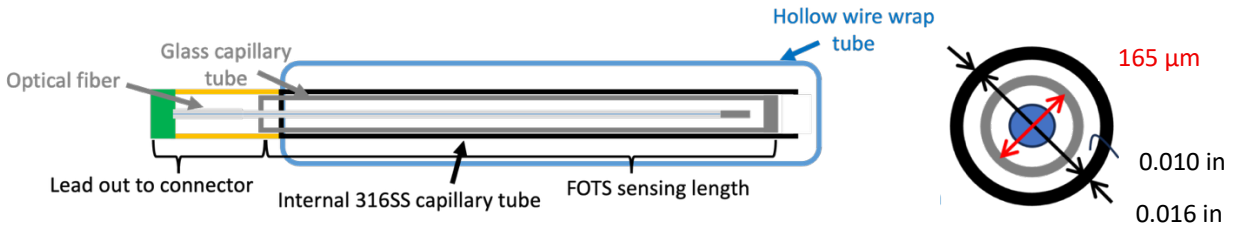

Figure 4-7: Fiber optic temperature sensor (FOTS) fabrication diagram.

The completed sensor was then subjected to a vacuum annealing process to remove residual stresses in the glass of the fiber that are present from the factory optical fiber manufacturing process. The annealing process is discussed in the following section 4.3 on Fiber Spool Calibration.

Arrival at the final fabrication methods outlined here took a lot of experimentation with different components, materials, dimensions, lubricants, and coatings to arrive at a doable, if still difficult, method that could repeatably produce robust sensors. Many FOTSs were fabricated over the course of this project for testing purposes, to replace failed sensors, and to share with project collaborators at Oregon State University.

4.3 - Fiber Spool Calibration

Prior to operation of the SHTL facility, three separate optical fiber temperature sensors were constructed from the SMF-28 Ultra spool #100559802565 fiber and loaded into a tube furnace. These fibers were used to investigate the fiber sensor annealing process and to collect spectral shift data used to develop a calibration correlation for all fiber sensors built from the SMF-28 Ultra stock. This calibration was performed by Dr. Alastair Luna [50], [52]. The process will be discussed here as it informs the uncertainty quantification methods used in this research.

The calibration furnace contained two calibrated K-type thermocouples, centrally located 8 inches apart in the 5’ long furnace, which were used to provide a reference temperature for the

FOTS calibration. After the FOTSs were loaded into the furnace, they were connected to the Luna ODiSi-6's remote modules and *keyed* in the Luna software at room temperature. The ambient temperature was measured by the average of the two reference thermocouples located in the furnace. The furnace used in calibration is shown in figure 4-8.

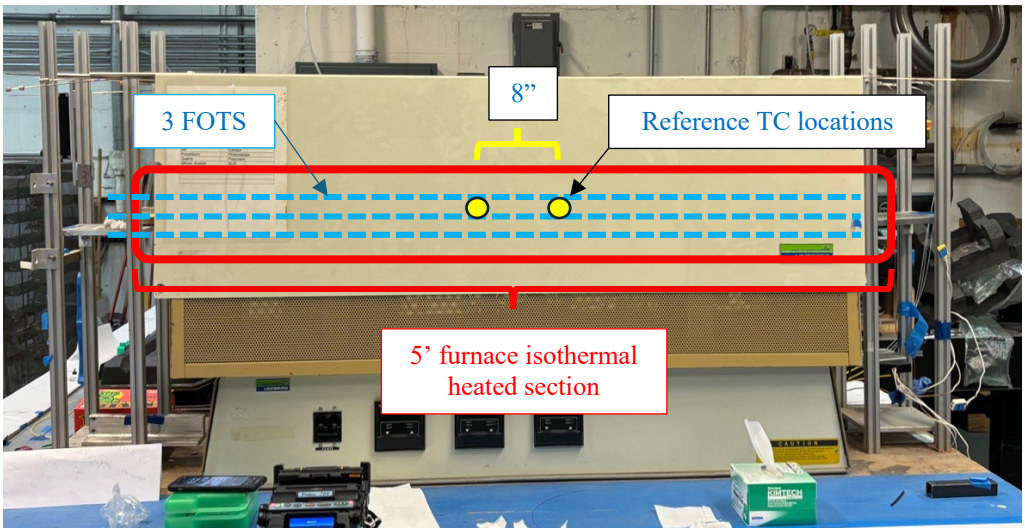

Figure 4-8: Tube furnace used for initial calibration of FOTS SMF-28 Ultra fiber spool.

To obtain a temperature calibration curve for the fibers, the spectral shift of the fibers was recorded along with temperature data from the reference thermocouples at temperatures from 50 °C to 800 °C in 50 °C increments. The furnace was then allowed to cool and the FOTS were *rekeyed* at room temperature (17.9–21.2 °C). This procedure was repeated five times to investigate the stability of the fibers' response over repeated exposures at elevated temperatures (the glass fiber structure and properties change due to the annealing of residual stresses).

The three FOTSs embedded in the SHTL fuel simulator rod (SR2, SR3, and SR4) were annealed in-situ in the sodium loop facility. This was accomplished by cycling through the setpoints 200 °C, 300 °C, 400 °C, 500 °C, and 550 °C with a 1 hour pause between each increment, and a 3 hour pause at 550 °C. This heat up and cool down cycle (200 °C → 550 °C →

200 °C) was done four times over a 48–72 hour period. This annealing process was determined to establish a stable, repeatable, and predictable spectral shift versus temperature profile for the fibers.

Alternatively, the FOTS installed in the hollow wire wrap was pre-annealed in a long tube furnace built for this purpose, prior to installation in the experiment. This procedure consists of heating the complete fabricated sensor in the tube furnace under vacuum with a 2-hour ramp up from room temperature (~17 °C) to 700 °C, followed by a 6-hour soak at 700 °C, and a slow 12-hour linear ramp down to 100 °C [50]. This procedure was found to produce similar stability in the FOTS as the in-situ method and is recommended where possible (this was not an option for the SR2, SR3, and SR4 fibers which consisted of bare glass fiber + glass capillary tube that were inserted into the already embedded stainless steel capillaries).

An initial *key* is made during the fabrication of a new FOTS probe. This key, however, may need to be overwritten after experiment operation and movements of the fiber if a drift in the baseline signal is observed (applying a new mechanical strain, bend, etc.). This *rekeying* is common during preparation for a new experimental campaign, and it ensures the baseline state of the fibers is recorded and used as the spectral shift reference state for the instrument. Rekeying must be done at a known isothermal reference key temperature (typically room/ambient temperature) which is recorded with reference thermocouples for application during a 2-step data post-processing procedure where spectral shift data is converted to the temperature domain according to a fiber calibration correlation.

The process for keying or rekeying FOTS and using the calibration correlation developed by Dr. Luna for SMF-28 Ultra spool #100559802565 requires the use of an inverse correlation to convert the reference key temperature, T_0, to the spectral shift domain (GHz) and then calculate a

spectral shift *adjustment parameter*, Adj, that can be used in the calibration correlation step. This method was shown to work well over a range of reference key temperatures from 16 °C to 250 °C.

$$Adj = -4.328 * 10^{-7} T_0^3 - 1.100 * 10^{-3} T_0^2 - 1.2145 T_0 + 26.23905 \qquad (4-1)$$

The recorded reference key temperature is used to calculate the adjustment parameter using equation 4-1. The raw spectral shift data, S, is then corrected by the adjustment parameter (S + Adj) as shown in the calibration correlation in equation 4-2, which has the coefficient values identified for SMF-28 Ultra spool #100559802565 in this fiber spool calibration work in the 5 foot tube furnace.

$$T = -7.8182 * 10^{-8}(S + Adj)^3 - 2.4957 * 10^{-4}(S + Adj)^2 - 0.7542(S + Adj) + 21.215 \quad (4-2)$$

A cubic polynomial was found to be a good fit with a low root mean square error (RMSE) over the entire calibration range (T_{room}–800 °C) (RMSE = 1.85 °C) [50], [52].

4.4 - Uncertainty Analysis

The three calibration FOTSs made from spool #100559802565 of SMF-28 Ultra fiber and tested in the tube furnace were used to obtain a correlation that is consistent throughout this spool/lot via Dr. Luna's procedure described in section 4.3. Correlated temperature data from these fibers were also analyzed in MATLAB to estimate the uncertainty of the absolute FOTS temperature measurements made via the calibration correlation in equations 4-1 & 4-2.

Simultaneous observational 95% *prediction* intervals were used. This was done to obtain limits that bound the measured temperature vs spectral shift curve with 95% confidence (± 2σ). An uncertainty of ± 5.69 °C was determined from the correlation fit over the temperature range from 17 °C to 800 °C. The independent uncertainty in the two reference thermocouples used in the calibration (± 1.1 °C over the 17 °C–800 °C range) was included in the uncertainty by adding this error in quadrature with the correlation uncertainty. These reference TCs were calibrated against an ISO 17025 certified PRT according to lab procedure. With this combined uncertainty, an estimated 95% prediction bound of ± 5.80 °C for the SMF-28 Ultra fiber optic temperature sensors was established.

It is also necessary to include the uncertainty of the TCs used to obtain the FOTS reference key temperature, T_0, during an experiment. This small uncertainty — ± 0.244 °C for the reference TCs in the SHTL test section — is included by propagating error using the partial derivative method and then adding this resulting uncertainty in quadrature with the ± 5.80 °C uncertainty mentioned above.

$$\sigma^2_{T_{refTC}} = \left(\left. \frac{\partial T(S, T_0)}{\partial T_0} \right|_{T_0 = T_{key}} \right)^2 \sigma^2_{refTC} + \cancel{(\ldots)} \qquad (4-3)$$

In equation 4-3, refTC indicates the reference thermocouple used to record the temperature at which the fiber was keyed in the experiment and T(S, T_0) comes from combining equations 4-1 & 4-2 as demonstrated in equation 4-4:

$$T(S,T_0) = -7.8182 * 10^{-8}(S - 4.328 * 10^{-7}T_0^3 - 1.100 * 10^{-3}T_0^2 - 1.2145T_0 + 26.23905)^3$$
$$-2.4957 * 10^{-4}(S - 4.328 * 10^{-7}T_0^3 - 1.100 * 10^{-3}T_0^2 - 1.2145T_0 + 26.23905)^2$$
$$-0.7542(S - 4.328 * 10^{-7}T_0^3 - 1.100 * 10^{-3}T_0^2 - 1.2145T_0 + 26.23905) + 21.215 \qquad (4-4)$$

Including all combined uncertainties yields an overall conservative uncertainty of ± 5.8046 °C ≅ ± 5.80 °C over the range of $T_{room} < T < 800$ °C for the SHTL heat transfer experiments.

The investigation showed that much of the absolute temperature measurement uncertainty is due to the cubic polynomial form of the calibration correlation when applied to such a large temperature range (~17 °C–800 °C). This is expected, and sub-correlations that are valid over narrower temperature ranges could be developed to improve upon the FOTS measurements for specific sets of desired test conditions. The cubic polynomial correlation was selected as it is broadly applicable over a wide range of conditions, can be easily corrected to work with a range of reference key temperatures, and minimal improvement in uncertainty was seen with 4th and 5th order polynomials.

4.5 - Summary and Conclusions

The FOTSs employed in the present sodium heat transfer testing work were extensively validated relative to reference TCs via isothermal operation of the SHTL facility. Discussion of these test campaigns is the subject of section 3.4. Accurate operation of the sensors was also verified by taking isothermal data at three different elevated temperature points before and after each heat transfer test campaign (separate loop fills and weeks). This verification process will be described in section 5.1.

FOTS fabrication methods, calibrations, and uncertainty analyses are documented for the SMF-28 Ultra fiber used here in the 2026 publication in the IEEE Sensors journal from Moreira et al. [52].

This investigation resulted in a reliable method for fabricating robust FOTSs that can operate at temperatures up to 800 °C in the helical wire wrap geometry with an absolute temperature uncertainty of ± 5.80 °C. Detailed reports were supplied to the project sponsor with the intent to deploy these sensors in ongoing and future larger experimental investigation at the SFR fuel assembly bundle scale, such as those at Oregon State University. Two FOTS samples were also supplied to Oregon State for test fitting and confirmation of function with their Luna Systems interrogator system.

Chapter 5 – Experimental Heat Transfer Testing Temperature Measurements

5.1 Heat Transfer Testing

Following all calibration, FOTS validation, and shakedown testing, three campaigns of steady state heat transfer testing were conducted, amounting to 36 tests in total. Power inputs ranged from approximately 7 kW to 37 kW applied through the cosine heat flux profile fuel simulator rod. These tests corresponded to sodium flow conditions within a Peclet number range of about 40 to 400. FOTS data were collected for installed sensors. Data from thermocouples and the flow meter was recorded at a frequency of 10 Hz. Isothermal testing at 200 °C, 300 °C, and 500 °C was repeated before and after each of these test campaigns to *verify* the operability of the FOTSs in the test section.

An example showing the data collected during the isothermal verification checks performed before and after each heat transfer test campaign is given in figure 5-1. This gave high confidence that the sensors performed as expected during powered testing and returned to their baseline state post-test.

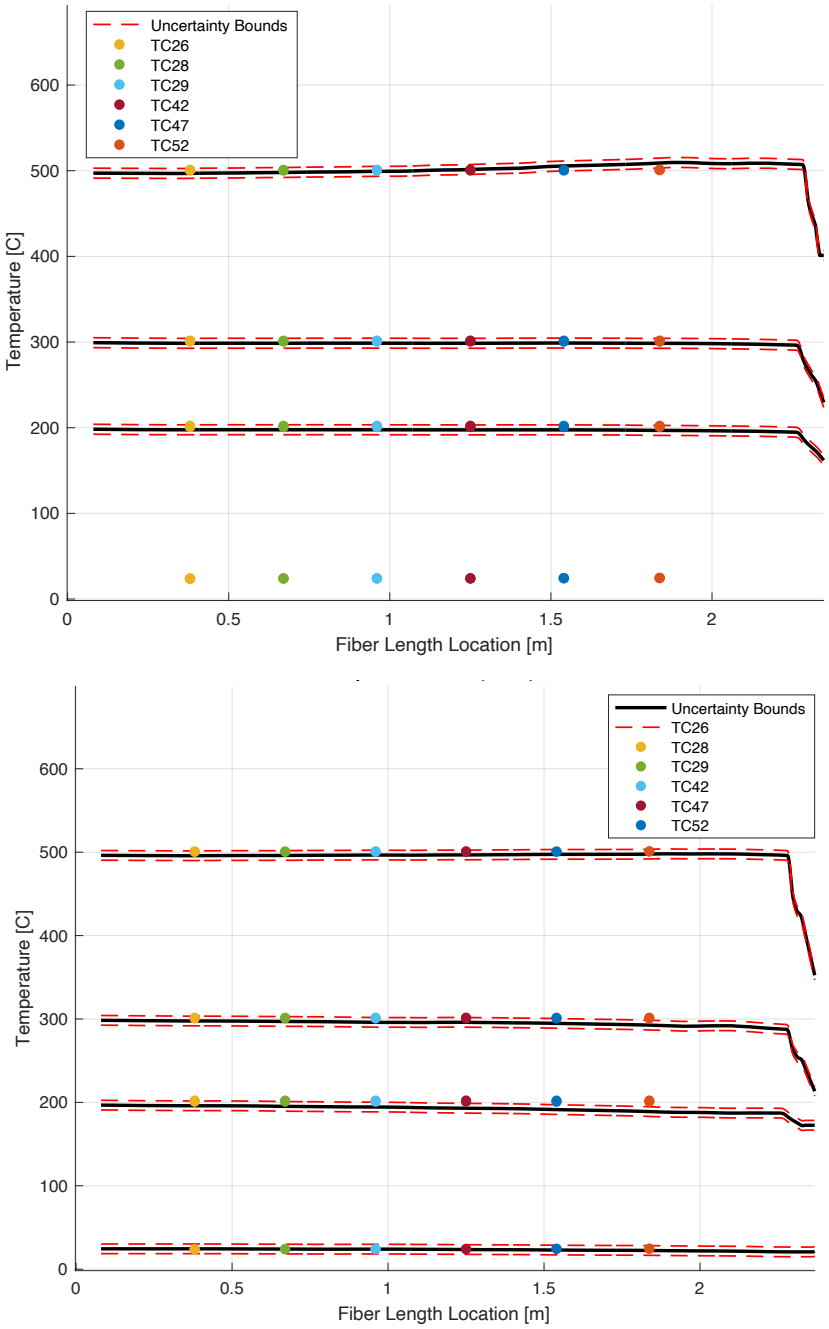

Figure 5-1: Example of isothermal validation data collected pre- (top) and post- (bottom) heat transfer test campaign (HT(3)).

The data from each powered test case were time averaged during post-processing and the conditions are listed in the test matrices in tables 5-1 to 5-3.

Table 5-1: Test matrix from HT(1) test series.

Test Case	T_{in} [°C]	T_{out} [°C]	$\dot{m}$ [kg/s]	Pe [-]	$\dot{q}$ [kW]
01	361	401	0.53	382	27.0
02	360	430	0.30	221	27.0
03	360	395	0.30	211	11.9
04	360	460	0.11	81	12.9
05	360	409	0.11	80	6.9
06	200	300	0.17	113	21.5
07	199	253	0.17	111	10.9

Table 5-2: Test matrix from HT(2) test series.

Test Case	T_{in} [°C]	T_{out} [°C]	$\dot{m}$ [kg/s]	Pe [-]	$\dot{q}$ [kW]
01	360	397	0.53	381	25.7
02	360	427	0.30	218	25.7
03	360	393	0.30	215	12.9
04	359	453	0.12	88	13.9
05	361	407	0.12	87	6.9
06	200	294	0.18	121	21.5
07	199	247	0.18	118	10.9
08	329	410	0.07	50	7.1
09	272	436	0.07	50	13.9
10	328	396	0.20	142	17.7
11	310	398	0.20	142	22.9
12	361	396	0.30	216	13.5
13	322	406	0.30	214	32.6
14	375	405	0.39	281	15.0
15	362	402	0.40	290	20.1
16	352	428	0.30	217	29.7

Table 5-3: Test matrix from HT(3) test series.

Test Case	T_{in} [°C]	T_{out} [°C]	$\dot{m}$ [kg/s]	Pe [-]	$\dot{q}$ [kW]
01	360	398	0.53	383	25.7
02	360	426	0.30	221	25.7
03	360	393	0.30	219	12.9
04	360	453	0.12	83	13.9
05	361	405	0.12	85	7.0
06	201	298	0.18	116	21.5
07	199	247	0.18	114	10.9
08	299	452	0.07	47	13.2
09	243	432	0.07	49	17.0
10	286	403	0.21	147	31.4
11	397	414	0.39	285	9.1
12	332	407	0.20	144	19.4
13	256	419	0.18	127	36.8

5.2 - Wire Wrap and Axial Temperature Profiles

Representative plots of the collected data are shown in figure 5-2. The horizontal axis indicates the axial position along the test section with the origin at the sodium inlet and increasing in the direction of upward flow. The beginning and end of the 2 m heated length, as well as the locations of five sets of locating pins that maintain rod centering, are marked. The vertical axis represents temperature. Steady state temperatures recorded from various instruments throughout the test section are displayed, including the primary FOTS installed in the hollow wire wrap; internal FOTSs embedded beneath the fuel simulator cladding; inlet, outlet, and intermediate thermocouples; and approximate flow-area-weighted average temperatures measured by the three transverse FOTSs passing through the test section. The analysis here will focus on one test case as a characteristic example, but data plots for all test cases can be found in appendix B.

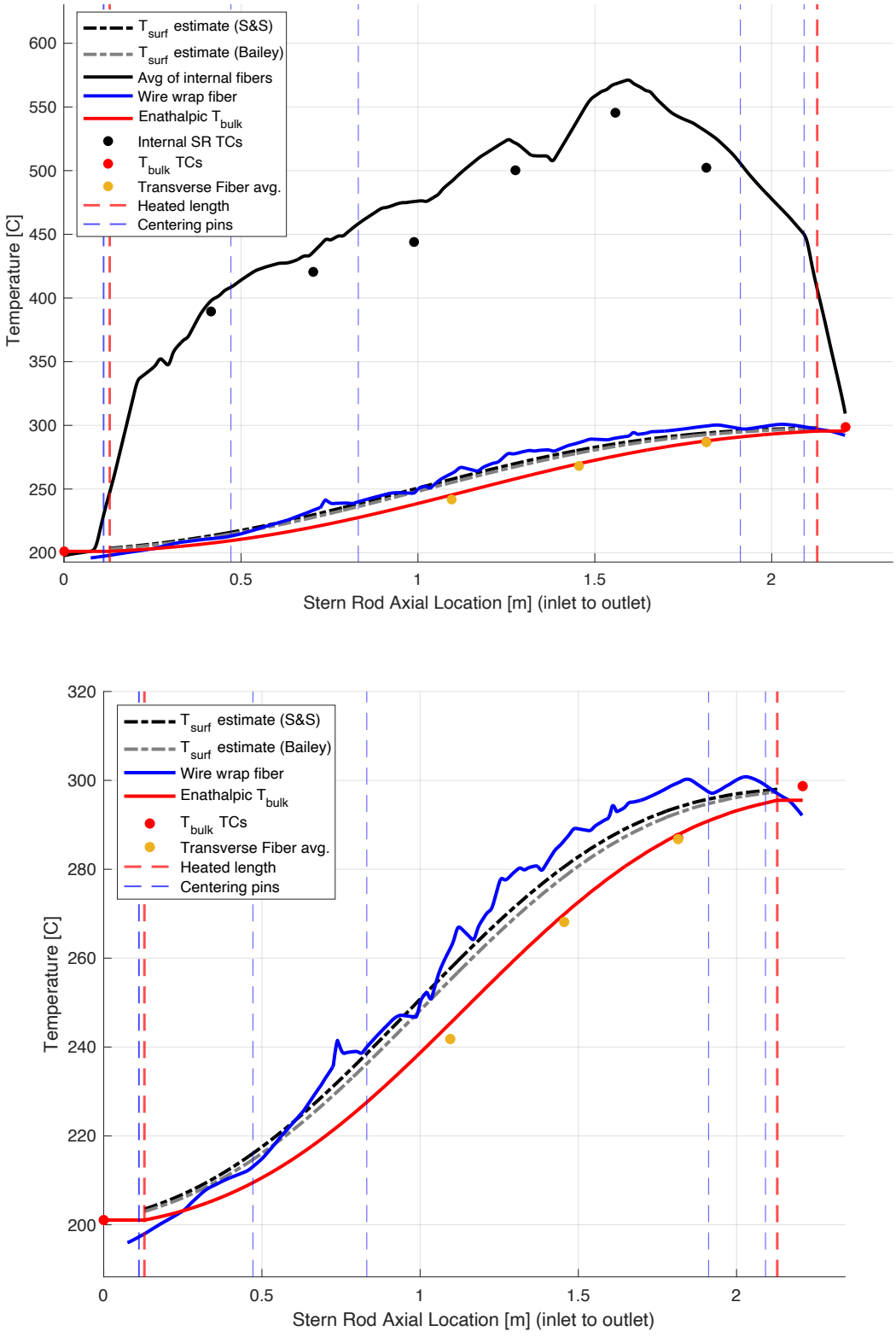

Figure 5-2: Example of HT(3) Test Case 06 temperatures (Pe = 116) (top) with zoom in to wire wrap measurements (bottom) and predicted surface temperatures.

5.3 - Radial and Bulk Temperature Measurements

In addition to the resolved temperature data from the internal fuel rod simulator FOTSs and the wire wrap FOTS of primary interest, data was also recorded from the transverse FOTS that crosses through the sodium flow channel at three different axial heights. These data from a representative test case are displayed in figure 5-3 (left). The temperatures at each of the seven fiber gage locations across the test section span are plotted along the linear dimension of the sensors.

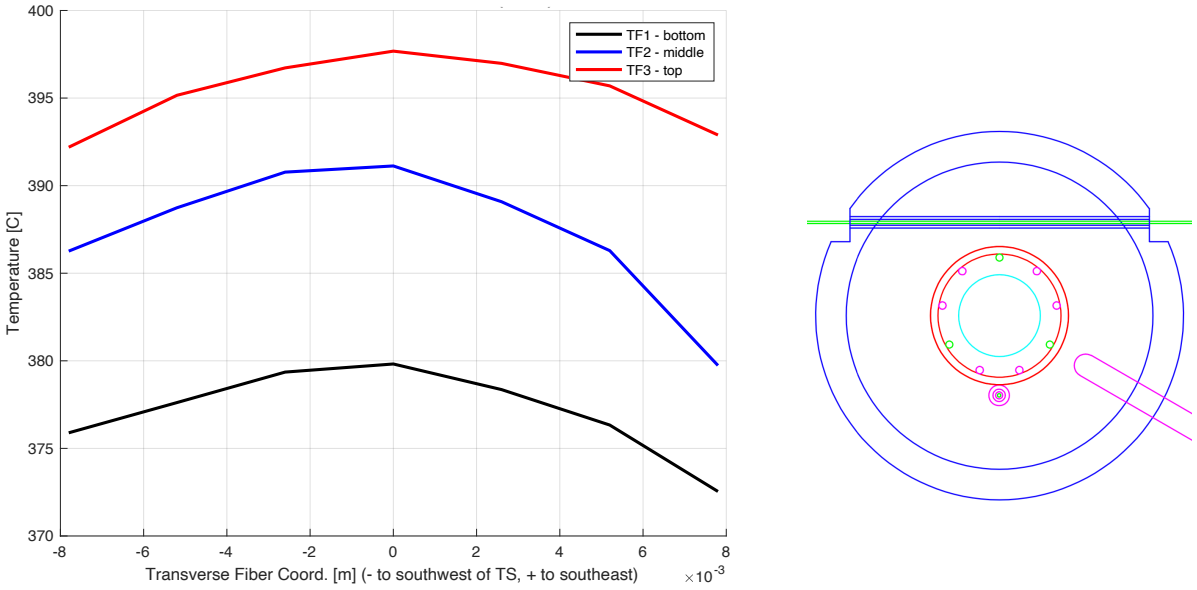

Figure 5-3: Transverse FOTS measurements plotted linearly (left) for HT(3) Test Case 01 and diagram of test section cross-section (right).

Figure 5-4 shows the same transverse FOTS data now mapped onto the radial dimension of the test section. The plot also has the local wire wrap FOTS temperature measurements overlaid, and the radial positions of the rod surface and the wire wrap centerline are indicated. The three transverse passes (black, blue, and red solid lines) show two temperatures for each radius value besides the radius nearest to the rod surface. This is because the sensor cuts across the entire section and measures temperature data on each side of its nearest pass to the fuel

simulator (see figure 5-3, right). It is also noticeable that the radial profiles are not perfectly symmetrical. This is likely largely due to limits on how well the location of each gage (spaced every 2.6 mm along the FOTS) can be known. The possibility of a swirling flow induced by the twist direction of the wire wrap was also considered and may play a minor roll (this is investigated further in chapter 7).

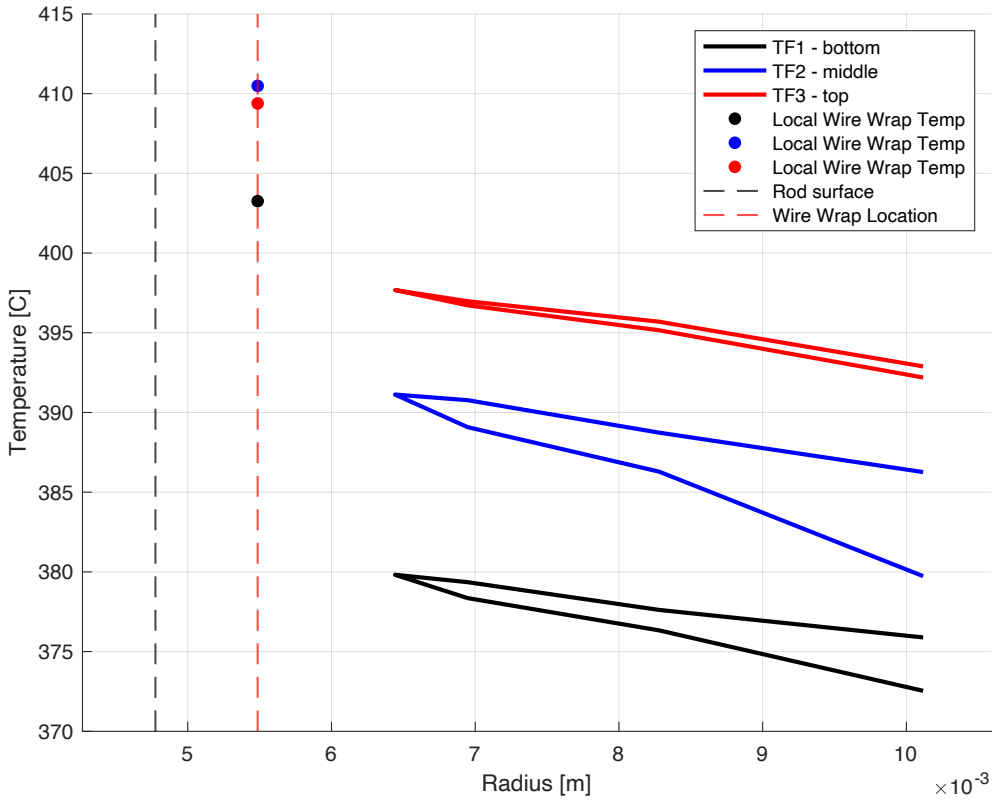

Figure 5-4: HT(3) Test Case 01 transverse FOTS measurements plotted radially.

A significant temperature gradient can be observed throughout the annular sodium channel, particularly when considering the local wire wrap FOTS temperature data points too. This behavior reflects the thermal transport characteristics of liquid metals discussed in chapters 1 and 2, and also gets at some of the challenges of characterizing their heat transfer with dimensionless correlations. Thermal diffusivity in liquid metals is much larger than momentum

diffusivity (resulting in comparatively thick thermal boundary layers). As a consequence, temperature gradients are not confined to a narrow region near the heated surface, as is often the case in conventional turbulent flows with higher Prandtl number fluids where the bulk temperature is homogenized throughout the core of the channel by advection. Instead, thermal diffusion allows the temperature field to extend significantly into the bulk flow, producing measurable radial temperature variations across the annular channel even under turbulent flow conditions. This behavior is expected at the low to moderate Peclet numbers of interest and the measured profiles are demonstrative of the difficulties in measuring a bulk temperature of heated liquid metal internal flows with a single point instrument.

In this vein, the temperature data from the transverse FOTS were also area-averaged to estimate bulk fluid temperatures at the three axial locations where the sensors intersect the flow. For this calculation, a constant axial sodium velocity equal to u_{mean} was assumed throughout the annular channel, simplifying the bulk temperature approximation. This assumption was considered acceptable based on the close agreement between the resulting bulk temperature estimates and the curve obtained from an incremental energy balance along the test section. The assumptions and tools used to perform the area-weighted average bulk temperature estimates are overlaid on figure 5-5. The average temperature at each radial location on the transverse FOTS was used and the boundaries of the temperature profile were closed under the assumption that the local wire wrap probe measurement is representative of the local heater surface temperature and that the largest radius temperature measurement extended to the inside of the test section wall.

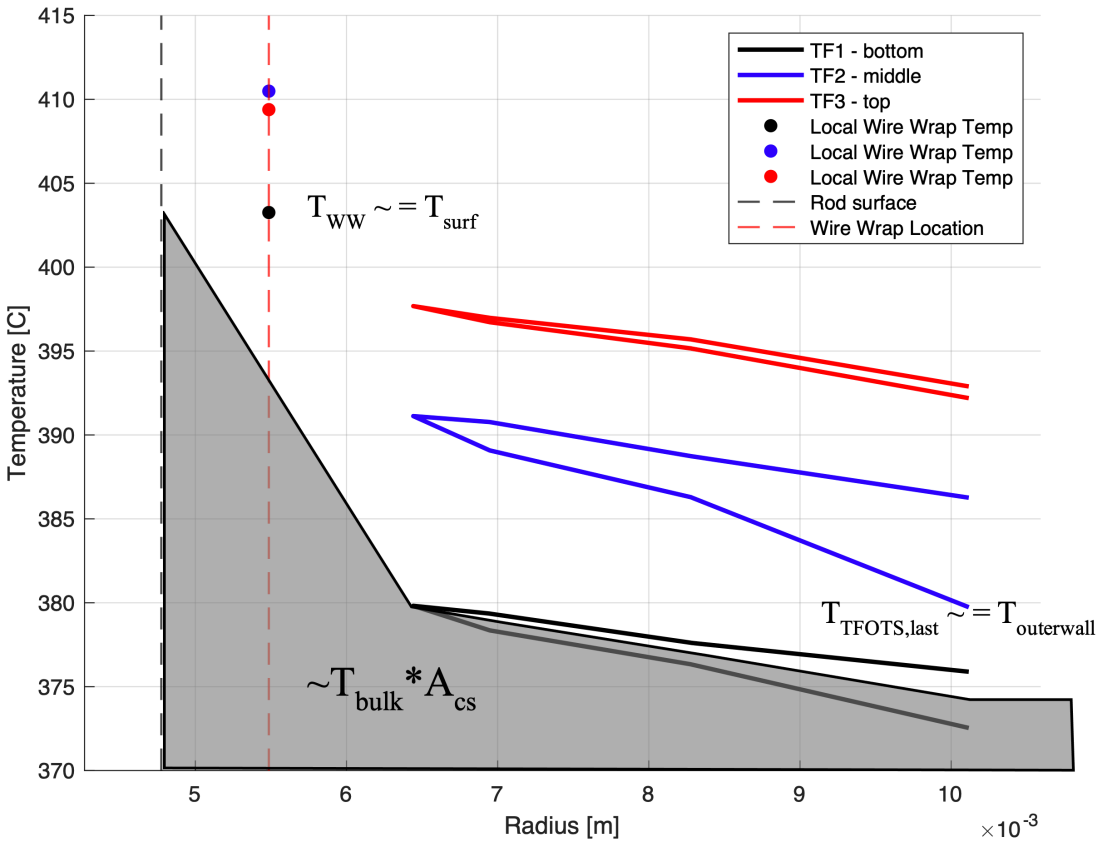

Figure 5-5: HT(3) Test Case 01 radial transverse FOTS measurements with area-weighted average bulk temperature estimation information overlaid.

Furthermore, a simple arithmetic average of channel temperatures also yielded results within approximately 4 °C of the area-averaged estimation in this representative case. Figure 5-6 compares bulk temperature estimates obtained from an incremental energy balance (solid red line), area-weighted average using transverse FOTS data (cyan), arithmetic average of transverse FOTS data (yellow), and a single point TC fluid temperature measurement at the same axial location as the top transverse FOTS pass (red point).

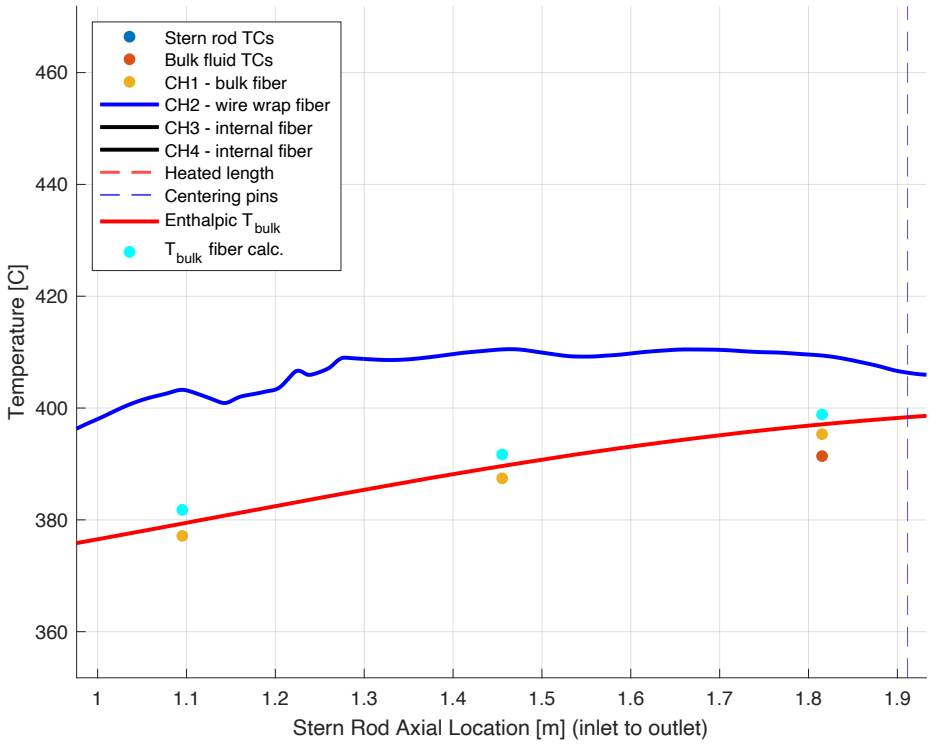

Figure 5-6: Example plot showing multiple methods for estimating local average fluid bulk temperature using the dataset from HT(3) Test Case 01.

Chapter 6 – Analysis of Heat Transfer Behavior

6.1 - Observed Temperature Profile Behavior

The experimental heat transfer results reveal several notable features in the measured temperature distributions. In particular, the temperature profiles obtained from the wire wrap FOTS exhibit a jagged structure along the axial length of the test section rather than a smooth shape. Similarly non-smooth behavior is observed in the temperature data recorded by the fiber sensors embedded within the heater rod, appearing consistently across multiple test campaigns conducted on different days and sodium loop fills. While an ideal cosine heat flux distribution would be expected to produce a smooth axial temperature profile, the extensive validation and pre- and post-test verification procedures performed on the fiber optic sensors provide confidence that the measurements represent the actual local temperatures rather than artifacts of sensor error or mechanical strain induced temperature measurement bias [52].

6.2 - Causes of Local Temperature Variations

Measurements in liquid sodium are inherently challenging because the fluid removes heat very efficiently from the rod surface. The high thermal conductivity of sodium and the large power inputs required to generate measurable wall-to-bulk temperature differences can make the resulting temperature field sensitive to small geometric or material variations within the heater assembly (internal conduction resistances become significant compared to the very low convection resistance). Consequently, relatively small manufacturing nonidealities in the heater rod have the potential to produce measurable variations in the local temperature distribution. Based on analysis of the experimental configuration, three primary mechanisms were identified as potential contributors to the observed temperature variations: eccentricity of the heater

filament within the fuel rod simulator, positional uncertainty of the wire wrap FOTS probe within the capillary tube, and spatially varying thermal contact resistances between the layered components of the heater assembly.

The heater filament, fabricated from a helically machined Inconel 718 tube with a wall thickness of 0.020 inches, serves as the resistive heating element. According to the manufacturer's specification, the filament is positioned concentrically within the heater sheath, which consists of a Monel K500 layer beneath the swaged outer cladding, to within ±0.010 inches (0.25 mm) relative to the sheath layer. A schematic cross-section of the nominal heater rod construction is provided in Figure 6-1. The filament is electrically isolated from the sheath by a packed boron nitride (BN) insulating sleeve with a nominal radial thickness of 0.0225 inches. Consequently, a positional offset of 0.010 in represents nearly a 50% reduction in the BN layer thickness on the displaced sides of the filament, corresponding to an approximate 13% decrease in the total radial conduction path between the filament outer surface and the rod cladding. This geometric sensitivity highlights the potential for measurable circumferential variations in applied surface heat flux should small manufacturing offsets be present.

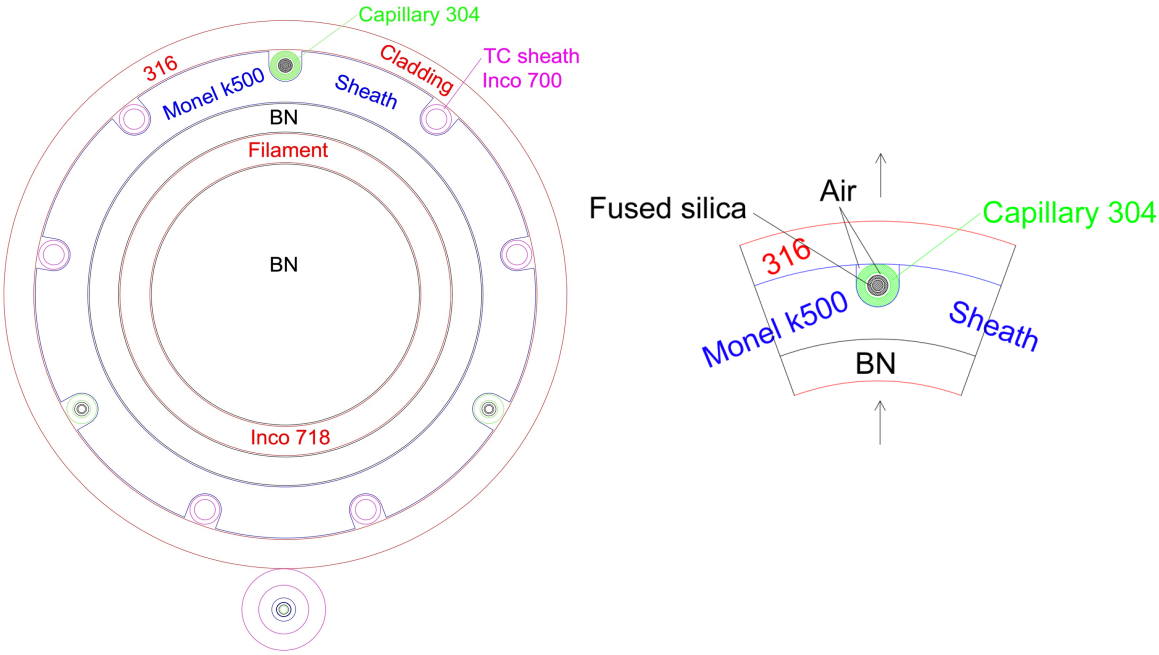

Figure 6-1: Fuel simulator rod cross-sectional diagram.

The potential significance of such geometric variation is highlighted by the large temperature differences measured between the internal fiber sensors and the wire wrap sensor located at the rod surface. As shown in figure 5-2, temperature differences on the order of 200 °C can be sustained. Under these conditions, relatively small changes in internal conduction path length could substantially alter the local heat flux reaching the rod surface.

The effect of the position of the wire wrap FOTS probe inside the hollow wire wrap was also considered. Installation of the pre-assembled fiber sensor required clearance between the sensor and the receiving tube. The inner diameter of the wire wrap is 0.0335 inches, while the outer diameter of the FOTS assembly is approximately 0.016 inches, allowing the sensor to shift within the capillary. In practice, the sensor position likely varies between its bounds as the wire wrap winds along the rod, influenced by thermal expansion of the test section and elastic tension in the FOTS capillary tube.

To evaluate these two effects (heater filament concentricity and wire wrap FOTS positional uncertainty), finite element (FEA) models were developed in ANSYS Mechanical. Two two-dimensional geometries representing the cross-section of the fuel simulator were created with the heater filament displaced by 0.010 inches toward and away from the wire wrap location. The wire wrap FOTS probe was also offset to either the innermost or outermost positions within the wire wrap tube that houses it in either model, respectively. Secondary features such as embedded thermocouples, the helical cut in the filament, and the internal composition of the wire wrap were simplified. Sensitivity studies demonstrated that the predicted wire wrap temperature changed by only 1-2 °C when the wire wrap gap or fill region was modeled as air, boron nitride, or stainless steel. When boundary conditions corresponding to the HT3TC06 test case (figure 5-2) were applied, the simulations indicated that the compounded geometric offsets can produce significant temperature variations at the wire wrap probe location. The model predicted wire wrap FOTS temperatures ranging from 266 °C to 249 °C for the “hot’’ and “cold’’ eccentric configurations, respectively (figure 6-2).

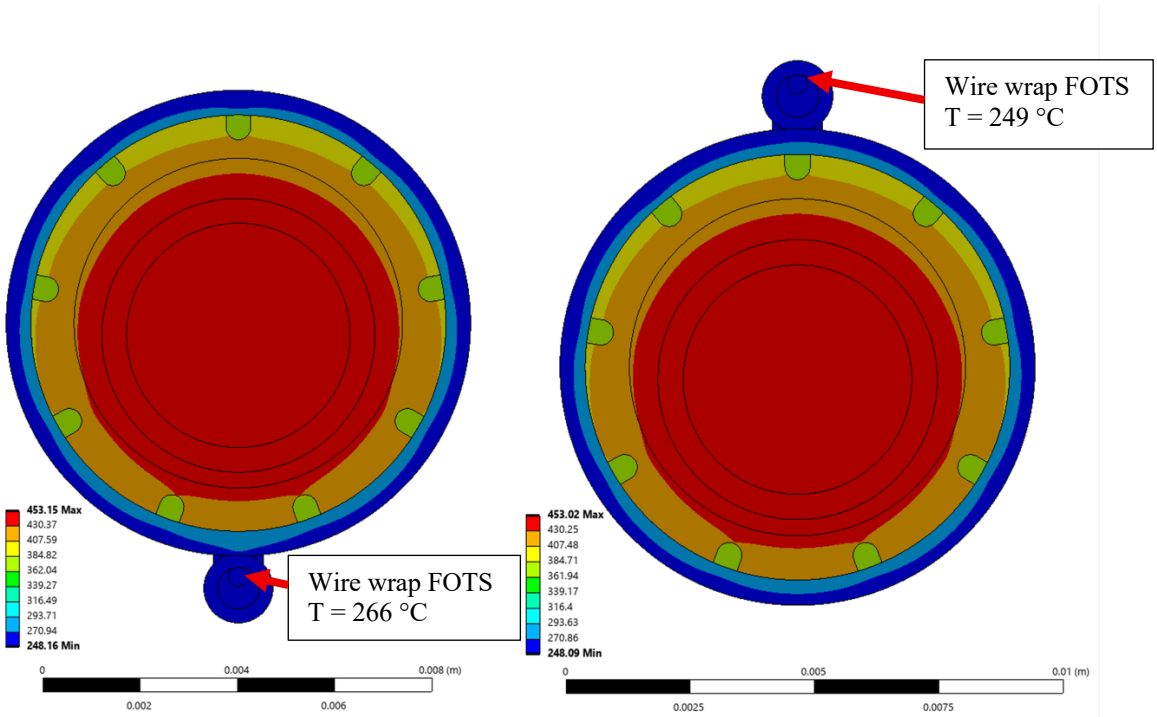

Figure 6-2: 2D ANSYS filament concentricity and wire wrap sensor position variability temperature results for the "hot" (left) and "cold" (right) configurations.

To further examine these mechanisms, three-dimensional finite element models were developed that also incorporated both filament eccentricity and wire wrap sensor positional variation. As with the 2D case, two geometries were created with the heater filament displaced to one side by 0.010 inches and with the wire wrap FOTS probe following its innermost or outermost path inside the wire wrap. These higher-fidelity geometries included the helically cut heater filament and a full wrap of the wire wrap in three dimensions, allowing for the inclusion of axial conduction effects and the evaluation of circumferential variation in temperature as the wire wrap traverses the rod surface.

For the configuration with the filament offset by 0.010 inches and the wire wrap sensor located at the innermost position, the predicted sensor temperature varied from 259 °C to 264 °C as the wire wrap moved from the low heat flux side of the rod to the high heat flux side over half of a wrap pitch (9 cm into-the-page along the axial direction of the heater rod in figure 6-3).

When the sensor was located at the outermost position, the predicted range was 250 °C to 254 °C over the same distance (figure 6-3, left). Consequently, the total range of accessible measured temperatures over one half wrap pitch (9cm) is ~250 °C to 264 °C – a similar result to that from the 2-dimensional models.

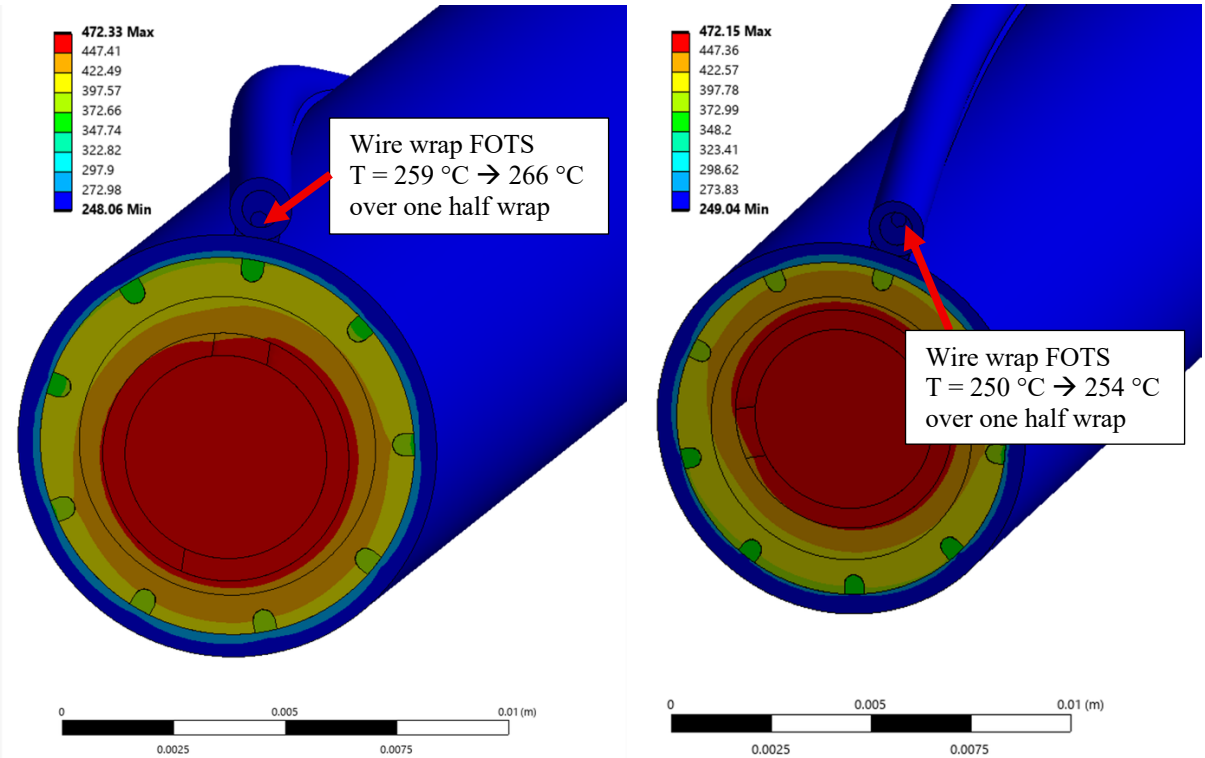

Figure 6-3: 3D ANSYS results filament concentricity and wire wrap sensor position variability temperature results.

In addition to geometric factors, thermal contact resistances between the layered components of the heater assembly are also expected to influence the measured temperature distribution. The heater rod contains multiple internal interfaces where imperfect thermal contact may occur, especially between the cladding, sheath, and embedded sensors. These contact resistances can modify the conductive heat transfer path and therefore affect both internal and surface temperature measurements.

The significance of this effect is suggested by the large temperature differences observed between the embedded fiber sensors and the wire wrap FOTS on the rod surface (on the order of 200 °C in the HT3TC06 test case shown in figure 5-2). In contrast, finite element simulations assuming perfect thermal contact between layers predict temperature differences of ~80 °C under similar operating conditions. While spatially uniform thermal contact resistances would only shift the *internal* temperatures in the heater, spatial variations in this resistance can locally modify the heat flux reaching the rod surface and therefore the surface temperature. Simple thermal resistance estimates indicate that contact resistances equivalent to the conduction resistance of an approximately 0.0001 inch thick air gap could change the surface-to-embedded-sensor temperature difference by amounts on the order of 100 °C in some cases. Considering that the cladding layer itself is only 0.020 inches thick, such small variations in internal thermal resistance can significantly influence the measured surface temperature distribution.

6.3 - Interpretation of Temperature Variations

Taken all together, these results demonstrate that relatively minor manufacturing tolerances and changes in interface contact conditions, such as those caused by thermal expansion during operation, can have a measurable impact in liquid metal heat transfer experiments where convective resistance at the surface is comparatively small.

Examination of the wire wrap temperature profile for the representative test case (figures 5-2, 6-4) shows local temperature variations on the order of approximately 5-10 °C occurring over axial distances of roughly 8-12 cm. While the temperature profile is not strictly periodic, the characteristic length scale of these variations is comparable to the geometric scale of the wire wrap pitch itself. In the test section, the wire wrap half-pitch is 9 cm, meaning that the sensor

traverses 180 degrees azimuthally over that axial distance. The FEA models described above indicate that variations in heater filament eccentricity and wire wrap sensor position can produce surface temperature differences of a comparable magnitude as the wire wrap moves circumferentially around the rod. When combined with possible spatial variations in contact resistance within the heater assembly, the resulting superposition of effects provides a plausible explanation for the magnitude and spatial scale of the temperature variations observed in the experimental data.

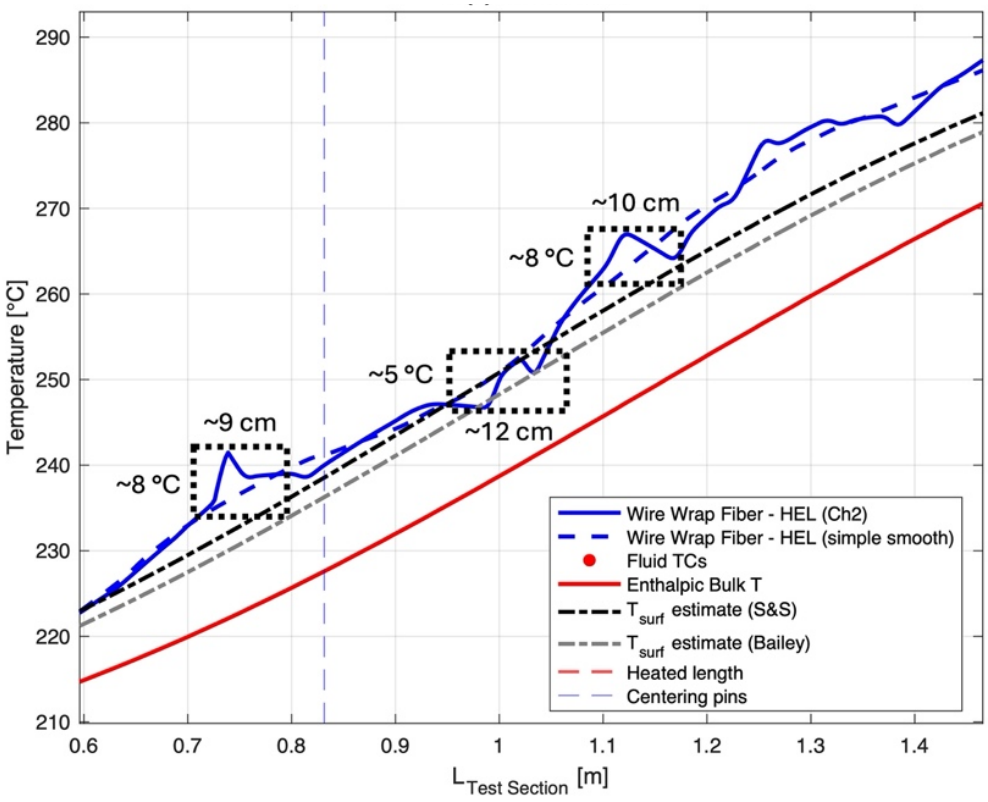

Figure 6-4: Close-up of wire wrap FOTS temperature profile and scale of temperature variations from HT(3) Test Case 06.

Additional confidence that the observed wire wrap temperature variations represent real physical features of the thermal field rather than random measurement noise is provided through comparison of similar structure in wire wrap temp profiles over repeated test cases and multiple experimental campaigns. Figure 6-5 shows three separate realizations of the same two nominal operating conditions collected using two different wire wrap FOTS installations. The overall shape and local structure of the temperature profiles remain highly consistent between tests, including the locations of many local temperature peaks and depressions along the axial direction. This repeatability indicates that the measured fluctuations are strongly influenced by persistent physical effects within the test section, including internal heater filament eccentricity, and conjugate heat transfer pathways within the fuel simulator rod and wire wrap assembly.

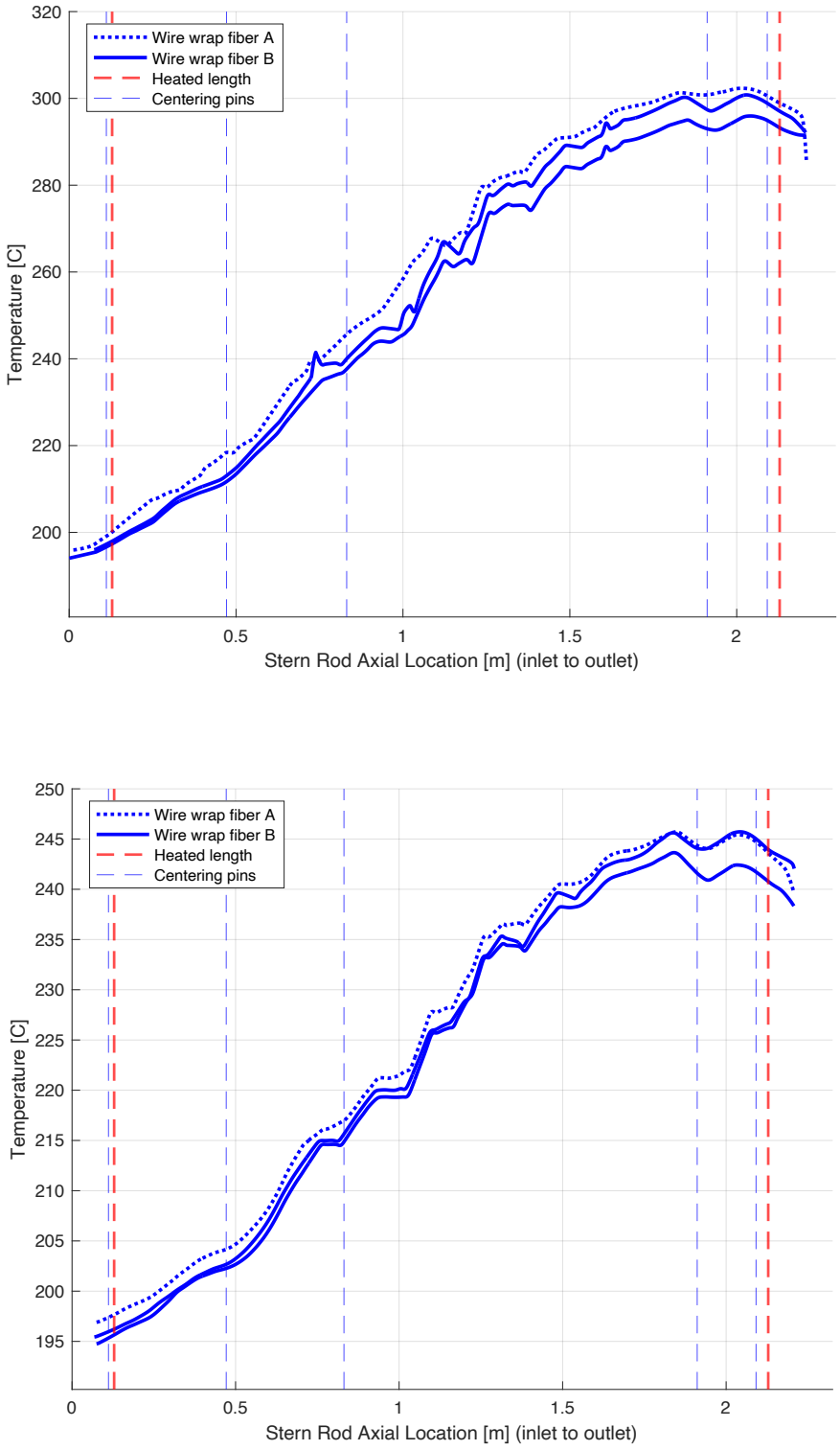

Figure 6-5: Comparison of wire wrap FOTS traces from repetitions of nominal test cases TC06 (top) and TC07 (bottom).

At the same time, smaller differences between traces are also evident and are consistent with the expected sensitivity of the measurement to local sensor positioning within the hollow wire wrap capillary tube, as discussed previously and further investigated in Chapter 7 through CFD modeling, in addition to FOTS uncertainty. Minor differences in the installed position of the fiber within the wire wrap or small positional shifts during operation can alter the local thermal resistance between the rod surface, wire wrap, and sensor, contributing to the variations in measured local temperature. The persistence of the broader temperature profile structure across repeated experiments nevertheless supports the conclusion that the underlying thermal behavior within the sodium cooled geometry is being captured consistently.

6.4 - Overall Heat Transfer Analysis

While the measured real local temperature variations complicate a local heat transfer analysis, it is still possible to characterize the overall heat transfer behavior of the system. The total electrical power input to the heater is well known, and the nominal axial heat flux distribution is constrained by the geometry of the resistive filament, which produces a cosine-shaped profile along the heated length. Consequently, while local heat flux and temperature at the rod surface may vary due to geometric effects, the average heat flux over an axial region must remain consistent with the imposed power input. This observation motivates the use of windowed smoothing and/or spatial averaging when analyzing the temperature data.

Windowed spatial smoothing will be discussed first. Several methods were investigated: a simple moving average with a spatial smoothing window size of one wire wrap pitch (18 cm), a physically meaningful curve fitting forcing the surface-to-bulk temperature difference to be proportional to the nominal local heat flux throughout the central developed flow portion of the

test section (equivalent to a constant Nusselt number condition), and a 50/50 blended weighted-averaging of the proportional curve fit with the raw wire wrap data. Figure 6-6 shows the three smoothed curves overlaid with the raw temperature data for the representative example test case (HT3TC06).

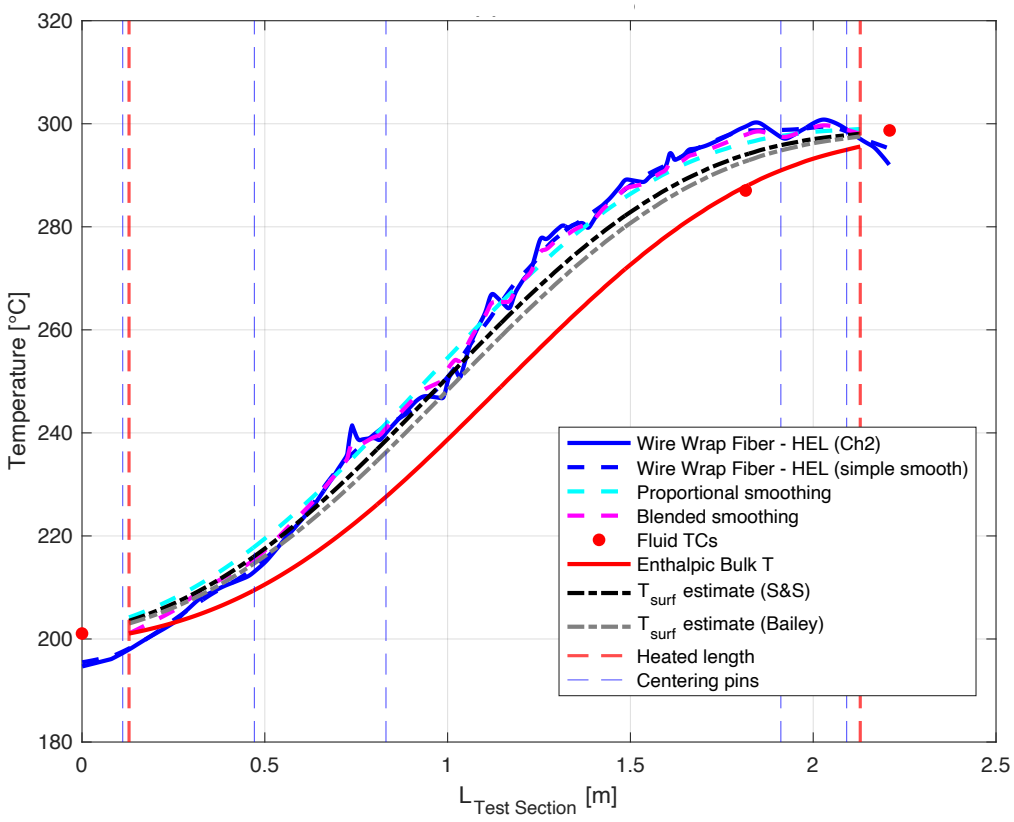

Figure 6-6: Example of smoothed wire wrap temperature data for HT(3) Test Case 06 (Pe = 116).

In the present analysis, the temperature measured by the wire wrap FOTS is taken to approximate the local rod surface temperature ($T_{\text{wire wrap}} = T_{\text{surf}}$). The bulk fluid temperature profile is obtained from an incremental energy balance using the known electrical power input to the heater rod. Together with the assumed cosine-shaped axial heat flux distribution, this allows local temperature differences and heat flux values to be determined along the heated length. Heat transfer coefficients are then calculated using Newton's law of cooling:

$$h = \frac{\dot{q}''}{T_{wire\ wrap} - T_{bulk}} \qquad (6-1)$$

Nusselt numbers are subsequently calculated as:

$$Nu = \frac{hD_e}{k_f} \qquad (6-2)$$

where D_e is the equivalent hydraulic diameter of the annular flow channel and k_f is the thermal conductivity of liquid sodium.

A series of "local" Nusselt numbers can therefore be calculated from the smoothed wire wrap temperature data curves. Figure 6-7 thorough 6-9 show Nusselt numbers for all three smoothing methods for 28 of the 36 total test cases. Test cases with low power/low heat flux were excluded from this analysis as the heat fluxes were not large enough to generate significant measurable wall-to-bulk temperature differences in the sodium, resulting in large uncertainties, as discussed below in the overall average Nu analysis.

The Nusselt numbers are plotted linearly along with the Seban & Shimazaki and Bailey annular correlations in the top plots of figure 6-7 through 6-9 and on a log-log plot overlaid with the historical liquid metal heat transfer data first presented in figure 2-1 in the bottom plots of figure 6-7 through 6-9 [27], [39], [42], [69].

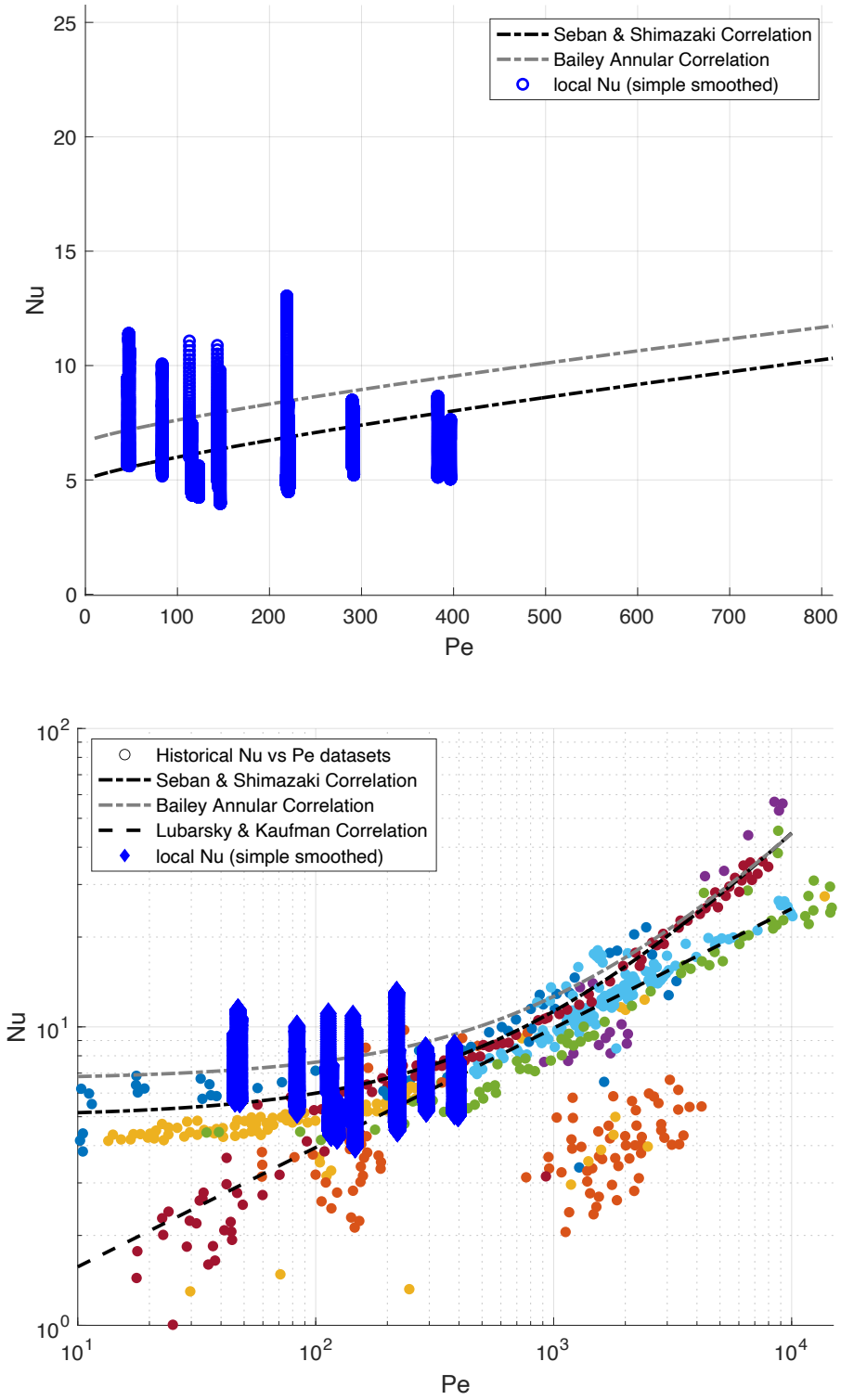

Figure 6-7: Nusselt number measurements using simple moving average filtered wire wrap FOTS data compared to correlations on a linear plot (top) and compared to historical data sets on a log-log plot (bottom) [36].

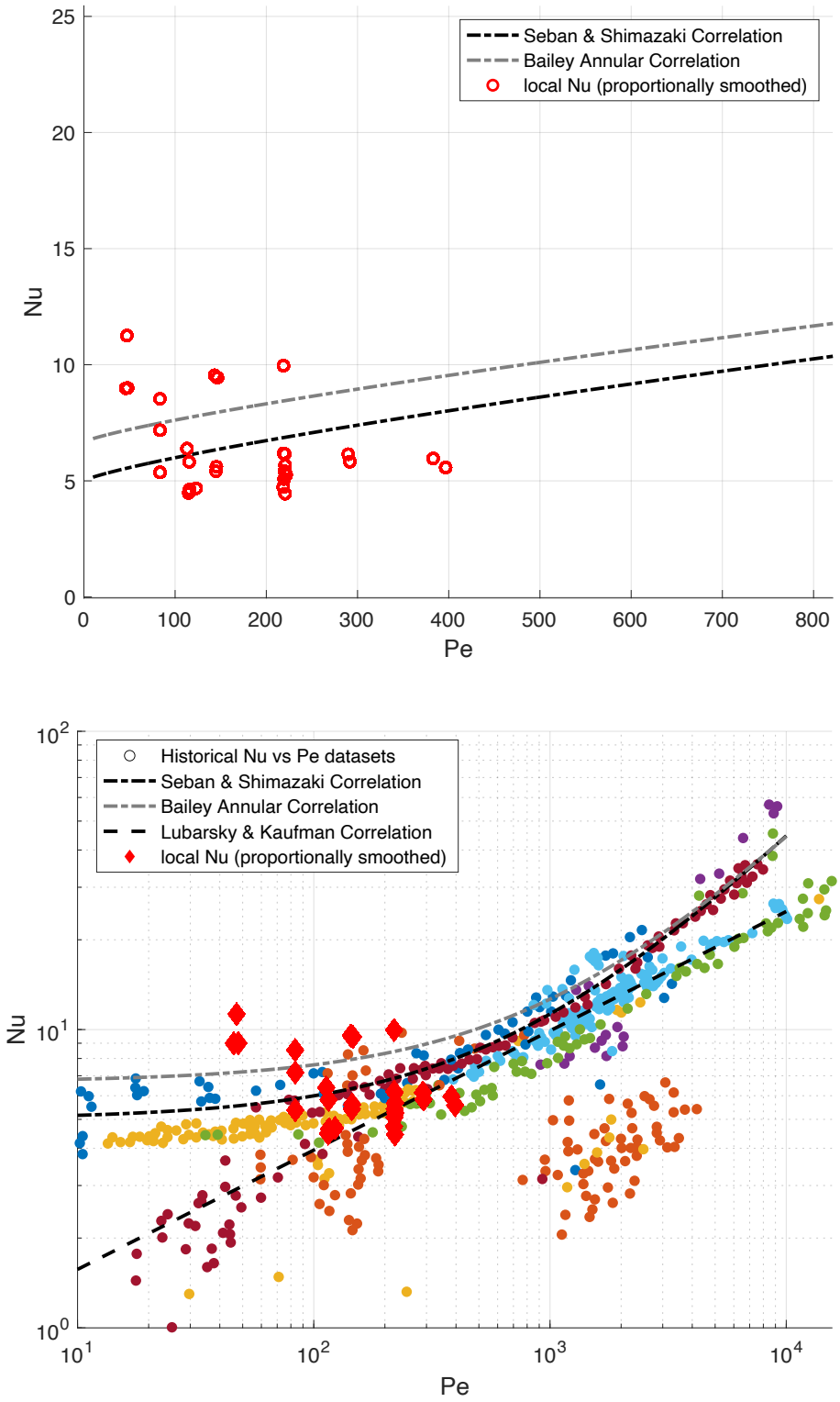

Figure 6-8: Nusselt number measurements using heat flux-ΔT proportional curve fit wire wrap FOTS data. Compared to correlations on a linear plot (top) and compared to historical data sets on a log-log plot (bottom) [36].

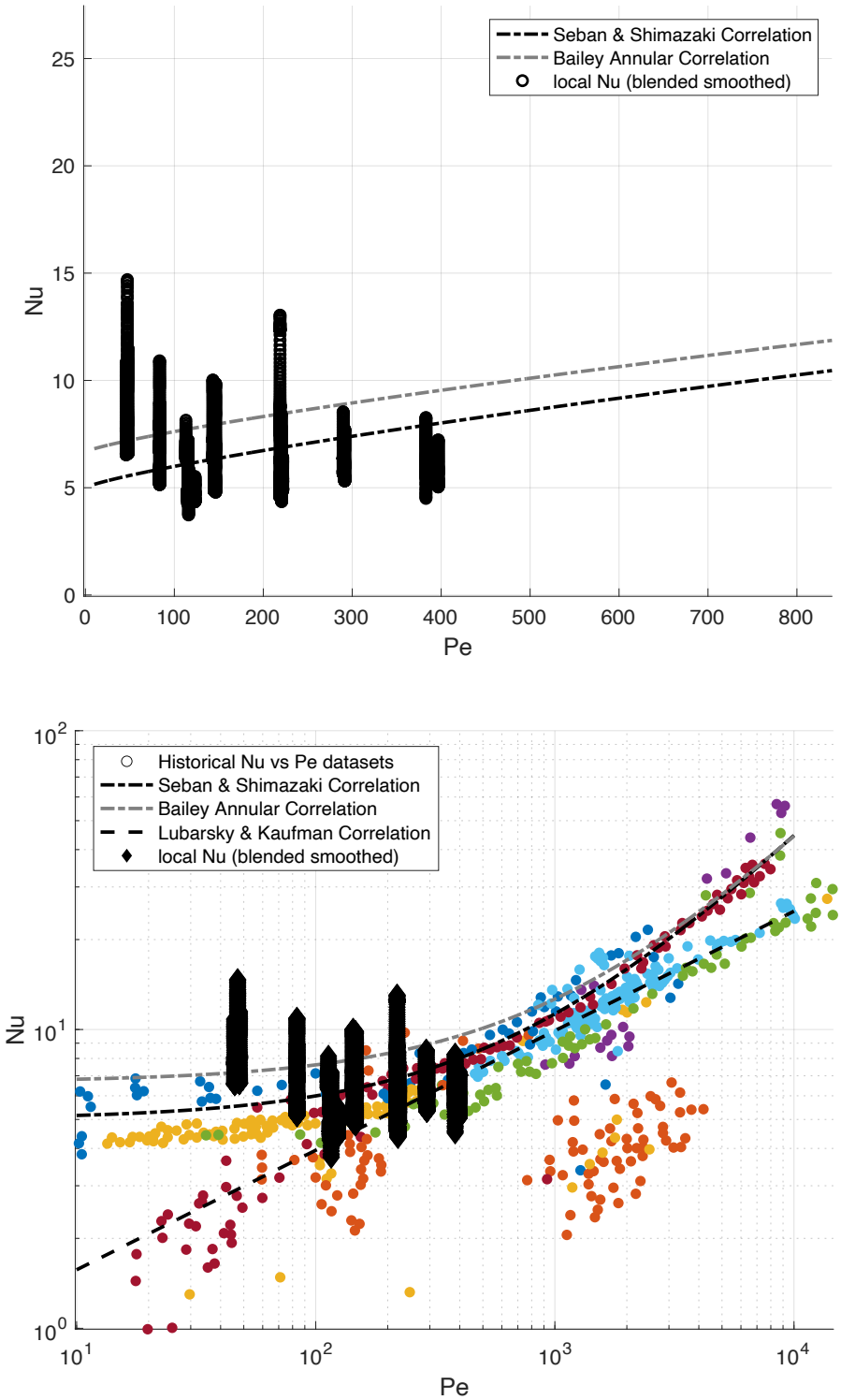

Figure 6-9: Nusselt number measurements using a blend of the heat flux-ΔT proportional curve fit wire wrap FOTS data with the raw wire wrap FOTS data. Compared to correlations on a linear plot (top) and compared to historical data sets on a log-log plot (bottom) [36].

For the curve fitting method that forces a constant Nu, it is observed that the "local" Nusselt numbers all have the same value within each test case as expected.

Similarly, spatial averaging over the test section can be used to characterize overall heat transfer, and this method offers the advantage of making uncertainty analysis straightforward, avoiding the application of spatial moving averaging to the raw temperature data curve. Nusselt numbers are calculated again from the raw temperature data according to equation 6-1 & 6-2, under the same assumptions. The resulting Nusselt numbers are then averaged over the fully developed portion of the heated length to obtain representative values for each test condition.

An accompanying error propagation analysis is performed to place 95% confidence interval limits on the measured average Nusselt number values (includes instrumentation calibration uncertainties, power measurement and power profile uncertainties, geometry, etc.) using the standard partial derivative error propagation methods. The average Nusselt numbers for 28 of the 36 total test cases are shown in linear and log-log plots and compared to the historical liquid metal heat transfer data in figure 6-10. Several of the low power/low heat flux test cases were excluded from this analysis as the heat fluxes were not large enough to generate significant measurable wall-to-bulk temperature differences in the sodium, resulting in large relative uncertainties in excess of 100% of the calculated average Nu value.

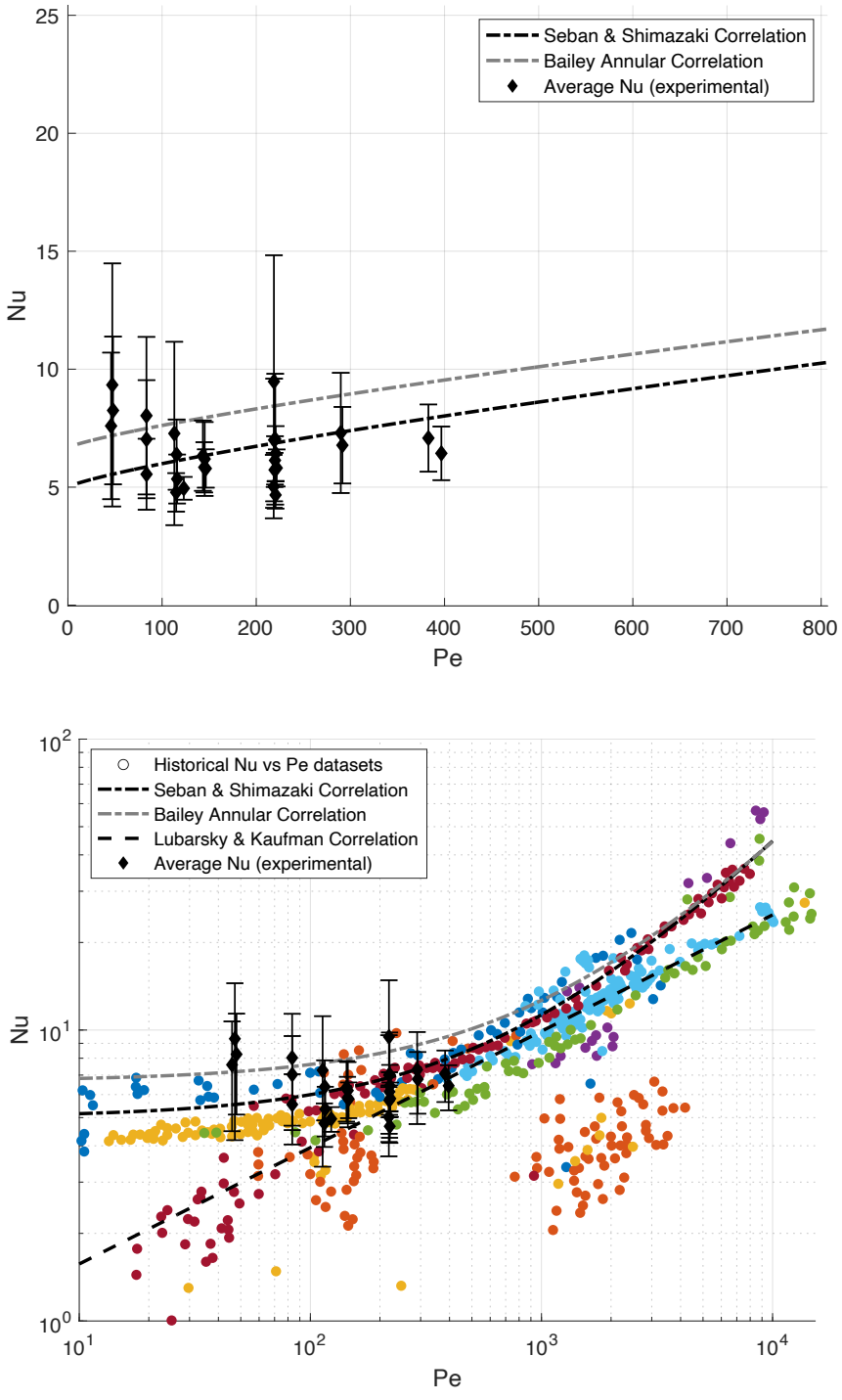

Figure 6-10: Average Nusselt number measurements with 2σ uncertainties. Compared to correlations on a linear plot (top) and compared to historical data sets on a log-log scale plot (bottom) [36].

This analysis approach preserves the experimentally measured temperature information while reducing sensitivity to small-scale variations arising from heater construction tolerances, allowing the overall heat transfer behavior of the sodium flow to be evaluated.

6.5 - Summary and Conclusions

While the fiber optic temperature sensor technique was found to provide reliable measurements of the local temperature field, analysis of the measured temperature profiles revealed variations along the wire wrap path. Investigation of these features through finite element modeling and scoping calculations indicates that they are consistent with the combined effects of heater filament eccentricity, positional variation of the wire wrap FOTS probe, and spatially varying thermal contact resistances within the heater assembly. Because convective resistance at the rod surface is comparatively small in liquid sodium, these internal conduction variations can significantly influence the local surface heat flux distribution. As a result, spatial averaging of the temperature data was employed to obtain representative heat transfer metrics for the system.

The experimental results lead to several key conclusions regarding both the overall heat transfer behavior and the measurement technique. When the temperature data are appropriately averaged, the resulting Nusselt numbers show good agreement with established liquid metal heat transfer correlations from Seban & Shimazaki and Bailey (annular) (figure 6-8) [27], [39], [42], [69]. This agreement suggests that these classical correlations remain applicable for this geometry more representative of SFR core configurations, which includes a wire wrap and cosine-shaped axial heat flux profile. This result also supports the conclusions of researchers like Mochizuki and Takano, who have reexamined some of the anomalously low Nu heat transfer

data from low Pe liquid sodium flows. These authors have suggested that such discrepancies are likely attributable to systematic errors, including instrumentation setup limitations in early liquid metal heat transfer experiments and improper accounting of heat transfer occurring in reactor plena regions (e.g. Monju and Joyo) [36], [40], [41].

The successful application of FOTSs in the wire wrap geometry in the present experiment also demonstrates the potential of this instrumentation technique for larger bundle scale experiments. Because the sensors can be integrated within a hollow wire wrap tube without disturbing the surrounding flow, the method provides an attractive way for obtaining temperature measurements in full SFR fuel assembly geometries. Such measurements could provide valuable validation data for thermal hydraulics models of wire wrapped pin bundles and improve understanding of local heat transfer behavior in SFR cores.

The results also provide insight into temperature variations that may occur in real SFR fuel assemblies. In operating metallic fuel elements, factors such as sodium bonding conditions, fuel-cladding interactions as burnup increases, and other geometry/contact changes at the bundle scale can produce circumferential variations in thermal resistance and therefore surface temperature too. These surface temperature variations have been reported to be on the order of tens of degrees Celsius, not unlike the variations observed on the surface of the simulated SFR rod in this work [17], [14], [15]. Again, this behavior is consistent with the characteristics of liquid metal cooling where the external convective resistance is small. The present measurements therefore provide a useful experimental analogue for understanding how geometric and contact condition variability can influence local thermal behavior in sodium fast reactor fuel pins.

A presentation of this experimental heat transfer data and the resulting overall heat transfer analysis are the primary focus of a 2026 manuscript submitted for publication in the Journal of Nuclear Engineering and Design, titled “High-Resolution Measurements of Liquid Sodium Heat Transfer on a Wire Wrapped Rod with a Prototypic Fuel Pin Heat Flux Profile” [70].

The finite element analyses presented in the work in this chapter were intended primarily as scoping calculations to aid interpretation of the experimental observations rather than as a comprehensive modeling study. Nevertheless, the results highlight opportunities for future comparison with higher fidelity computational models, and this is the subject of chapter 7.

Chapter 7 – CFD Model Development and Results Comparison

7.1 - Introduction

Accurate prediction of heat transfer behavior in SFR systems is essential for thermal hydraulic design and safety analysis, and the experimental efforts to analyze this behavior and to develop high-resolution sensors that can probe local temperature fields have been discussed throughout the previous chapters. The unique effects present in liquid metal systems, where the high required heat fluxes and low convective resistance at the surface makes the temperature field sensitive to small geometric and material variations in the solid components, were also introduced particularly in chapter 6. Consequently, even with high-resolution temperature measurements, interpretation of the measured data is not always straightforward, as the recorded temperatures may reflect local surface conditions including circumferential and axial variation due to solid conduction effects.

The temperature measurements obtained in the experimental work provide detailed insight into the thermal behavior of liquid sodium flowing around a wire wrapped fuel rod simulator. While these results were used to perform a heat transfer analysis that supported extending the historical correlations, particularly Seban & Shimazaki (1951) and Bailey (1950) (for thick annular channels), to the conditions that include wire wrapped pins with cosine-shaped axial heat flux profiles, the dataset also revealed characteristic features in the measured temperature fields, including axial and azimuthal temperature variations along the wire wrap and measurable radial temperature gradients within the coolant [27], [36], [38], [39], [40], [41].

Interpretation of these measurements requires consideration of the complex conjugate heat transfer processes occurring within the system. Computational fluid dynamics (CFD) modeling provides a useful complementary tool for examining these phenomena. When properly

validated against experimental data, CFD simulations can provide detailed spatial information on the temperature and velocity fields that are not directly accessible through instrumentation. In particular, numerical models can help clarify how the temperature measured within the hollow wire wrap relates to the actual surface temperature of the rod and to the surrounding solid and fluid temperature fields. CFD models are also useful for validation of radial temperature profiles measured in the liquid sodium flow, among other useful comparisons to experiment.

The objective of chapter 7 is therefore to compare the high-resolution measurements obtained from the sodium heat transfer experiment with results from a detailed full-scale CFD model of the experimental test section developed using Simcenter STAR-CCM+ [71]. This model was developed by Hugo Barthod and Guillaume Mignot, at Oregon State University, and is the subject of "CFD assessment of the uncertainty of temperature measurements with fiber optics (DTS) in Sodium Fast Reactors (SFR)" (2026) [72]. Rather than focusing on CFD methodology itself, the goal here is to evaluate how well the numerical model reproduces the experimentally observed thermal behavior and to use the simulations to better interpret the experimental temperature measurements. In addition, this work contributes to ongoing efforts to assess and validate modeling approaches used in thermal hydraulic analysis and design of SFR systems.

The comparisons presented include axial temperature distributions along the wire wrap, radial temperature profiles within the sodium flow, bulk fluid temperature estimations, evaluation of the relationship between the measured wire wrap temperatures and the underlying rod surface temperature, and comparisons of predicted/measured heat transfer behavior/Nusselt numbers. Together, these results provide a basis for interpreting high-resolution temperature

measurements in wire wrapped geometries and for assessing the applicability of CFD modeling approaches for representing heat transfer behavior under SFR-relevant conditions.

The research discussed in this chapter resulted in a manuscript submitted for publication in the Journal of Nuclear Engineering and Design, titled “Comparison of High-Resolution Liquid Sodium Heat Transfer Measurements with CFD Modeling of a Wire Wrapped Fuel Rod Simulator” [73] (2026).

7.2 - Computational Modeling Literature Review

Computational investigations using CFD methods including RANS, LES, and DNS have been used to study flow and heat transfer in wire wrapped pin geometries relevant to SFRs, in addition to the experimental studies and other work that is the subject of chapter 2 [20], [44], [45], [46], [47]. However, robust, high-resolution experimental data suitable for validating such models remains limited, particularly for sodium flows in the low to moderate Peclet number regime.

High-fidelity simulations, including Large Eddy Simulation (LES), have been used to resolve detailed flow structures around individual wire wrapped pins. For example, Peet and Fischer (2010) conducted LES of flow around a single wire wrapped pin and demonstrated the formation of complex vortex structures on the leeward side of the wire wrap [20]. Their results highlighted the strong coupling between local flow features and surface temperature, emphasizing that accurate knowledge of the surface temperature distribution is important for evaluating heat transfer behavior in these systems.

More recently, even higher-fidelity approaches such as Direct Numerical Simulation (DNS) have been applied to small bundle configurations. For example, Dutra et al. performed a

DNS study of a 7-pin wire wrapped bundle and predicted Nusselt numbers in the range of 8–10 for flow at a Peclet number of 50. This work also demonstrated the role of wire wraps in enhancing heat transfer when the bundle is considered as a whole [74]. At the same time, more computationally efficient Reynolds-Averaged Navier–Stokes (RANS) approaches remain widely used for larger scale systems. Studies such as Jeong et al. have shown that RANS models using shear stress transport (SST) turbulence closures can capture key features of the flow and predict increased heat transfer effectiveness due to the presence of wire wraps [46]. While these studies provide valuable insight into the underlying physics, direct comparison with high-resolution experimental data in highly instrumented prototypic geometries (bundle of single wrapped pins) remains limited [75].

7.3 - CFD Model Description

A CFD model of the experimental test section was developed using Simcenter STAR-CCM+ to simulate the coupled thermal and fluid behavior of liquid sodium flowing past the wire-wrapped fuel rod simulator [71]. The base model was created at Oregon State University as part of a collaborative effort and is described in detail in “CFD assessment of the uncertainty of temperature measurements with fiber optics (DTS) in Sodium Fast Reactors (SFR),” by Barthod and Mignot (2026) [72]. Only a brief overview of the model is provided here, with emphasis on the aspects relevant to comparison with the experimental measurements. The purpose of the present work is not to develop new CFD methodology, but rather to evaluate whether established methods reproduce experimentally observed behavior and to use the simulation results to aid in interpretation of the experimentally measured temperature fields.

The modeled domain consists of the vertical test section containing the fuel rod simulator and surrounding annular sodium flow region. The geometry includes the rod cladding, the helically wrapped hollow capillary tube representing the wire wrap, the internal region of the wire wrap capillary, and the annular fluid region occupied by the sodium coolant (see figure 7-1). The heating within the rod is represented by imposing a prescribed axial heat flux distribution along the inner surface of the cladding corresponding to the cosine-shaped profile used in the experiment. Experimental instrumentation, including thermocouples and fiber optic probes, are not explicitly modeled as physical bodies; instead, temperature data are extracted at corresponding locations within the computational domain.

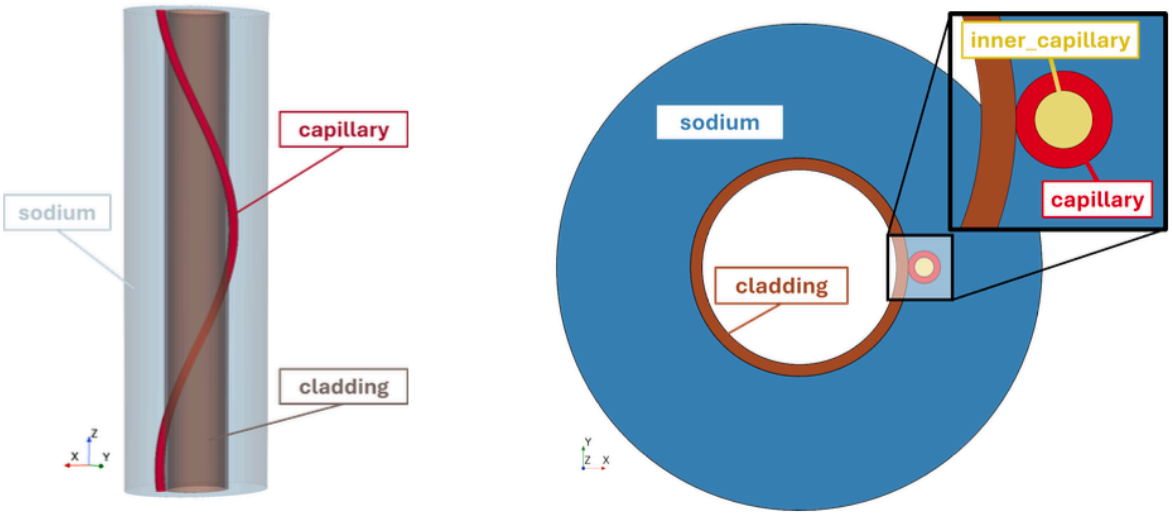

Figure 7-1: Experimental geometry modeled for simulation in CFD (Barthod and Mignot, 2026) [72].

The flow and heat transfer are modeled using steady-state RANS equations with conjugate heat transfer between the solid and fluid regions. Turbulence is represented using the SST k–ω model, which blends near-wall and free-stream formulations to provide accurate resolution of both boundary layer and bulk flow behavior. Temperature-dependent material properties are used for the sodium and structural materials. The computational mesh is generated

using a directed meshing approach that exploits the predominantly axial nature of the geometry, allowing efficient resolution of the thin gap between the rod and wire wrap while maintaining tractable computational cost. Additional details regarding mesh generation, mesh independence of results, turbulence modeling, and numerical uncertainty can be found in Barthod and Mignot (2026) [72]. The mesh cells in the computational domain are shown in figure 7-2.

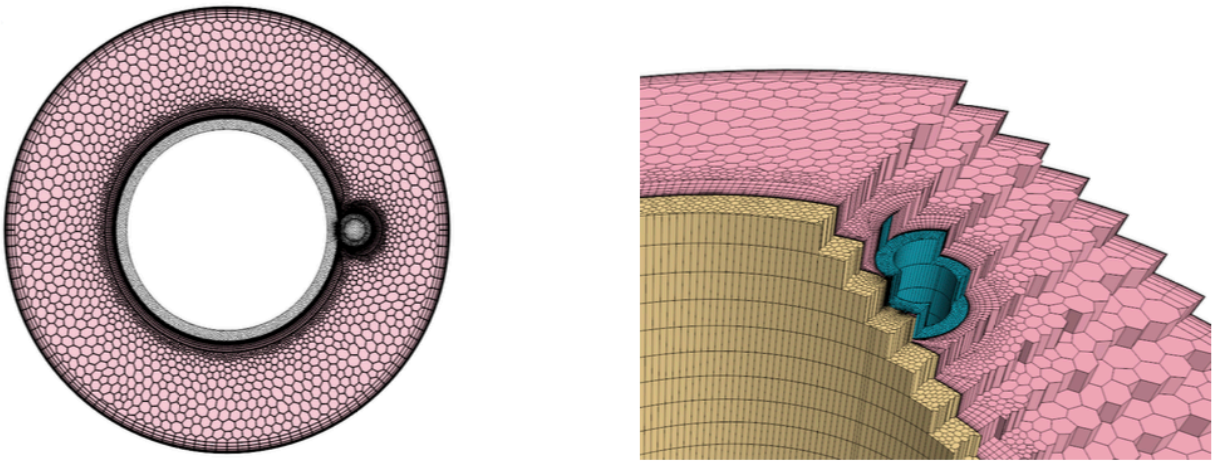

Figure 7-2: Mesh visualization (Barthod and Mignot, 2026) [72].

To account for the influence of the inlet geometry on the developing flow field, a separate CFD model including the test section inlet tee and upstream piping was developed. This auxiliary simulation was used to generate physically realistic velocity and turbulence profiles at the entrance to the vertical test section, capturing the non-uniform flow distribution and secondary flow structures introduced by the inlet configuration. The resulting profiles were then applied as boundary conditions for the primary computational domain containing the heated wire wrapped rod, ensuring that the inlet conditions used in the simulations are representative of the experimental configuration and support meaningful comparison between measured and predicted temperature fields.

For comparison with the experimental measurements, temperatures were extracted from the CFD solution at locations corresponding to the wire wrap fiber optic sensor (including over a range of positions in the housing tube), the embedded sensors within the rod, and the transverse fiber positions in the sodium flow. In addition, surface temperatures along the rod and spatial temperature fields within the sodium were evaluated to aid interpretation of the measured data. The temperature results and implications of Barthod and Mignot's work are discussed in detail in "CFD assessment of the uncertainty of temperature measurements with fiber optics (DTS) in Sodium Fast Reactors (SFR) [72]."

7.4 - Comparison of Experimental and CFD Results

The CFD model results are compared directly with the high-resolution temperature measurements obtained in the liquid sodium heat transfer experiments. These comparisons are used to evaluate the extent to which the numerical model reproduces the key thermal features observed in the experimental data, including the temperature distribution along the wire wrap, radial temperature profiles within the sodium flow, and local temperature variations associated with the wire wrap geometry. Emphasis is placed on comparisons that provide insight into both the overall heat transfer behavior and the interpretation of the measured temperature data.

7.4.1 Wire Wrap Sensor Position and Measurement Variability

To examine the interpretation of the wire wrap FOTS data, the effect of positional variation of the FOTS within the hollow wire wrap capillary was first investigated, as was done with finite-element solid conduction modeling in chapter 6 (see figures 6-2 & 6- 3). The CFD

model of Barthod and Mignot produced similar results, demonstrating that the sensor location within the capillary can have an important effect on the temperature that is measured.

Figure 7-3 shows the predicted wire wrap temperature traces corresponding to five representative sensor positions spanning the feasible range of motion within the capillary for representative example test case HT3TC06 (also focused on in section 5.2); one of eight heat transfer test conditions simulated in CFD. These positions include the radially innermost and outermost locations, as well as the bounding azimuthal positions, and a central location within the tube. The eight selected test cases, shown in table 7-1, span flow and power conditions representative of the experimental matrix.

Table 7-1: Test matrix containing the eight modeled HT(3) series test cases.

Test Case	T_{in} [°C]	T_{out} [°C]	$\dot{m}$ [kg/s]	Pe [-]	$\dot{q}$ [kW]
01	360	398	0.53	383	25.7
02	360	426	0.30	221	25.7
03	360	393	0.30	219	12.9
04	360	453	0.12	83	13.9
05	361	405	0.12	85	7.0
06	201	298	0.18	116	21.5
07	199	247	0.18	114	10.9
08	299	452	0.07	47	13.2

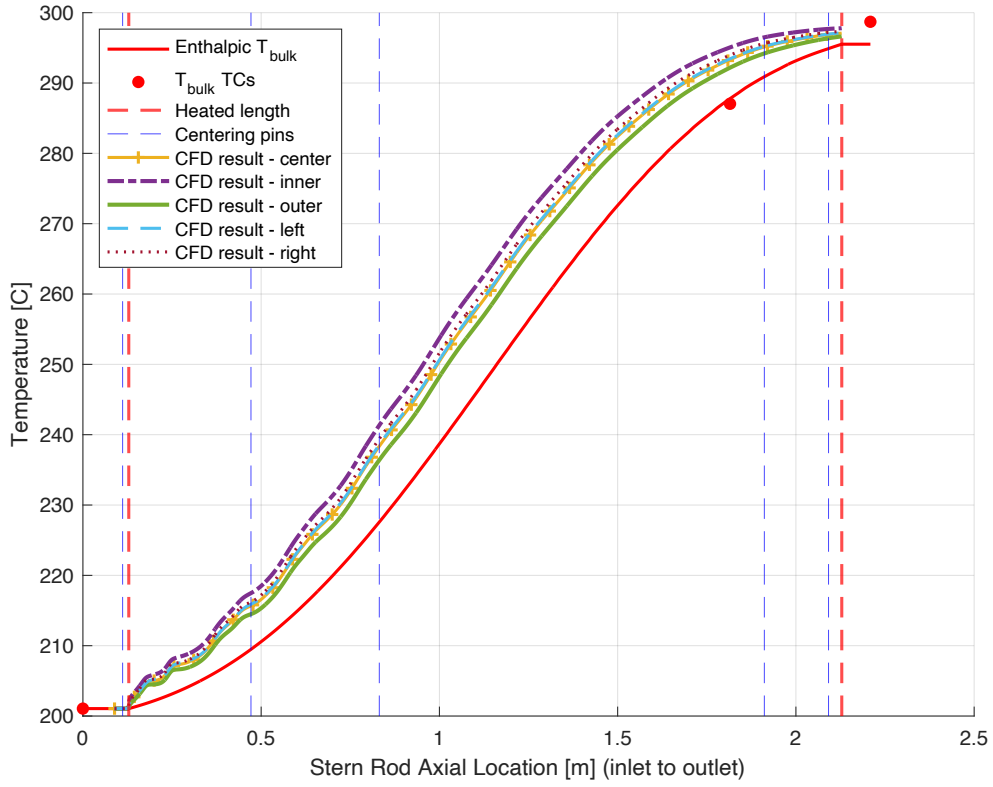

Figure 7-3: CFD wire wrap FOTS temperature trace results for four bounding sensor locations for HT(3) Test Case 06 conditions.

Several notable features are observed in figure 7-3. The predicted temperature varies appreciably depending on the sensor position, with differences on the order of 5-6 °C for this case (deviating by up to 20% of the estimated surface-to-bulk temperature difference). The largest variation occurs between the radially innermost and outermost positions, while azimuthal variation is comparatively smaller. These magnitudes are consistent with both the experimental observations and the finite-element conduction models presented in chapter 6. Additional sensitivity studies indicated that the thermal properties of the wire wrap fill region (e.g., air, helium, or solid filler) have a negligible effect on the measured temperature relative to positional variability.

Recall that in the experiment, the sensor position is expected to vary along the wire wrap due to thermal expansion of the test section components and mechanical compliance of the hardened 316 stainless FOTS capillary. The CFD results therefore also support the interpretation that the observed temperature fluctuations arise from positional variability combined with solid conduction effects within the rod.

These observations motivate averaging of the wire wrap temperature over the range of possible sensor positions when comparing to additional CFD model results and experimentally measured data. Accordingly, the average of the five CFD-predicted temperature traces is used to represent the effective wire wrap measurement for subsequent comparisons.

7.4.2 Relationship Between Wire Wrap FOTS Temperature and Surface Temperature

Barthod and Mignot's CFD model was further used to examine how the wire wrap FOTS measurement relates to the local surface temperature field on the fuel simulator. Circumferentially averaged surface temperatures were obtained by performing a length-weighted average of the cladding and wire wrap surface temperatures around the wetted perimeter at each axial location. These values are then compared to the averaged wire wrap FOTS temperature obtained from the CFD traces for each bounding sensor location (see figure 7-4).

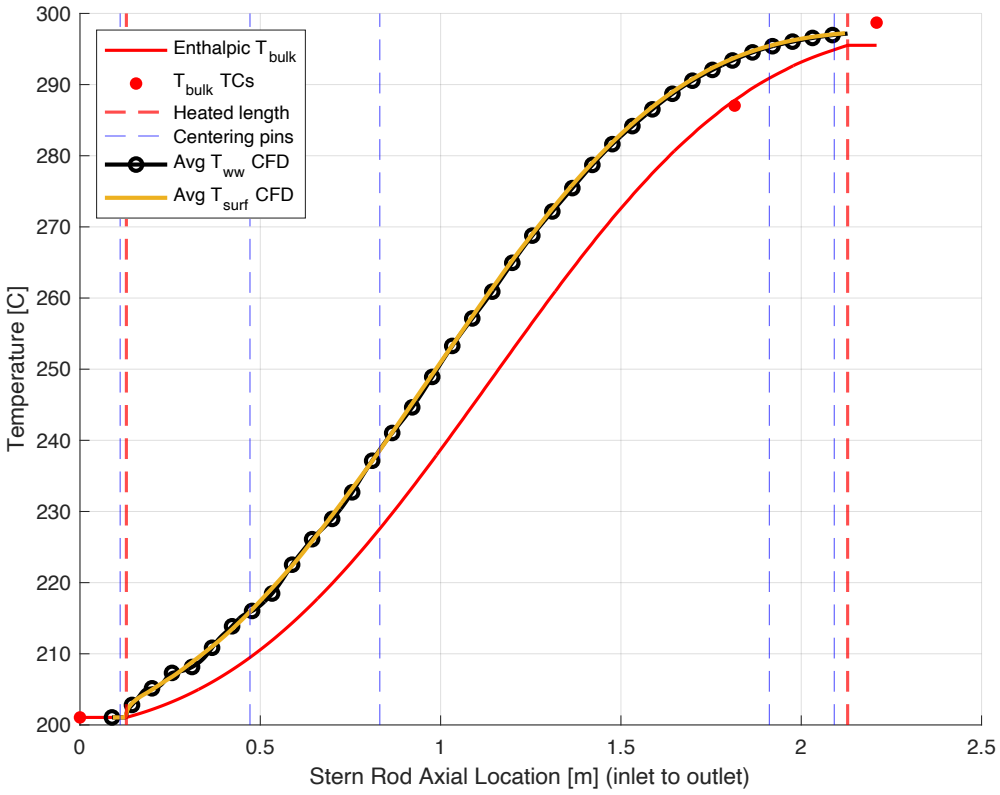

Figure 7-4: CFD-modeled local circumferential average surface temperature compared to average simulated wire wrap sensor temperature profile for HT(3) Test Case 06 conditions.

The averaged wire wrap temperature closely matches the circumferentially averaged surface temperature along the axial length. For the example test case, agreement is within ~0.75 °C, or 5% of the surface-to-bulk temperature difference, across the domain, with similar trends observed across all modeled cases.

This result supports the interpretation that the wire wrap FOTS provides temperature measurements that, on average, are representative of the local average fuel simulator surface temperature in the SHTL facility. This assumption underpins the overall heat transfer analysis presented in section 6.4 and is reinforced by the present CFD comparison.

7.4.3 Comparison with Experimental Wire Wrap FOTS Data

The experimental wire wrap temperature data from example test case HT3TC06 (originally presented in figure 5-2) are also compared directly with the CFD predictions in figure 7-5. Both the raw and spatially smoothed experimental data are shown, where smoothing is performed using a moving average window corresponding to one wire wrap pitch length (18 cm) [70].

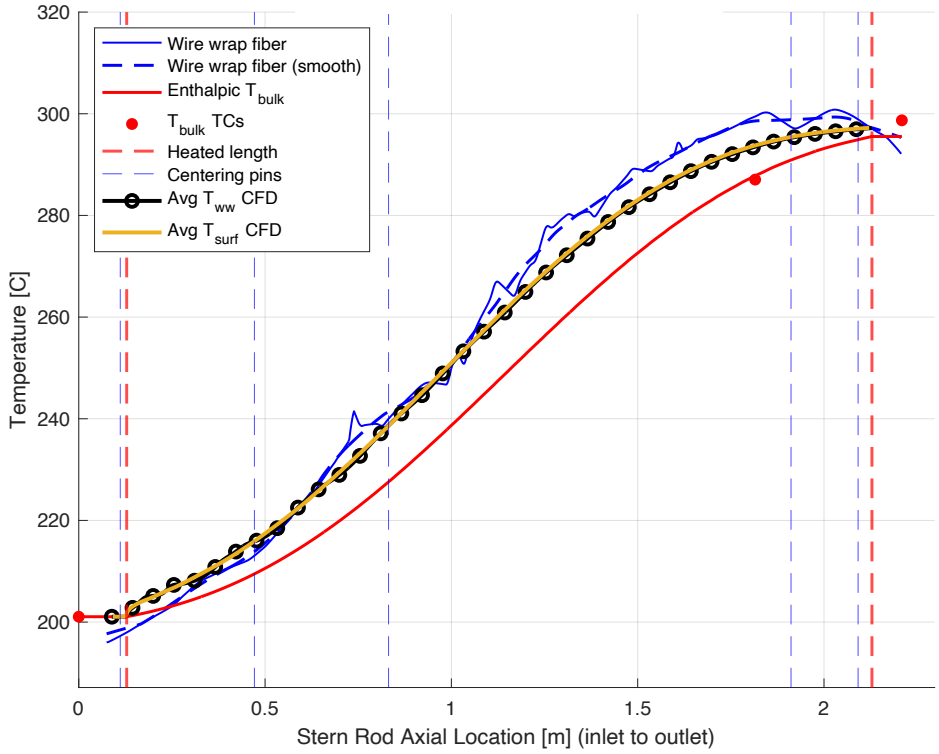

Figure 7-5: CFD-modeled circumferential average surface temperature and average wire wrap FOTS trace compared to raw and smoothed wire wrap data for example HT(3) Test Case 06.

While local fluctuations are evident in the raw experimental data and have been discussed at length above, the overall trends show good agreement with the CFD-predicted circumferentially averaged surface temperature/average wire wrap temperature. The smoothed experimental data deviated from the average modeled trace values by up to ~ 50% of the predicted surface-to-bulk temperature difference over the central developed-flow portion of the

test section for the example test case, indicating that spatial averaging captures the general trend of the underlying heat transfer behavior.

Once again, the general agreement of the predicted average surface temperature along the rod and the experimental wire wrap sensor temperature measurements further reinforces the assumption that the wire wrap sensor can be used as an analog for average surface temperature, especially when smoothing or averaging techniques are applied to the data in order to analyze the overall heat transfer behavior of the sodium flow.

7.4.4 Conjugate Heat Transfer Effects (2D cross-section map)

Additional insight into the influence of wire wrap geometry is provided by cross-sectional 2D temperature fields obtained from the CFD simulations. As shown in figure 7-6, a hot spot is observed in the cladding region beneath the wire wrap. This behavior is consistent with the additional thermal resistance introduced by the wire wrap, which partially impedes convective heat transfer at the rod surface. These results highlight the conjugate nature of the heat transfer problem, where local variations in solid conduction paths influence the surface temperature distribution and, consequently, the measured temperature within the wire wrap.

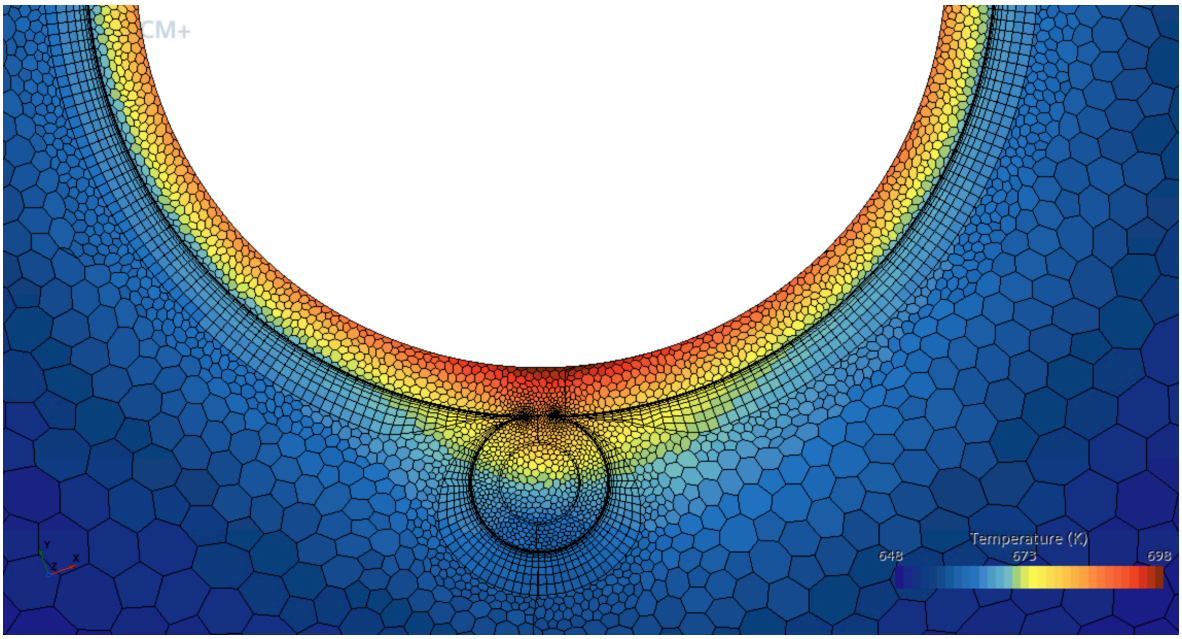

Figure 7-6: 2D temperature map from CFD simulation.

The 2D temperature map shown in figure 7-6 also illustrates how the wire wrap FOTS, at its average location within the capillary, effectively measures a circumferentially averaged surface temperature. The localized hot spot beneath the wire wrap conducts heat into the surrounding structure and into the wire wrap itself, elevating the temperature within the capillary region. As a result, the sensor captures a temperature consistent with a circumferentially averaged surface value.

7.4.5 Nusselt Number Comparison

The overall heat transfer behavior predicted by the CFD model was also evaluated by calculating local and average Nusselt numbers. The bulk sodium temperature T_{bulk} was obtained from a mass flow weighted average of the sodium temperature field result, and local heat transfer coefficients and Nusselt numbers were calculated using Newton's law of cooling (equations 7-1 & 7-2) with the circumferentially averaged surface temperature T_{surf} and prescribed local heat flux $\dot{q}''$.

$$h = \frac{\dot{q}''}{T_{surf} - T_{bulk}} \qquad (7-1)$$

$$Nu = \frac{hD_e}{k_f} \qquad (7-2)$$

D_e is the hydraulic diameter of the annular flow channel and k_f is the thermal conductivity of liquid sodium.

The resulting Nusselt numbers were averaged over the heated length and compared to experimental results and established correlations. As shown in figure 7-7, the CFD predictions are in good agreement with both the experimental data and classical correlations discussed in chapter 6, further supporting that the Barthod and Mignot's model captures the dominant heat transfer behavior in the system.

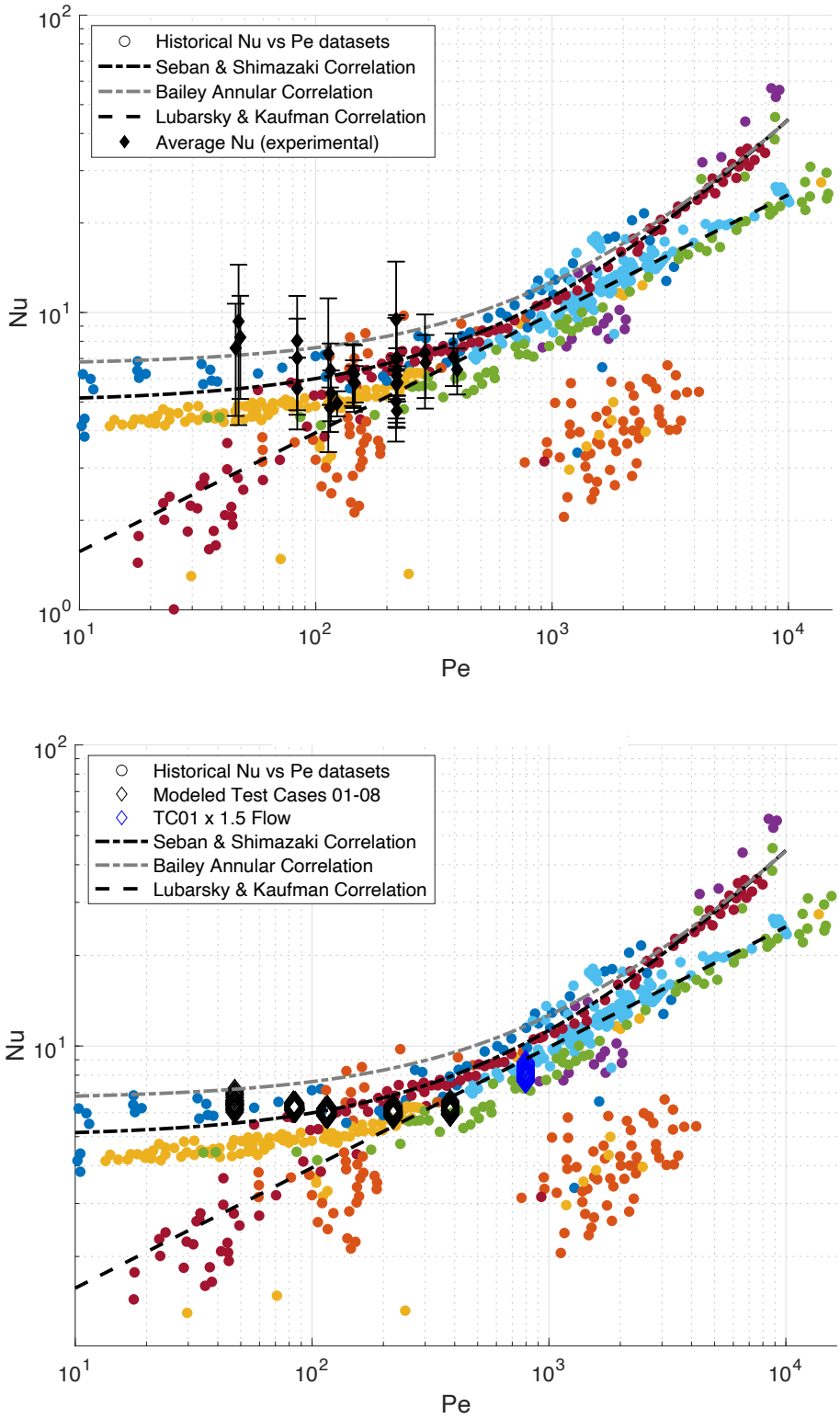

Figure 7-7: Average Nusselt number from experimental overall heat transfer analysis (top) and local Nusselt numbers from CFD-simulated results (bottom) compared to historical data and correlations [36].

The agreement between the modeled heat transfer and the same historical correlations examined and found to agree with the experimental data can also be seen by overlaying the surface temperatures predicted by the Seban & Shimazaki (1951) and Bailey (1950) correlations with the surface temperature predictions and measurements in figure 7-8 [27], [39], [42], [69].

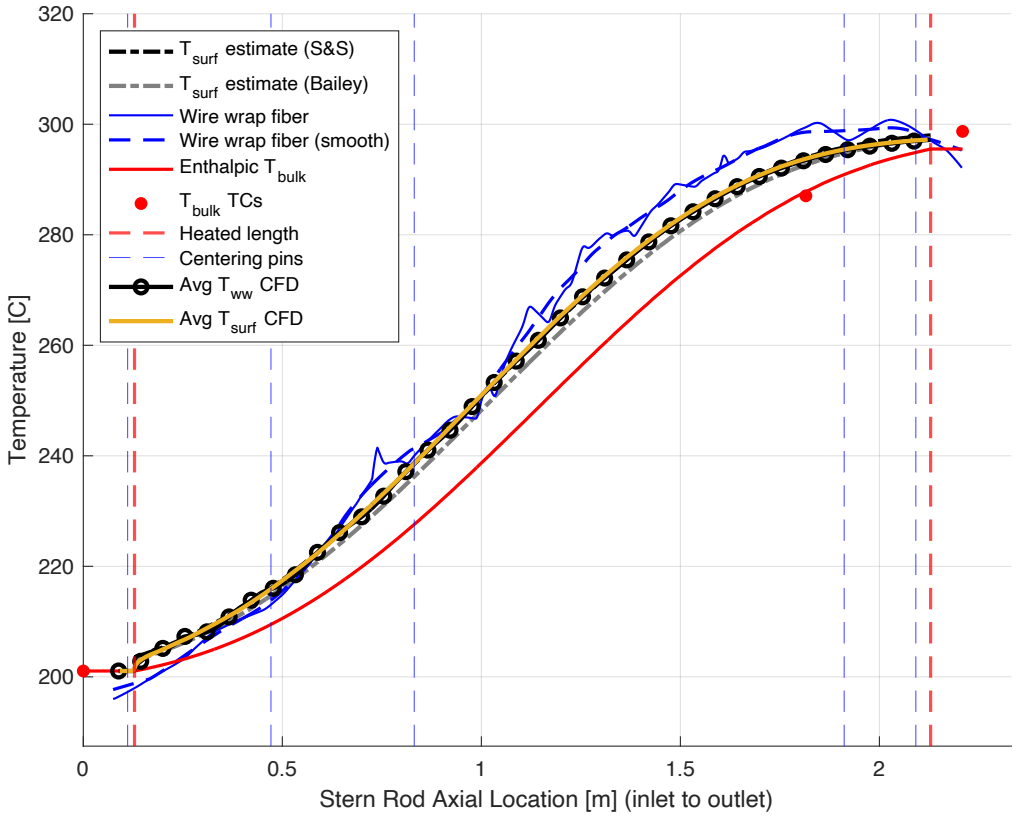

Figure 7-8: Plot of experimental and modeled temperatures overlayed with correlation-predicted surface temperature for example HT(3) Test Case 06.

7.4.6 Radial Sodium Temperature Profiles

Radial temperature profiles measured using the transverse FOTS cutting through the sodium flow channel at three different axial height locations were also compared with CFD predictions. As shown in figure 7-9, the model reproduces much of the same measured radial

temperature gradient behavior seen throughout the annular sodium flow, including the persistence of temperature change across the annular gap.

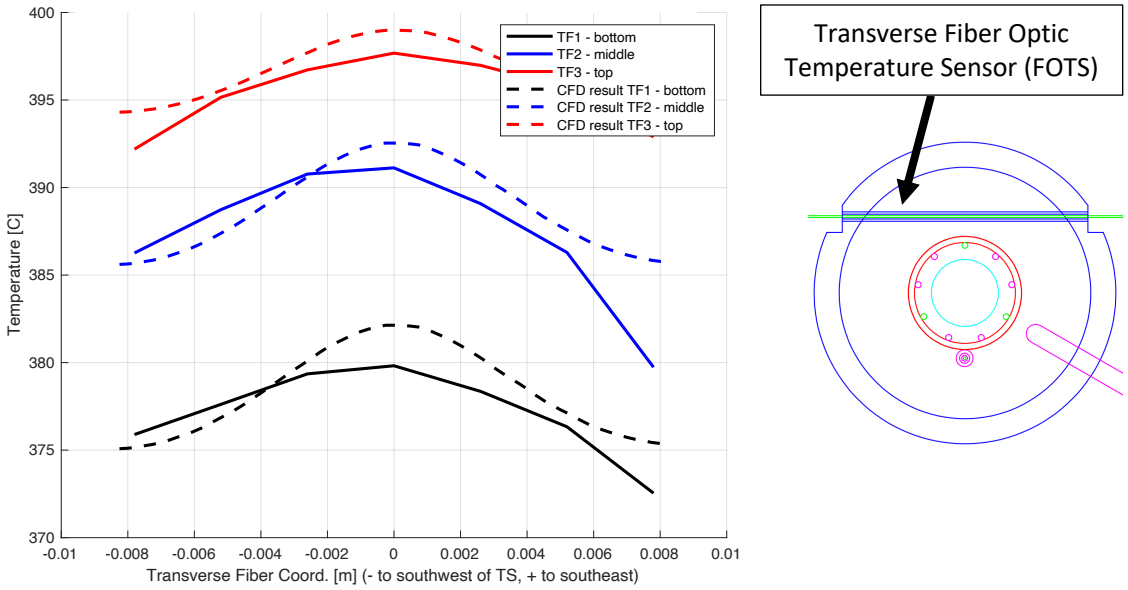

Figure 7-9: Example HT(3) Test Case 01 sodium channel transverse FOTS measurements from experiment (solid) compared to CFD results (dashed).

This behavior is consistent with the relatively high thermal conductivity of liquid sodium, where diffusive transport contributes significantly to heat transfer, even outside the immediate near-wall region. Differences in the experimentally measured and CFD predicted profiles are attributed to uncertainty in the precise centering and alignment of the transverse FOTS inside its test section capillary tubes, due to the 2.6 mm gauge spacing of the fiber sensor (meaning there are seven measurement locations per span of the sensor), in addition to the presence of the sensor's capillary tube housing in the experiment.

7.4.7 Axial Conduction Discussion

The CFD results also provide insight into axial heat transport within the sodium flow. Under certain conditions, axial conduction within the fluid may contribute to the temperature

distribution, particularly in low flow regimes. These effects are difficult to isolate experimentally but are captured in the CFD simulations, providing additional context for interpreting the measured temperature fields.

To examine the importance of axial conduction, bulk sodium temperature profiles obtained from the CFD simulations were compared with temperatures calculated from an incremental energy balance using the prescribed and measured experimental heat input. In the CFD results, bulk temperature was defined using a mass-flow-weighted average across the annular flow channel at each axial location. See figure 7-10 for this comparison for the example test case.

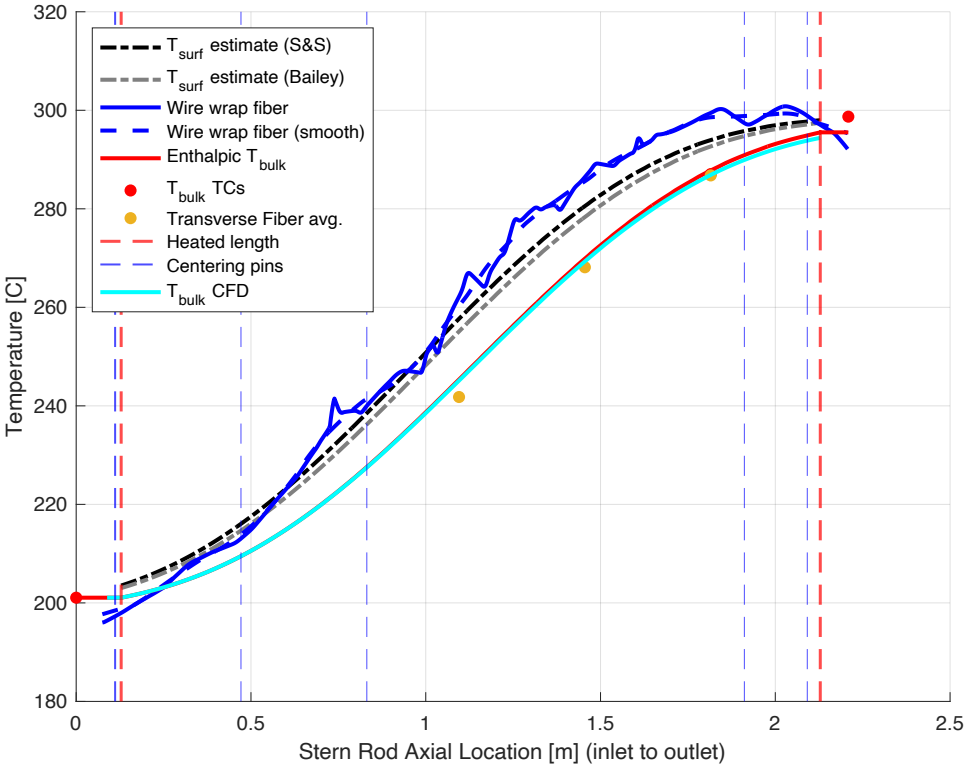

Figure 7-10: Axial temperature data and predictions with comparison of bulk sodium temperature estimate from an incremental energy balance and from CFD mass flow weighted average, for HT(3) Test Case 06 conditions.

Figure 7-10 shows that the two bulk temperature traces are in close agreement over most of the heated length, which is true for the majority of modeled test cases. This indicates that axial back-conduction within the sodium is generally small under the test conditions studied. Noticeable deviations are observed only for the lowest-flow cases, where the CFD-predicted bulk temperature differs from the energy-balance result by up to approximately 2-4 °C. These results suggest that axial conduction in the fluid is not a dominant effect for most of the present experiments, but it can become non-negligible as Peclet number decreases even further or if the heat flux input gradient was altered. This comparison also provides additional confidence that the bulk temperature derived from an incremental energy balance going up the test section used in the experimental heat transfer analysis in the preceding chapters is representative of the actual fluid's thermal state in the test section.

7.5 - Summary and Conclusions

The comparisons between experimental results and different CFD model predictions collectively demonstrate that the CFD modeling method captures the key thermal behaviors observed in the experiment, including temperature variations along the wire wrap FOTS location, the influence of geometric and conduction effects, the same overall heat transfer behavior (average Nusselt numbers), and radial gradients in the sodium flow. In addition, the simulations provide insight into transport mechanisms such as axial conduction that are difficult to isolate experimentally. Together, these results support the use of the modeling approach for interpreting experimental measurements and predicting heat transfer behavior in similar liquid metal systems.

More broadly, the agreement between CFD predictions and high-resolution experimental measurements provides mutual support for both approaches. The experimental data support the use of the modeling techniques, turbulence closures, and numerical methods employed in Barthod and Mignot's CFD simulations for liquid sodium flows, while the CFD results reinforce key assumptions made in the interpretation of the experimental measurements. In particular, the simulations provide physical context for understanding how measured temperatures relate to the underlying thermal field, strengthening confidence in the experimental analysis methods.

The CFD simulations of the wire wrap sensor within the capillary demonstrate that positional variability of the fiber can produce temperature variations comparable to those observed experimentally. These results are consistent with independent two- and three-dimensional finite element solid conduction models of the heater rod and support the conclusion that the measured temperature fluctuations arise from a combination of geometric effects and internal conduction pathways. In this way, the modeling results provide confidence in a coherent physical explanation for features observed in the experimental data.

In addition, the CFD results support the interpretation that the temperature measured by the fiber optic sensor within the hollow wire wrap corresponds to a measure of the locally averaged rod surface temperature, within the context of the conjugate heat transfer environment and temperature field surrounding the wire wrap. This finding provides confidence in the use of the wire wrap FOTS as a meaningful proxy for surface temperature in this geometry and reinforces the methodology used to evaluate heat transfer behavior in the experimental study.

The CFD simulations also show good agreement with the experimental temperature measurements more generally, including both wire wrap temperature profiles along the helical path and radial temperature distributions in the sodium flow. In addition to the similar predicted

temperatures, local and average Nusselt number values calculated from CFD results also agree well with those calculated from experimental results alone. These agreements indicate that the modeling approach captures the dominant heat transfer mechanisms present in liquid metal flows around wire wrapped pins under the SFR-relevant conditions studied and supports the broader applicability of the approach for similar systems. The Nusselt numbers resulting from this CFD study also aligned with those predicted by other similar CFD studies discussed in the literature review. Particularly, a DNS simulation of a 7-pin wire wrapped rod bundle from Dutra et al. (2024) predicted Nusselt numbers of 8-10 for Pe = 50 for sodium flows around the central pin [74]. This compares well with the Nu = ~6.5-8 values measured with Barthod and Mignot's RANS CFD technique here, for a sodium flow of Pe = 47, especially considering Dutra et al.'s (2024) observed enhancement of heat transfer due to the presence of wire wraps when considering a *whole bundle configuration*.

Further validation is provided through comparison of radial temperature profiles within the sodium flow channel for a higher heat flux representative test case, where the CFD model reproduces the measured gradients and supports the interpretation of bulk and near-wall temperature behavior in low Prandtl number fluid turbulent flows. The simulations additionally provide insight into the role of axial conduction within the sodium, demonstrating that back-conduction is generally small for the conditions studied, but of course may become non-negligible at very low flow rates. This capability complements the experimental measurements by enabling assessment of transport mechanisms that are difficult to isolate experimentally.

Finally, these results demonstrate the value of combining high-resolution experimental measurements with detailed CFD modeling for understanding liquid sodium heat transfer. The validated modeling approach provides a useful tool for predicting thermal behavior in wire

wrapped fuel geometries relevant to sodium fast reactors, while the experimental data provide a benchmark for continued model development and validation. Together, these approaches contribute to improved accuracy and validity of thermal hydraulic analyses that support the design and evaluation of advanced nuclear reactors being developed for commercial deployment.

Chapter 8 – Friction Factor Analysis and Application to Pronghorn SC Code

8.1 - Idaho National Lab Modeling and Simulation Project

In addition to the powered heat transfer tests, isothermal validation of optical fiber instrumentation techniques, and CFD comparison work, the wire wrapped rod test section was also instrumented with a differential pressure transducer. This instrument was used to record pressure drop data throughout the various Sodium Heat Transfer Test Loop test campaigns, especially the isothermal validation runs. This dataset was used during a research project with Idaho National Laboratory (INL) scientists, where it was compared to other sodium friction factor treatments, including those used to model SFR core assembly fluid mechanics in system level codes. The work discussed in this chapter was done under a DOE-NE UNLP internship with funding support from the UNLP graduate fellowship award, and it resulted in a manuscript submitted publication in the Journal of Nuclear Engineering and Design titled “Experimental Friction Factor Measurements in Liquid Sodium Around a Wire Wrapped Pin and Application in Pronghorn SC Code” [76]. The journal article was authored with the help of two collaborators and research mentors at INL, Dr. Mauricio Tano Retamales and Dr. Piyush Sabharwall, in addition to Prof. Mark Anderson.

8.2 - Introduction

As discussed in chapter 1, many of the SFR designs presently of interest for new commercial nuclear power plants use similar core designs featuring hexagonal bundles of fuel rods, as employed in historical programs such as EBR-II/IFR and FFTR, and carried forward in proposed designs including GE-Hitachi PRISM, the ARC-100 from ARC clean technology, and

TerraPower and GE-Hitachi's Natrium design [9], [7], [10]. The helical wire wraps applied to each fuel rod's surface, serving a similar role as the spacer grids commonly used in LWRs, have been discussed at length in the previous chapters. In addition to the conjugate heat transfer questions and the nonintrusive instrumentation pathways provided by this geometry, understanding how wire wraps contribute to the pressure drop and friction factor of sodium flows around a wire wrapped fuel rod, or through a bundle fuel assembly, is an important research question, and experimental data of this nature can support SFR operations and validation of computational/numerical models.

Friction factor and general liquid metal flow behavior in wire wrapped rod bundles has been studied extensively through correlation development and numerical simulation, with the Cheng and Todreas correlation (1986) and its subsequent "Upgraded Cheng and Todreas" (UCTD) update (2018) providing the primary basis for subchannel code applications [77], [78], [79]. CFD studies of flow around single wire wrapped pins and in multi-pin bundle geometries have expanded understanding of local flow phenomena in these configurations, and many of these studies using DNS, LES, and RANS have been mentioned in chapter 7 [44], [80], [45], [74]. However, experimental data for these geometries in liquid sodium remains limited, particularly for single pin channels [46].

This work presents a friction factor dataset obtained from liquid sodium flow around the single wire wrapped fuel pin simulator in the SHTL experimental facility. A power law correlation is fit to the processed friction factor data, and these results are compared with other commonly used correlations for sodium, both for pipes and simple annular channels (Petukhov, 1970 & Colebrook, 1939) and for bundles of wire wrapped pins (Upgraded Cheng and Todreas,

2018) [81], [82], [83], [78], [79]. The dataset and correlation presented here represent a limited but meaningful technical contribution to the available experimental literature for channels with single wire wrapped pins, complementing the numerical and CFD-focused studies that have been done for this geometry with direct experimental measurements in liquid sodium [80], [44].

A local build of INL's Pronghorn Subchannel (SC) code was also modified to include the fit correlation, and pressure field results for a built-in EBR-II fuel assembly example case were compared to those from the default UCTD correlation used by Pronghorn SC [84], [85], [86], [87].

The experimental friction factor data collected has uses for validating SFR systems code analysis methods, such as the Pronghorn SC code in the MOOSE framework, and CFD software used in the nuclear industry, like STAR-CCM+ and Nek5000 [84], [71], [88]. The findings provide valuable guidance for future experiments with expanded and full-scale simulated SFR fuel assemblies and provide additional context to the heat transfer testing done in the same facility.

8.3 - Methods

The test section geometry and instrumentation setup of the SHTL facility are laid out in detail in chapter 3. A picture and diagram of the experimental facility are shown in figure 8-1 again for reference.

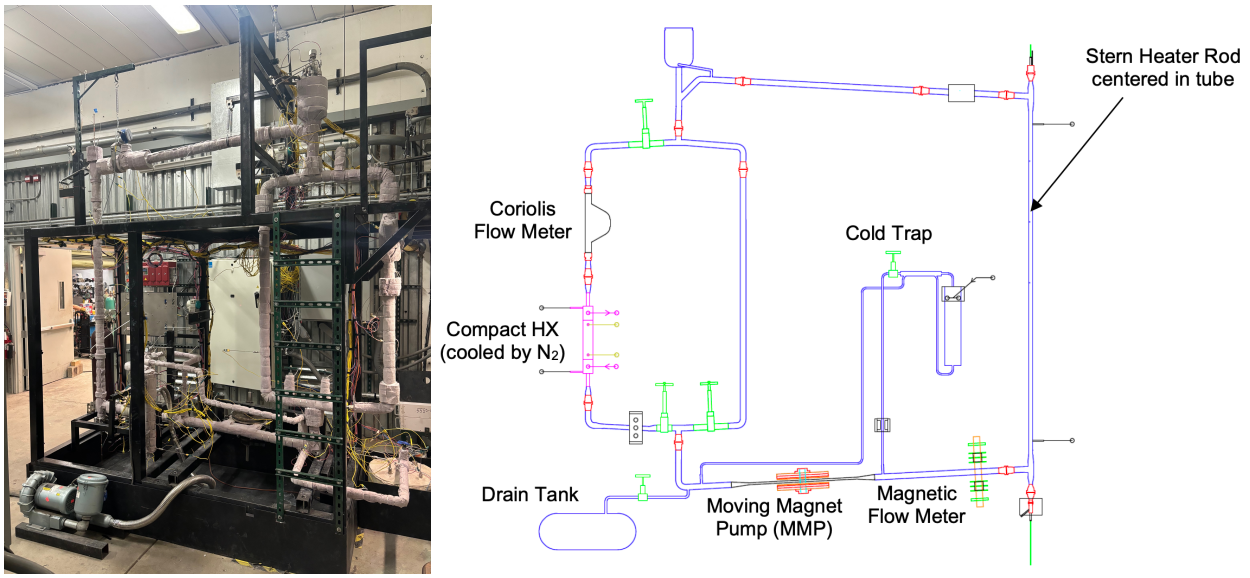

Figure 8-1: Sodium Heat Transfer Test Loop facility.

The test section pipe contained five sets of three centering pins that keep the fuel rod simulator located at the center of the test section and prevent buckling/bending. In addition to the primary heat transfer testing instrumentation, the outer test section pipe contained two pressure taps spaced 180 ± 0.16 cm (10 wire wrap pitches) apart vertically. These taps were coupled to a differential pressure transducer, and pressure drop data was recorded and used for this friction factor analysis [89]. The lower (high pressure side) pressure tap was located 8.048 ± 0.0625 in above the test section sodium inlet. Three of the five sets of three 1/16 inch locating pins protruding through the sodium channel and contacting the rod surface lay between the pressure taps. The test section also contained the three 1/32 inch outer diameter capillary tubes spanning through the annular sodium channel and coming within 0.050 inches of clearance from the fuel simulator cladding surface, used for the transverse FOTS sensors for heat transfer testing. Differential pressure data was also recorded with no sodium flow to capture the head difference, which was used to compensate in post-processing such that only frictional losses were used in the friction factor calculations.

Two series of steady state friction factor tests were conducted with the test section at isothermal conditions, and data was collected at three repetitions of nine different operating points each time (table 8-1). This amounted to 54 total recorded tests. Pressure drop measurements were obtained using the pressure transducer to investigate friction factor correlations with an uncertainty of 0.0055 psi. Permanent magnet electromagnetic flow meters measured sodium flow rate with an uncertainty of 0.0213 gpm. Data was recorded at a sampling frequency of 10 Hz for at least 1 minute per test case and was time averaged during post-processing. A steady state temperature criterion of changes of < 0.4 °C/min for the inlet and outlet sodium thermocouples was used. The test matrix encompassed Reynolds numbers ranging from ~9,000 – 75,000, and temperatures ranging from 200 °C to 550 °C.

Table 8-1: Isothermal friction factor test conditions matrix.

Test Case	Reynolds	Flow [gpm]	Temperature [°C]
01	70,000	7.52	550
02	40,000	4.30	550
03	10,000	1.07	550
04	70,000	7.94	500
05	70,000	9.09	400
06	70,000	10.90	300
07	70,000	12.24	200
08	40,000	6.99	200
09	10,000	1.75	200

Following completion of the experimental measurements, a complementary modeling effort was undertaken to investigate the applicability of friction factor data in existing SFR thermal hydraulics analysis tools. This phase included analyzing the pressure drop measurements and comparing to established friction factor correlations for pipes and simple channels in addition to correlations for wire wrapped rod bundles. Next, INL's Pronghorn SC source code

was updated to implement a newly developed friction factor correlation and compare the results against existing models via previously simulated example cases within Pronghorn SC.

8.4 - Results

The pressure drop (ΔP) data collected from the sodium loop experiment was post-processed and Darcy friction factors were calculated for each of the 54 test cases:

$$f = \frac{2\Delta P D_e}{L\rho u^2}, \qquad (8-1)$$

where D_e is the hydraulic diameter, L is the length between pressure taps, ρ is the sodium density, and u is the mean bulk velocity. Property correlations from Fink and Leibowitz (1995) and from Bomelburg and Smith (1972) were for sodium density and viscosity values respectively [5], [49]. A power law fit of the type $f = CRe^b$ was applied to the data with a least square fitting technique, and yielded the following correlation:

$$f = 0.2114Re^{-0.19} \qquad (8-2)$$

With a R^2 goodness of fit parameter of 0.9826 and a root mean square error (RMSE) of 0.00058. 95% prediction intervals for the fit are also overlaid with the experimental data and equation 8-2 power law correlation in figure 8-2.

The Colebrook equation (1939) (equation 8-3) and Petukhov correlation (1970) (equation 8-4) for smooth and rough pipes and simple channels were identified as widely used and cited correlations for liquid metals, and the hydraulic behavior of liquid sodium has been shown to be

quite similar to liquid water (similar density and viscosity to hot water) to the extent that liquid water is often used as a surrogate fluid in liquid sodium flow studies [8], [90]. These correlations are also applicable over a wide range of Reynolds numbers. The correlations were used as points of comparison for the friction factors calculated from the experimental test section, because of the relatively open/thick annular channel shape and smooth metallic surfaces, although the experimental setup does include a spiral wire wrapping and several protrusions into the flow channel.

$$\frac{1}{\sqrt{f}} = -2.0 \log_{10}\left(\frac{\frac{\epsilon}{D}}{3.7} + \frac{2.51}{Re\sqrt{f}}\right) \quad (8-3)$$

$$f = (0.790 \ln(Re) - 1.64)^{-2} \quad (8-4)$$

The UCTD correlation was identified as a widely used and well-established option for wire wrapped bundles [77], [78], [79], [91], [92]. It includes many geometrical parameters for describing flows through “interior” channels in the center of the bundle, “edge” channels where the rod bundle touches the hexagonal duct around it, and “corner” channels in the corners of the duct. This is also the correlation that is used by default in the Pronghorn SC code, and it was found to be in good agreement with data from existing experimental work with pin bundles [84]. The UCTD correlation for interior channels follows the form:

$$f_{T1} = C_{fT1} Re^{b} \quad (8-5)$$

$$C_{fT1} = C_{fT1}(P, D, H, per_{w1}, A_{c1}, \ldots) \quad (8-6)$$

$$b = -0.18 \qquad (8-7)$$

Where the C parameter is a function of bundle geometry (flow area, wrap pitch, rod spacing pitch, duct size, etc.). The corrected formulation per the published corrigendum to Chen et al. (2018) is used throughout [79]. This correlation applies to tightly packed hexagonal bundles with wire wraps typical of SFR fuel assemblies (~1.0 < P/D < 1.5).

To compare data from a channel with a single wire wrapped pin to the UCTD correlation, which is intended for bundles, it was necessary to define a channel type and method for deriving a bundle channel that was appropriate for comparison to the 1-pin experiment. An interior bundle channel with the same simulated fuel rod diameter and wire wrap diameter and pitch was drawn by matching the hydraulic diameter to that of the single pin annular channel experiment.

The friction factor data from the sodium loop experiment and its power law fit (equation 8-2) lie between the smooth annular channel correlations and the corrected UCTD bundle correlation, consistent with a channel geometry that falls between the two limiting cases represented by the correlations. The presence of the spiral wire wrap and centering pin sets and small transverse capillary tubes protruding into the flow increases the measured friction factor above what would be expected for a smooth annulus, while the relatively open channel geometry (P/D ~ 1.45 for an equivalent interior bundle channel with the same hydraulic diameter, rod diameter, and wire wrap geometry) results in friction factors below those predicted by UCTD for the more tightly packed hexagonal bundle subchannels for which it was developed. This behavior is expected, as the single pin annular test section shares characteristics with both geometry classes without being fully representative of either. The friction factor data points, uncertainty values, and correlations are presented on figure 8-2.

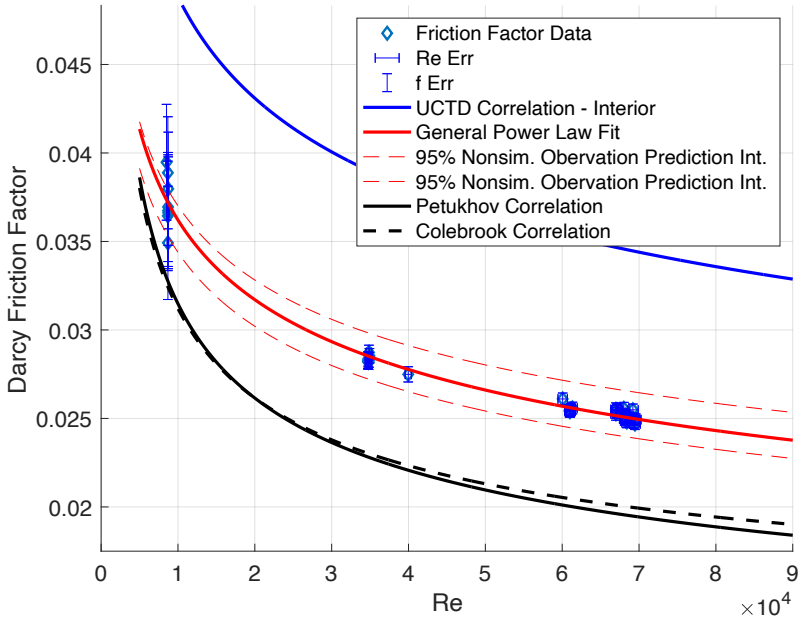

Figure 8-2: Friction factor vs Reynolds number plot with experimental data. Custom power law correlation and relevant pipe and pin bundle correlations are overlaid.

The power law correlation fit to the experimental data ($f = 0.2114Re^{-0.19}$) was implemented into a local build of Pronghorn SC, which uses the corrected UCTD correlation as its default treatment for friction factor in bundles of wire wrapped pins. The custom correlation was applied uniformly to all subchannels for an EBR-II validation case, and the resulting pressure fields predicted a pressure drop (ΔP) 6% higher than that obtained using the built-in UCTD formulation, which applies different friction factor correlations for interior, edge, and corner channels in the 91-pin EBR-II bundle, depending on geometry [86].

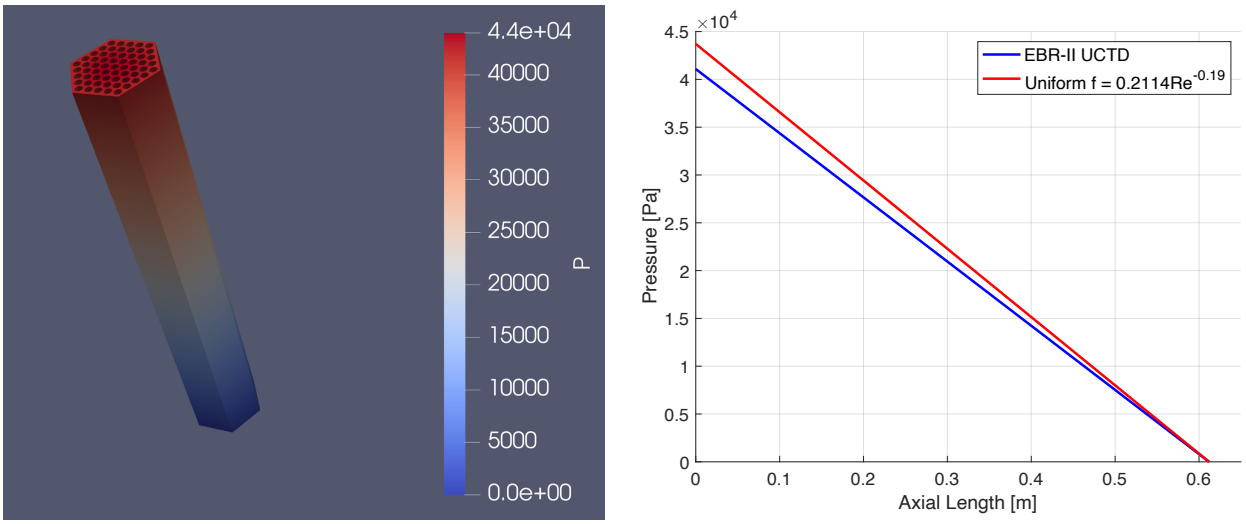

Figure 8-3: EBR-II example case pressure comparison in Pronghorn SC.

Although the UCTD correlation assigns a higher friction factor coefficient to *EBR-II interior bundle channels* ($f \sim 0.48Re^{-0.18}$ at P/D = 1.28) than the single pin fit correlation, the assembly level weighting across all subchannel types, where edge and corner channels carry substantially lower friction coefficients (closer to the smooth pipe curves), results in the custom correlation predicting slightly higher overall assembly ΔP when applied uniformly.

8.5 - Conclusions

This work presents a friction factor dataset and fits a power law correlation ($f = 0.2114Re^{-0.19}$) for liquid sodium flow around a single wire wrapped SFR fuel pin simulator. The measured friction factors lie between smooth annular channel correlations (Colebrook, 1939 & Petukhov, 1970) and the UCTD (2018) bundle correlation, consistent with the intermediate nature of the experimental geometry. The well characterized geometry, boundary conditions, and quantified experimental uncertainty make this dataset well suited for informing future studies of wire wrapped pin hydraulics [44], [80].

The power law fit correlation was implemented in a local build of Pronghorn SC and applied uniformly across all subchannels in a 91-pin EBR-II assembly example case, in contrast to the built-in UCTD formulation which assigns geometry-dependent friction factors separately to interior, edge, and corner subchannels. Despite this, the predicted assembly pressure drop differed by only approximately 6% from the UCTD result, suggesting that assembly level pressure drop prediction in Pronghorn SC is not strongly sensitive to the choice of friction factor correlation for this configuration and flow regime. The quantified prediction interval bounds on the fit correlation can also inform future uncertainty propagation through Pronghorn SC simulations.

It should be noted that this sensitivity assessment is limited in scope and generality. The comparison reflects a single experimental geometry, one example bundle configuration and flow condition, and one alternative correlation applied uniformly across all subchannel types. The 6% result may not generalize to other assembly geometries, pitch to diameter ratios, or flow conditions, and should not be interpreted as a broadly applicable conclusion about friction factor correlation sensitivity in the Pronghorn SC code. Rather, it represents a preliminary indication that systematic sensitivity studies incorporating multiple geometries and correlation forms would be a valuable direction for future work.

This work also provides hydraulic context supporting the heat transfer studies conducted in the same test section for which Nusselt number measurements and comparisons to CFD simulations of liquid sodium thermal hydraulics have been presented [70], [73]. The present study is well suited for validation of higher fidelity CFD simulations of liquid metal flows around wire wrapped pins, and further supports the development of modeling techniques, along with the content discussed in chapter 7.

Chapter 9 – Overall Conclusions

9.1 - Overview of Dissertation

This dissertation summarized the investigation of heat transfer behavior in liquid sodium flows under conditions representative of sodium fast reactor fuel assemblies, with an emphasis on generating high-resolution experimental data and developing methods for its interpretation. To accomplish this, high temperature distributed fiber optic temperature sensing techniques were developed and implemented in a sodium test facility, enabling detailed spatial measurements of temperature within and around a wire wrapped fuel pin simulator. These measurements were used to characterize overall heat transfer behavior in an annular flow geometry with a prototypic wire wrap and cosine shaped axial heat flux profile. CFD modeling and other finite element computational analysis tools were also applied to support interpretation of the experimental data and to assess the applicability of modeling approaches for liquid metal thermal hydraulics.

Taken together, the work presented here represents a coordinated effort to address key challenges associated with measuring and predicting heat transfer in liquid metal systems. The development of robust high-temperature FOTS instrumentation enabled the collection of a high-resolution dataset that captures spatial variations in temperature not typically resolved in many sodium experiments. Analysis of this dataset provided insight into both the overall heat transfer behavior and the physical mechanisms responsible for local temperature variations, which also occur in the fuel assemblies of operating SFRs. Complementary CFD modeling and code comparisons further clarified the relationship between measured temperatures and underlying thermal fields and demonstrated that combined experimental and computational approaches can be used to interpret complex conjugate heat transfer phenomena in wire wrapped geometries.

9.2 - Instrumentation Contributions

The development and implementation of high temperature distributed fiber optic temperature sensors suitable for use in liquid sodium environments was a central component of the research. Robust fabrication and installation techniques for deploying FOTSs within challenging geometries were established, including embedding sensors within the heater rod, *routing sensors through the hollow helical wire wrap*, and positioning sensors across the annular sodium flow channel. These configurations enabled measurement of temperatures in both the solid and fluid domains without significantly disturbing the flow, providing a level of spatial resolution not typically achieved in liquid metal heat transfer experiments.

Extensive calibration and validation efforts demonstrated that the FOTSs provided reliable temperature measurements under the operating conditions of the sodium loop. These efforts included controlled spool/lot calibrations, in-situ validation and verification against thermocouple measurements, and evaluation of potential measurement biases arising from mechanical strain, installation tolerances, etc. The resulting instrumentation approach was shown to be capable of operation in the SHTL test section at temperatures above 600 °C with well characterized uncertainty, establishing confidence in the measured temperature data used throughout the subsequent analyses.

Beyond its direct use in the experimental campaigns, the instrumentation work produced a practical and transferable methodology for high-resolution temperature measurement in high temperature liquid metal systems. The demonstrated ability to integrate fiber optic sensors within a challenging helical wire wrap geometry, in particular, provides a pathway for future application in larger, bundle scale experiments representative of full SFR fuel assemblies. The instrumentation contributions extend beyond the present study and provide a foundation for

future experimental investigations and model validation efforts in liquid metal thermal hydraulics.

9.3 - Findings of Heat Transfer Experiment

The experimental investigation conducted in this research work produced a high spatial resolution temperature dataset characterizing heat transfer to liquid sodium flow around a wire wrapped fuel pin simulator under conditions representative of SFR cores. Measurements were obtained over a range of heat flux conditions and flow rates corresponding to Peclet numbers on the order of ~40–400, capturing radial temperature distributions within the annular flow channel as well as detailed temperature profiles both axially and along the wire wrap. This dataset serves as a valuable resource for both physical interpretation of overall heat transfer behavior and model validation.

Analysis of the measured temperature profiles revealed that the axial temperature distribution along the wire wrap exhibits local variations on the order of ~10 °C over length scales comparable to the wire wrap half-pitch. These variations were shown to be physically consistent with the combined effects of heater filament eccentricity, positional variability of the wire wrap FOTS within the capillary, and spatially varying thermal contact resistances within the heater assembly. The high thermal conductivity of liquid sodium and the correspondingly low convective resistance at the rod surface amplify the influence of these internal conduction pathways, leading to measurable local variations in surface temperature fields even under nominally uniform operating conditions.

Despite these local variations, it was demonstrated that the overall heat transfer behavior of the system can be effectively characterized through appropriate spatial averaging of the

temperature data. When averaged over the central region of the heated length in the test section, the resulting Nusselt numbers were found to be in good agreement with established liquid metal heat transfer correlations, including those of Seban & Shimazaki (1951) and Bailey (1950, for annular geometries) [27], [36], [38], [39], [42], [69]. This result supports the applicability of these classical correlations to wire wrapped geometries with cosine-shaped axial heat flux profiles more characteristic of SFR heat transfer and reinforces the interpretation that previously reported deviations in low Peclet number liquid metal heat transfer data may be attributable, in part, to measurement limitations, experimental uncertainties, and systematic errors in data processing and assumptions [28], [36], [41].

The ability of the FOTSs to resolve the local temperature variations seen also has important implications beyond the present experiment. In actual SFR fuel, circumferential variations in surface temperature are expected to arise from factors such as fuel-cladding contact conditions, sodium bonding behavior, irradiation induced swelling/deformation, and interactions between neighboring pins within a bundle. The present measurements therefore demonstrate that the instrumentation approach is capable of capturing temperature variations of similar magnitude and spatial scale, supporting its potential application in larger bundle-scale experiments and future fuel performance investigations.

9.4 - Role of CFD

The CFD modeling performed provides a complementary framework for interpreting the high-resolution temperature measurements obtained in the experiment. Rather than serving as a standalone modeling study, the CFD analysis was used to evaluate whether established modeling approaches could reproduce the observed thermal behavior and to provide insight into how the

measured temperatures relate to the underlying conjugate heat transfer process. In this way, the CFD results extend the experimental findings by helping to explain the origin and meaning of features observed in the measured temperature profiles.

CFD simulations were found to reproduce the major thermal behaviors observed experimentally, including temperature distributions along the wire wrap, radial temperature gradients within the sodium flow, and overall heat transfer trends. An especially important finding was that the modeling results support the interpretation that the temperature measured within the hollow wire wrap corresponds closely to a perimeter averaged surface temperature around the fuel simulator and its wire wrap. This result provides additional confidence in the assumptions used in the experimental heat transfer analysis and reinforces the validity of using the wire wrap FOTS as a meaningful proxy for surface temperature in this geometry.

The simulations also provide a consistent explanation for the magnitude and spatial scale of the temperature variations observed along the wire wrap. By examining the effect of sensor position within its capillary, the CFD results demonstrate that positional variability of the fiber can produce temperature differences at scales that make sense with this effect being partly responsible for the variations measured experimentally. These findings are consistent with additional solid conduction analyses and support the conclusion that the observed fluctuations arise from a combination of geometric effects, internal conduction pathways, and measurement location variability, rather than from sensor error or measurement artifacts.

In addition to supporting interpretation of the wire wrap measurements, the CFD model was used to evaluate other aspects of the thermal field. Comparisons of radial temperature profiles showed good agreement between simulation and measurement, confirming the presence of measurable temperature gradients within the sodium flow and reinforcing the interpretation of

bulk temperature behavior in low Prandtl number fluids. Similarly, comparison of bulk temperature evolution along the test section demonstrated that axial conduction within the sodium is generally small for the conditions studied, becoming more noticeable only at lower flow rates. These results provide additional context for interpreting the experimental data and help establish the conditions under which simplified analysis approaches remain valid.

The CFD and experimental results provide consistent and mutually supporting evidence that the dominant heat transfer mechanisms in the present system are well captured by the modeling approach. This combined experimental-computational framework also demonstrates how high-resolution measurements and CFD analysis can be used together to improve understanding of complex conjugate heat transfer behavior in liquid metal systems relevant to SFR applications.

9.5 - Application to SFR Thermal Hydraulics

The findings discussed throughout the dissertation have relevance to the analysis and design of SFR systems, particularly in the context of heat transfer and temperature field prediction in and around wire wrapped fuel elements. Liquid metal thermal hydraulics in prototypic geometries remains an area where high-resolution experimental data are limited, and uncertainties in both measurement interpretation and modeling approaches can impact confidence in design decisions. The present work contributes to addressing this gap by providing a dataset that captures detailed temperature behavior in a geometry and operating regime representative of SFR core conditions.

By combining advanced instrumentation, high-resolution experimental measurements, and CFD-aided interpretation, this work demonstrates a framework for improving confidence in

both experimental and computational approaches to liquid metal heat transfer. The experimental results establish that *overall* heat transfer behavior can be reliably characterized through spatial averaging and use of known historical heat transfer correlations, even in the presence of local variability driven by geometric and conjugate effects. At the same time, the CFD comparisons provide insight into the physical meaning of measured temperatures and support the applicability of commonly used modeling approaches such as RANS and k-ω SST for predicting thermal behavior of liquid sodium flows in wire wrapped configurations.

More broadly, these results highlight the value of integrated experimental and modeling efforts for advancing thermal hydraulic understanding in liquid metal systems. The ability to generate and interpret high-resolution temperature data in complex geometries supports the continued development and validation of predictive tools such as CFD and systems level codes used in advanced reactor design and analysis. As such, the approaches developed in this work provide a foundation for future investigations of heat transfer and flow behavior in full scale SFR fuel assemblies and other related liquid metal heat exchange systems seeing similar flow conditions.

Several additional opportunities for future work follow naturally from this study. Extension of the instrumentation techniques and experimental methods to larger bundle scale geometries would enable investigation of multi-pin heat transfer and subchannel temperature distributions under conditions even more prototypic of SFR cores, and this is an area of work that is actively being pursued by other researchers. Additional work to better characterize internal conduction pathways and contact resistances within the heater assembly could further refine interpretation of local temperature variations. Continued validation of CFD and system level modeling tools against the present datasets and related configurations would also help

establish the broader applicability of these approaches for liquid sodium thermal hydraulic analysis.

References

[1] N. Stern, “The Economics of Climate Change,” *The American Economic Review*, vol. 98, no. 2, pp. 1–37, 2008.

[2] W. Nordhaus, “The ‘Stern Review’ on the Economics of Climate Change,” National Bureau of Economic Research, Cambridge, MA, w12741, Dec. 2006. doi: 10.3386/w12741.

[3] “GIF Portal - Sodium-Cooled Fast Reactor (SFR).” Accessed: Feb. 20, 2021. [Online]. Available: https://www.gen-4.org/gif/jcms/c_42152/sodium-cooled-fast-reactor-sfr

[4] B. S. Triplett, E. P. Loewen, and B. J. Dooies, “PRISM: A Competitive Small Modular Sodium-Cooled Reactor,” *Nuclear Technology*, vol. 178, no. 2, pp. 186–200, May 2012, doi: 10.13182/NT178-186.

[5] J. K. Fink and L. Leibowitz, “Thermodynamic and transport properties of sodium liquid and vapor,” ANL/RE--95/2, 94649, Jan. 1995. doi: 10.2172/94649.

[6] G. F. Nellis and S. A. Klein, *Introduction to Engineering Heat Transfer*, 1st ed. Cambridge University Press, 2021.

[7] B. Mays and R. B. Jackson, “Thermal Hydraulic Computational Fluid Dynamics Simulations and Experimental Investigation of Deformed Fuel Assemblies,” AREVA Federal Services, LLC, Charlotte, NC (United States), DOE-AFS--0008321-1, Mar. 2017. doi: 10.2172/1346027.

[8] F. Roelofs, V. R. Gopala, S. Jayaraju, A. Shams, and E. Komen, “Review of fuel assembly and pool thermal hydraulics for fast reactors,” *Nuclear Engineering and Design*, vol. 265, pp. 1205–1222, Dec. 2013, doi: 10.1016/j.nucengdes.2013.07.018.

[9] D. C. Crawford, D. L. Porter, and S. L. Hayes, “Fuels for sodium-cooled fast reactors: US perspective,” *Journal of Nuclear Materials*, vol. 371, no. 1, pp. 202–231, Sep. 2007, doi: 10.1016/j.jnucmat.2007.05.010.

[10] D. LaBrier, C. Pope, and W. Marcum, “On developing a practical safety culture for the advanced reactor workforce: Experiences of working with sodium,” *Front. Nucl. Eng.*, vol. 2, Mar. 2023, doi: 10.3389/fnuen.2023.1162751.

[11] “Sodium Coolant Handbook: Thermal Hydraulics Correlations.” International Atomic Energy Agency, Feb. 2024.

[12] C. B. Davis, “Evaluation of Fluid Conduction and Mixing Within a Subassembly of the Actinide Burner Test Reactor”.

[13] B. Prahlad, R. D. Kale, and K. K. R. Jan, “Thermal Performance Tests on a Sodium-to-Sodium Heat Exchanger”.

[14] T. H. Bauer, J. M. Kramer, R. W. Tilbrook, and A. J. Goldman, “A program to resolve the safety implications of fuel damage in the operation of advanced metal-fueled reactors,” ANL-IFR--103, 10200876, Feb. 1989. doi: 10.2172/10200876.

[15] Y. Miao *et al.*, “Metallic fuel cladding degradation model development and evaluation for BISON,” *Nuclear Engineering and Design*, vol. 385, p. 111531, Dec. 2021, doi: 10.1016/j.nucengdes.2021.111531.

[16] L. Ren, X. Tao, L. Zhang, M.-J. Ni, K.-Q. Xia, and Y.-C. Xie, “Flow states and heat transport in liquid metal convection,” *J. Fluid Mech.*, vol. 951, p. R1, Nov. 2022, doi: 10.1017/jfm.2022.866.

[17] P. G. Medvedev, “BISON Investigation of the Effect of the Fuel- Cladding Contact Irregularities on the Peak Cladding Temperature and FCCI Observed in AFC-3A Rodlet 4,” INL/EXT--16-40027, 1364503, Sep. 2016. doi: 10.2172/1364503.

[18] N. Dodds and S. Henslee, “Sodium Bond Defect Investigations,” ANL--IFR-131, 1548400, 154054, Mar. 1990. doi: 10.2172/1548400.

[19] Y. Miao, N. Stauff, A. Oaks, A. M. Yacout, and T. K. Kim, “Fuel performance evaluation of annular metallic fuels for an advanced fast reactor concept,” *Nuclear Engineering and Design*, vol. 352, p. 110157, Oct. 2019, doi: 10.1016/j.nucengdes.2019.110157.

[20] Y. Peet and P. Fischer, “Heat Transfer LES Simulations in Application to Wire-Wrapped Fuel Pins,” in *10th AIAA/ASME Joint Thermophysics and Heat Transfer Conference*, American Institute of Aeronautics and Astronautics. doi: 10.2514/6.2010-4318.

[21] G. Nellis and S. Klein, *Heat Transfer*. Cambridge University Press, 2008.

[22] R. N. Lyon, *Forced Convection Heat Transfer Theory and Experiments with Liquid Metals*. United States Atomic Energy Commission, Technical Information Service, 1949.

[23] C. Jackson, R. Miller, R. Tidball, R. Werner, and H. Grantz, “Liquid-metals Handbook,” *Atomic Energy Commison*, Jun. 1955.

[24] “Convective Heat and Mass Transfer - S. Mostafa Ghiaasiaan - Google Books.” Accessed: Dec. 14, 2023. [Online]. Available: https://books.google.com/books?hl=en&lr=&id=zNFfDwAAQBAJ&oi=fnd&pg=PT22&dq=Ghiaasiaan+Convective+Heat+and+Mass+Transfer&ots=OmVcr4F_rF&sig=4Kgyc5_jhg_rTcRAkKRQNtPhgj8#v=onepage&q=Ghiaasiaan%20Convective%20Heat%20and%20Mass%20Transfer&f=false

[25] R. C. Martinelli, “Heat transfer to molten metals,” *Trans. Am. Soc. Mech. Eng.*, vol. 69, pp. 947–959, 1947.

[26] R. N. Lyon, “Liquid metal heat transfer coefficients,” *Chem. Eng. Prog.*, vol. 47, pp. 75–79, 1951.

[27] R. A. Seban and T. Shimazaki, “Heat transfer to a fluid flowing turbulently in a smooth pipe with walls at constant temperature,” CALIFORNIA UNIV BERKELEY INST OF ENGINEERING RESEARCH, 1949.

[28] Y. Wu *et al.*, “Review on heat transfer and flow characteristics of liquid sodium (1): Single-phase,” *Progress in Nuclear Energy*, vol. 104, pp. 306–316, Apr. 2018, doi: 10.1016/j.pnucene.2017.11.004.

[29] H. A. Johnson, *Heat transfer to mercury in turbulent pipe flow*, vol. 2627. US Atomic Energy Commission, Technical Information Service, 1953.

[30] H. A. Johnson, J. P. Hartnett, and W. J. Clabaugh, “Heat transfer to lead-bismuth and mercury in laminar and transition pipe flow,” Institute of Engineering Research, Univ. of Calif., Berkeley, 1953.

[31] P. A. Ushakov, V. I. Subbotin, B. N. Gabrianovich, V. D. Talanov, and I. P. Sviridenko, “Heat transfer and hydraulic resistance in tightly packed corridor bundle of rods,” *Soviet Atomic Energy*, vol. 13, no. 2, pp. 761–768, 1963.

[32] V. I. Subbotin, A. K. Papovyants, P. L. Kirillov, and N. N. Ivanovskii, “A study of heat transfer to molten sodium in tubes,” *The Soviet Journal of Atomic Energy*, vol. 13, no. 4, pp. 991–994, Jun. 1963, doi: 10.1007/BF01480861.

[33] E. Skupinski, J. Tortel, and L. Vautrey, “Determination des coefficients de convection d’un alliage sodium-potassium dans un tube circulaire,” *International Journal of Heat and Mass Transfer*, vol. 8, no. 6, pp. 937–951, 1965.

[34] N. A. Ampleyev, “Heat transfer with liquid metal in a vertical pipe at low Peclet numbers(Liquid metal heat transfer in vertical pipes at low Peclet numbers),” *1969.*, pp. 8–27, 1969.

[35] A. Ono, H. Kamide, J. Kobayashi, N. Doda, and O. Watanabe, “An experimental study on natural circulation decay heat removal system for a loop type fast reactor,” *Journal of Nuclear Science and Technology*, vol. 53, no. 9, pp. 1385–1396, 2016.

[36] H. Mochizuki, “Consideration on Nusselt numbers of liquid metals under low Peclet number conditions,” *Nuclear Engineering and Design*, vol. 339, pp. 171–180, Dec. 2018, doi: 10.1016/j.nucengdes.2018.09.010.

[37] D. Elser, *Heat Transfer Measurements with Mercury*. University of California, Institute of Engineering Research, 1949.

[38] B. Lubarsky and S. Kaufman, “Review of Experimental Investigation of Liquid-metal Heat Transfer,” *National Advisory Committee for Aeronautics*, 1955.

[39] R. A. Seban, *Heat transfer measurements on lead bismuth eutectic in turbulent pipe flow*. University of California, Institute of Engineering Research, 1950.

[40] H. Mochizuki and M. Takano, “Heat transfer in heat exchangers of sodium cooled fast reactor systems,” *Nuclear Engineering and Design*, vol. 239, no. 2, pp. 295–307, Feb. 2009, doi: 10.1016/j.nucengdes.2008.10.013.

[41] H. Mochizuki, “Liquid metal heat transfer in heat exchangers under low flow rate conditions,” *Journal of Nuclear Science and Technology*, vol. 52, no. 6, pp. 821–828, Jun. 2015, doi: 10.1080/00223131.2014.980349.

[42] R. V. Bailey, “Heat transfer to metals in concentric annuli,” *Oak Ridge Natl. Lab., Oak Ridge, TN, ORNL*, vol. 521, 1950.

[43] K. Haga, Y. Daigo, A. Ohtsubo, and Y. Kikuchi, “Effects of bowing distortions on heat transfer in a seven-pin bundle,” 1974, Accessed: Oct. 31, 2025. [Online]. Available: https://inis.iaea.org/records/5ez2f-m7s21

[44] R. Ranjan, C. Pantano, and P. Fischer, “Direct simulation of turbulent heat transfer in swept flow over a wire in a channel,” *International Journal of Heat and Mass Transfer*, vol. 54, no. 21, pp. 4636–4654, Oct. 2011, doi: 10.1016/j.ijheatmasstransfer.2011.06.013.

[45] E. Merzari, W. D. Pointer, J. G. Smith, A. Tentner, and P. Fischer, “Numerical simulation of the flow in wire-wrapped pin bundles: Effect of pin-wire contact modeling,” *Nuclear Engineering and Design*, vol. 253, pp. 374–386, Dec. 2012, doi: 10.1016/j.nucengdes.2011.09.030.

[46] J.-H. Jeong, M.-S. Song, and K.-L. Lee, “Thermal-hydraulic effect of wire spacer in a wire-wrapped fuel bundles for SFR,” *Nuclear Engineering and Design*, vol. 320, pp. 28–43, Aug. 2017, doi: 10.1016/j.nucengdes.2017.05.019.

[47] B. Cheng-jean Chen and N. E. Todreas, “Prediction of the coolant temperature field in a breeder reactor including interassembly heat transfer,” *Nuclear Engineering and Design*, vol. 35, no. 3, pp. 423–440, Dec. 1975, doi: 10.1016/0029-5493(75)90072-2.

[48] C. J. Simons, “INVESTIGATION OF EROSION/CRROSION AND THERMAL-HYDRAULIC BEHAVIOR OF PROTOTYPIC SODIUM FAST REACTOR COMPONENTS,” Master of Science (Mechanical Engineering), University of Wisconsin - Madison, 2025.

[49] O. J. Foust, *Sodium-NaK Engineering Handbook*, 5 vols. Gordon and Breach, Science Publishers Inc., 1972.

[50] A. Luna, T. A. Moreira, M. Corradini, and M. Anderson, “Fiber Optic Sensors for Monitoring Elongation, Swelling, and Temperature in a Simulated Nuclear Fuel Cladding,” IEEE Sensors, 2025.

[51] A. Luna, “Optic Fiber Temperature Sensing at High Temperatures Ranging from 650 [C] to 750 [C],” p. 9.

[52] T. Moreira, N. Thoreson, S. Rabaey, A. Luna, and M. Anderson, “Distributed Temperature Sensing Optical Fiber Resolution, Accuracy, and Response Time for High-Temperature Applications,” University of Wisconsin - Madison, Jan. 2026.

[53] M. Weathered, J. Rein, M. Anderson, P. Brooks, and B. Coddington, “Characterization of Thermal Striping in Liquid Sodium With Optical Fiber Sensors,” *Journal of Nuclear Engineering and Radiation Science*, vol. 3, no. 4, p. 041003, Oct. 2017, doi: 10.1115/1.4037118.

[54] M. T. Weathered and M. H. Anderson, “On the Development of a Robust Optical Fiber-Based Level Sensor,” *IEEE Sensors Journal*, vol. 18, no. 2, pp. 583–588, Jan. 2018, doi: 10.1109/JSEN.2017.2777801.

[55] J. Schneider and M. Anderson, “Using optical fibers to examine thermal mixing of liquid sodium in a pool-type geometry,” *International Journal of Heat and Mass Transfer*, vol. 158, p. 119968, Sep. 2020, doi: 10.1016/j.ijheatmasstransfer.2020.119968.

[56] J. A. Schneider and M. Anderson, “Studying the effect of the upper internal structure design on thermal stratification in sodium fast reactors,” *Nuclear Engineering and Design*, vol. 385, p. 111501, Dec. 2021, doi: 10.1016/j.nucengdes.2021.111501.

[57] C. Simons, D. McCormick, R. Belgarde, T. A. Moreira, and M. H. Anderson, “The effect of high velocity liquid sodium flow on erosion/corrosion of orifice plates for use in sodium fast reactors,” *Nuclear Engineering and Design*, vol. 446, p. 114566, Jan. 2026, doi: 10.1016/j.nucengdes.2025.114566.

[58] A. Napora, “Oxygen Measurement and Control in Liquid Sodium Systems,” Ph.D., The University of Wisconsin - Madison, United States -- Wisconsin, 2024. Accessed: Aug. 24, 2025. [Online]. Available: https://www.proquest.com/docview/3067413532/abstract/5283F0B305C24606PQ/1

[59] A. C. Napora, R. L. Belgarde, T. A. Moreira, and M. H. Anderson, “Analysis of plugging meter measurement techniques for oxygen concentration determination in liquid sodium,” *Nuclear Engineering and Design*, vol. 421, p. 113112, May 2024, doi: 10.1016/j.nucengdes.2024.113112.

[60] M. Anderson and P. Brooks, “THL-FORM-0802-04 - Outside Instrument Calibration Certificate EMRS-CMFM-Q1-001.” UW-Madison THL, Mar. 12, 2024.

[61] C. Simons, D. McCormick, R. Belgarde, T. Moreira, and M. H. Anderson, “The Effect of High Velocity Liquid Sodium Flow on Erosion/Corrosion of Orifice Plates for Use in

Sodium Fast Reactors," Jun. 13, 2025, *Social Science Research Network, Rochester, NY*: 5293575. doi: 10.2139/ssrn.5293575.

[62] D. P. McCormick, "Design of a Test Facility for Orifice Corrosion in Liquid Sodium," Master of Science (Mechanical Engineering), University of Wisconsin - Madison, Madison, WI, 2023.

[63] M. Weathered, C. Grandy, M. Anderson, and D. Lisowski, "High Temperature Sodium Submersible Flowmeter Design and Analysis," *IEEE Sensors J.*, vol. 21, no. 15, pp. 16529–16537, Aug. 2021, doi: 10.1109/JSEN.2021.3079713.

[64] C. Simons, T. Moreira, and M. Anderson, "THL-OCL-PROC-1801 Electromagnetic Flow Meter Calibration Procedure." UW-Madison THL, Mar. 08, 2024.

[65] K. Miah and D. Potter, "A Review of Hybrid Fiber-Optic Distributed Simultaneous Vibration and Temperature Sensing Technology and Its Geophysical Applications," *Sensors*, vol. 17, p. 2511, Nov. 2017, doi: 10.3390/s17112511.

[66] M. Nakazawa, "Rayleigh backscattering theory for single-mode optical fibers," *J. Opt. Soc. Am.*, vol. 73, no. 9, p. 1175, Sep. 1983, doi: 10.1364/JOSA.73.001175.

[67] M. S. Wolfe, L. Technologies, and L. Technologies, "Distributed Fiber-Optic Temperature Sensing using Rayleigh Backscatter," p. 2.

[68] S. T. Kreger *et al.*, "High-resolution extended distance distributed fiber-optic sensing using rayleigh backscatter," presented at the The 14th International Symposium on: Smart Structures and Materials & Nondestructive Evaluation and Health Monitoring, K. J. Peters, Ed., San Diego, California, Apr. 2007, p. 65301R. doi: 10.1117/12.720913.

[69] *Sodium coolant handbook: thermal hydraulic correlations : IAEA project on sodium properties and safe operation of experimental facilities in support of the development and deployment of sodium cooled fast reactors (NAPRO)*. Vienna: International Atomic Energy Agency, 2024.

[70] N. J. Thoreson and M. H. Anderson, "High-Resolution Measuerments of Liquid Sodium Heat Transfer on a Wire Wrapped Rod with a Prototypic Fuel Pin Heat Flux Profile," University of Wisconsin - Madison, Mar. 2026.

[71] *Simcenter STAR-CCM+*. Siemens. [Online]. Available: https://www.siemens.com/en-us/products/simcenter/fluids-thermal-simulation/star-ccm/

[72] H. Barthod and G. P. Mignot, "CFD assessment of the uncertainty of temperature measurements with fiber optics (DTS) in Sodium Fast Reactors (SFR)," Oregon State University, Mar. 26, 2026.

[73] N. J. Thoreson and M. H. Anderson, "Comparison of High-Resolution Liquid Sodium Heat Transfer Measurements with CFD Modeling of a Wire Wrapped Fuel Rod Simulator," University of Wisconsin - Madison, Mar. 2026.

[74] C. Bourdot Dutra, L. Aldeia Machado, and E. Merzari, “Direct Numerical Simulation of Heat Transfer in a 7-Pin Wire-Wrapped Rod Bundle,” *Nuclear Science and Engineering*, vol. 198, no. 7, pp. 1439–1454, Jul. 2024, doi: 10.1080/00295639.2023.2246778.

[75] S. Vietz, “A Numerical Investigation into Capillary-Wrapped Liquid Sodium Pin-Bundles for Instrumentation Development.”

[76] N. J. Thoreson, M. Tano Retamales, P. Sabharwall, and M. H. Anderson, “Experimental Friction Factor Measurements in Liquid Sodium Around a Wire Wrapped Pin and Application in Pronghorn SC Code,” University of Wisconsin - Madison, Jan. 2026.

[77] S.-K. Cheng and N. E. Todreas, “Hydrodynamic models and correlations for bare and wire-wrapped hexagonal rod bundles — Bundle friction factors, subchannel friction factors and mixing parameters,” *Nuclear Engineering and Design*, vol. 92, no. 2, pp. 227–251, Apr. 1986, doi: 10.1016/0029-5493(86)90249-9.

[78] S. K. Chen, Y. M. Chen, and N. E. Todreas, “The upgraded Cheng and Todreas correlation for pressure drop in hexagonal wire-wrapped rod bundles,” *Nuclear Engineering and Design*, vol. 335, pp. 356–373, Aug. 2018, doi: 10.1016/j.nucengdes.2018.05.010.

[79] S. K. Chen, Y. M. Chen, and N. E. Todreas, “Corrigendum to ‘The upgraded Cheng and Todreas correlation for pressure drop in hexagonal wire-wrapped rod bundles’ [Nucl. Eng. Des. 335 (2018) 356–373],” *Nuclear Engineering and Design*, vol. 340, p. 414, Dec. 2018, doi: 10.1016/j.nucengdes.2018.10.009.

[80] Y. Peet and P. Fischer, “Heat Transfer LES Simulations in Application to Wire-Wrapped Fuel Pins,” in *10th AIAA/ASME Joint Thermophysics and Heat Transfer Conference*, Chicago, Illinois: American Institute of Aeronautics and Astronautics, Jun. 2010. doi: 10.2514/6.2010-4318.

[81] B. S. Petukhov, “Heat Transfer and Friction in Turbulent Pipe Flow with Variable Physical Properties,” in *Advances in Heat Transfer*, vol. 6, Elsevier, 1970, pp. 503–564. doi: 10.1016/S0065-2717(08)70153-9.

[82] C. F. Colebrook, “TURBULENT FLOW IN PIPES, WITH PARTICULAR REFERENCE TO THE TRANSITION REGION BETWEEN THE SMOOTH AND ROUGH PIPE LAWS.,” *Journal of the Institution of Civil Engineers*, vol. 11, no. 4, pp. 133–156, Feb. 1939, doi: 10.1680/ijoti.1939.13150.

[83] G. Keady, “Colebrook-White Formula for Pipe Flows,” *Journal of Hydraulic Engineering*, vol. 124, no. 1, pp. 96–97, Jan. 1998, doi: 10.1061/(ASCE)0733-9429(1998)124:1(96).

[84] V. Kyriakopoulos, M. E. Tano, and A. Karahan, “Demonstration of Pronghorn’s Subchannel Code Modeling of Liquid-Metal Reactors and Validation in Normal Operation Conditions and Blockage Scenarios,” *Energies*, vol. 16, no. 6, Art. no. 6, Jan. 2023, doi: 10.3390/en16062592.

[85] M. Tano Retamales, S. Schunert, V. Kyriakopoulos, A. Karahan, and A. Novak, "Development of a Subchannel Capability for Liquid-Metal Fast Reactors in Pronghorn," INL/RPT--22-67887-Rev000, 2279162, Jun. 2022. doi: 10.2172/2279162.

[86] M. Tano, V. Kyriakopoulos, J. McCay, and T. Arment, "Validation of Pronghorn's subchannel code using EBR-II shutdown heat removal tests: SHRT-17 and SHRT-45R," *Nuclear Engineering and Design*, vol. 416, p. 112783, Jan. 2024, doi: 10.1016/j.nucengdes.2023.112783.

[87] V. Kyriakopoulos, *Pronghorn SC*. (2023). Idaho National Laboratory.

[88] P. Fischer, *Nek5000*. Argonne National Laboratory. [Online]. Available: https://nek5000.mcs.anl.gov/

[89] N. J. Thoreson, M. H. Anderson, and M. Martin, "Heat Transfer Performance of a Wire-Wrapped Sodium Fast Reactor Fuel Rod Simulator," in *Transactions of the American Nuclear Society*, Washington, D.C.: American Nuclear Society, Nov. 2023, pp. 135–138.

[90] H. J. Bomelburg, "An Evaluation of the Applicability of Water Model Testing to Liquid Metal Engineering Problems," *OSTI.gov*, Feb. 1968.

[91] S. K. Chen, R. Petroski, and N. E. Todreas, "Numerical implementation of the Cheng and Todreas correlation for wire wrapped bundle friction factors-desirable improvements in the transition flow region," *Nuclear Engineering and Design*, vol. 263, pp. 406–410, Oct. 2013, doi: 10.1016/j.nucengdes.2013.06.012.

[92] S. K. Chen, N. E. Todreas, and N. T. Nguyen, "Evaluation of existing correlations for the prediction of pressure drop in wire-wrapped hexagonal array pin bundles," *Nuclear Engineering and Design*, vol. 267, pp. 109–131, Feb. 2014, doi: 10.1016/j.nucengdes.2013.12.003.

Appendices

Appendix A: Isothermal Validation Test Campaign Data

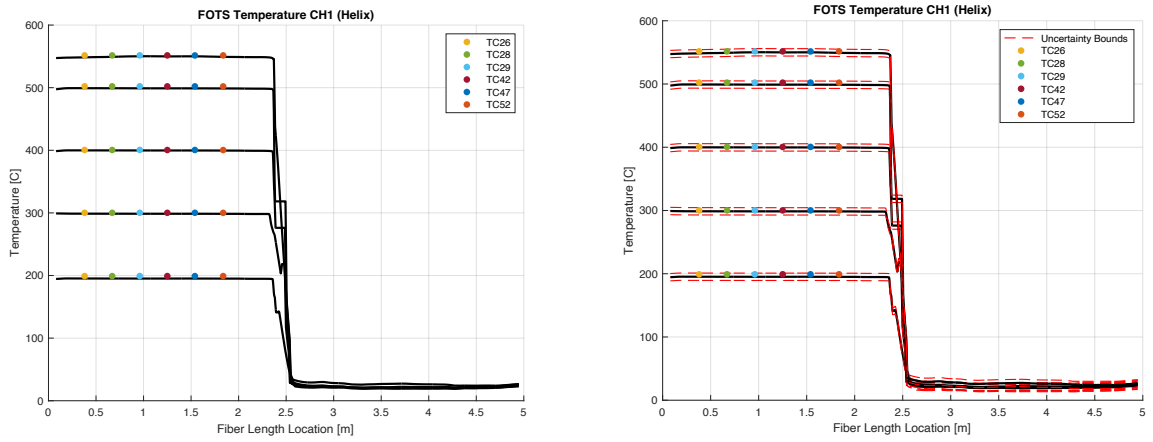

Figure A1: Output of FOTS inside helix wrapped capillary versus internal Stern rod thermocouples ($\dot{q} = 0$).

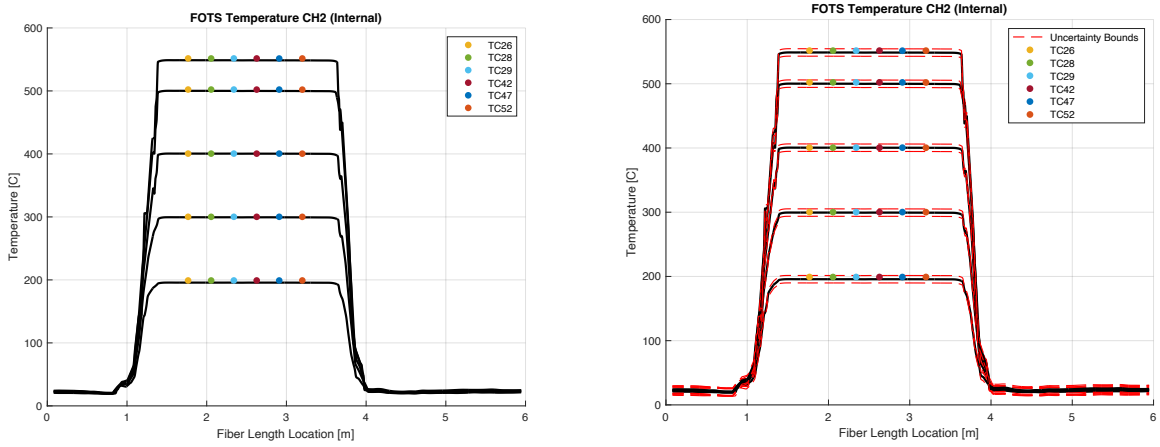

Figure A2: Output of channel 2 internal/embedded FOTS versus internal Stern rod thermocouples ($\dot{q} = 0$).

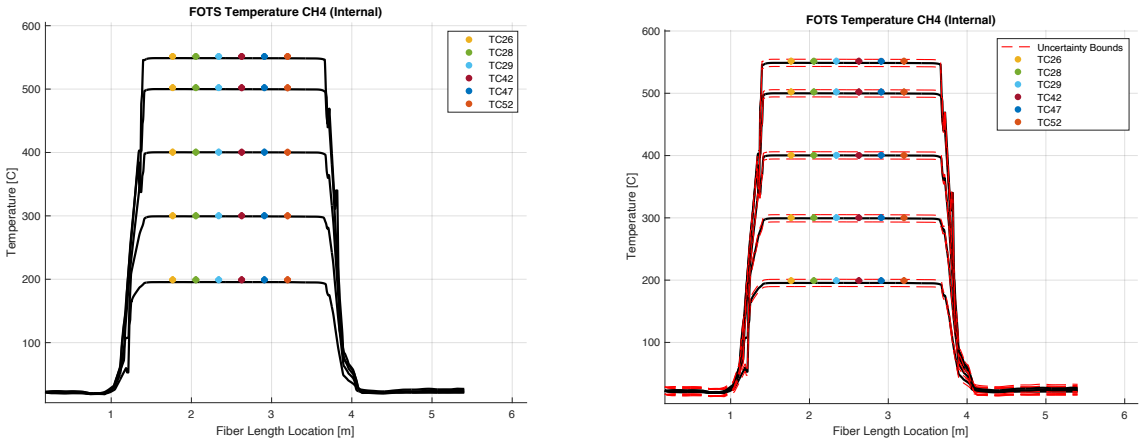

Figure A3: Output of channel 4 internal/embedded FOTS versus internal Stern rod thermocouples ($\dot{q} = 0$).

Appendix B: Heat Transfer Test Data

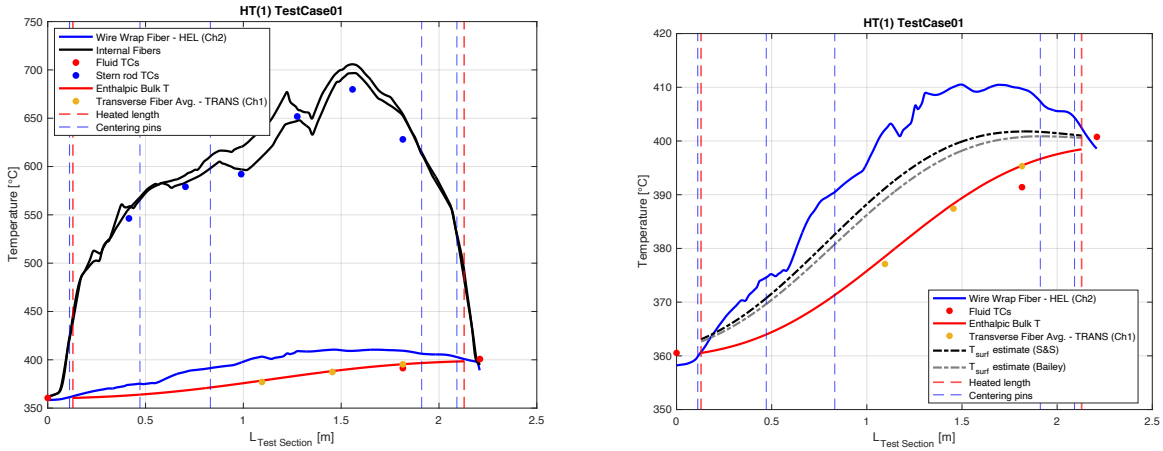

Figure B1: HT(1) Test Case 01 temperatures (Pe = 381, $\dot{q}$ = 25.7 kW).

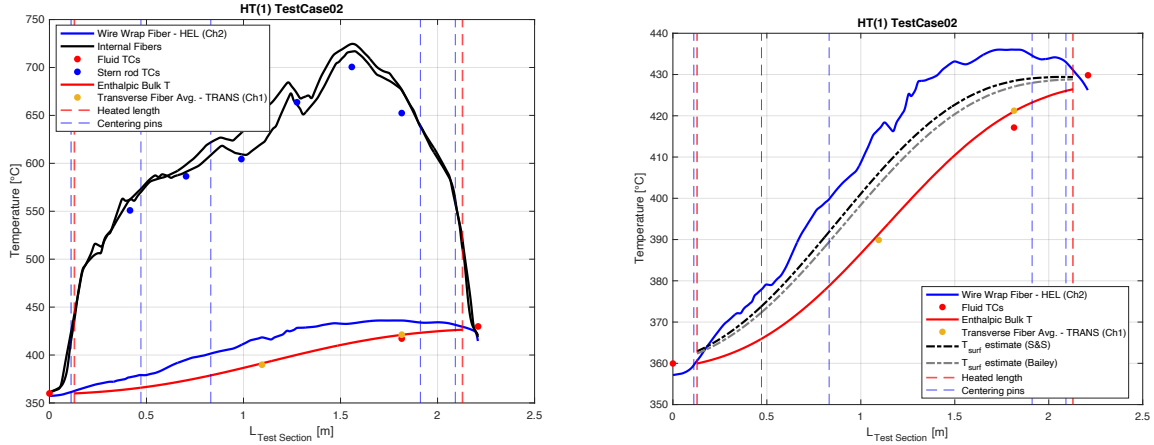

Figure B2: HT(1) Test Case 02 temperatures (Pe = 221, $\dot{q}$ = 25.7 kW).

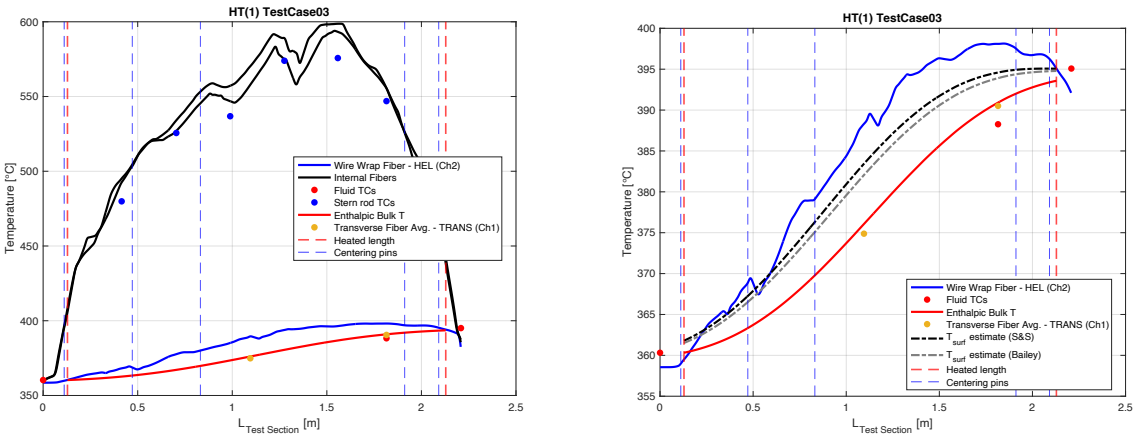

Figure B3: HT(1) Test Case 03 temperatures (Pe = 219, $\dot{q}$ = 13.0 kW).

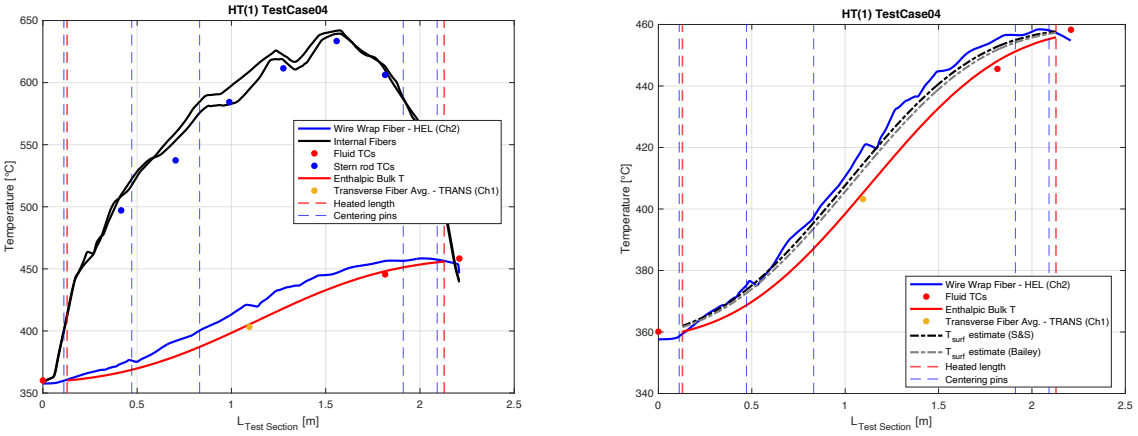

Figure B4: HT(1) Test Case 04 temperatures (Pe = 84, $\dot{q}$ = 13.8 kW).

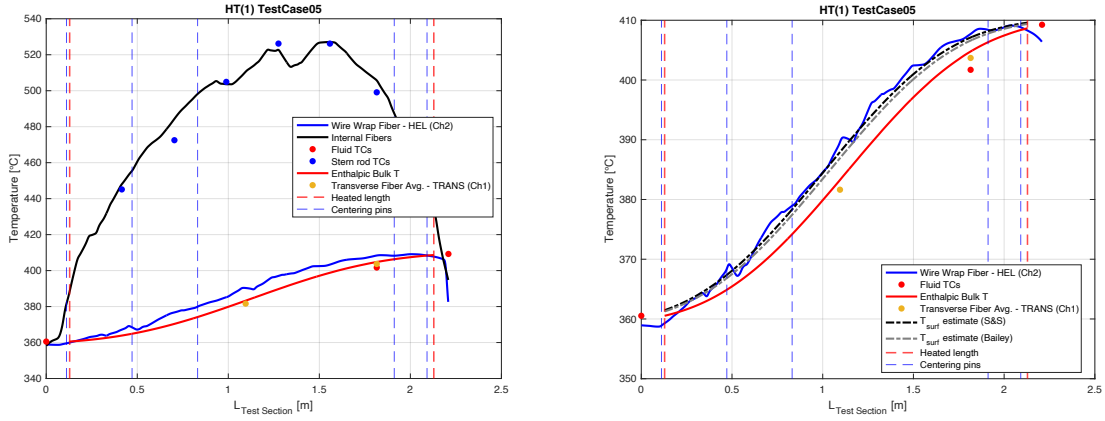

Figure B5: HT(1) Test Case 05 temperatures (Pe = 82, $\dot{q}$ = 7.0 kW).

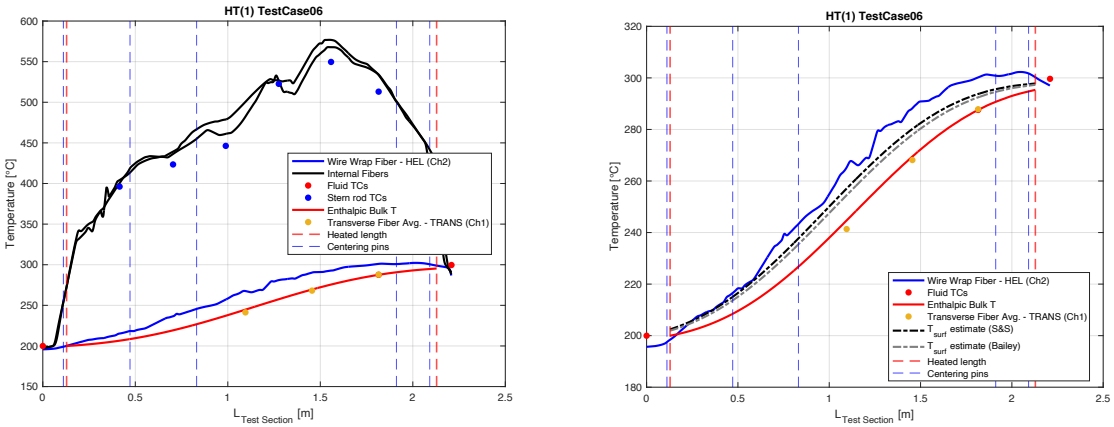

Figure B6: HT(1) Test Case 06 temperatures (Pe = 115, $\dot{q}$ = 21.5 kW).

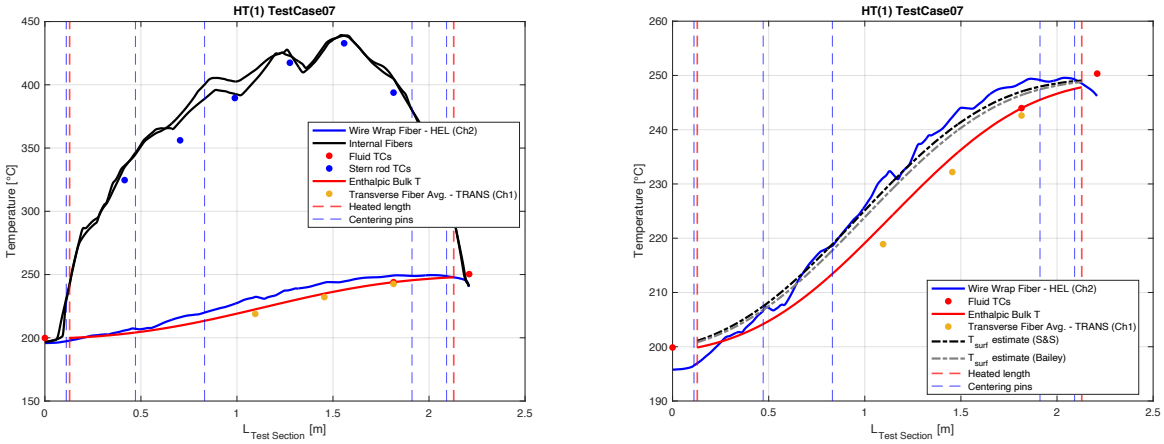

Figure B7: HT(1) Test Case 07 temperatures (Pe = 113, $\dot{q}$ = 10.9 kW).

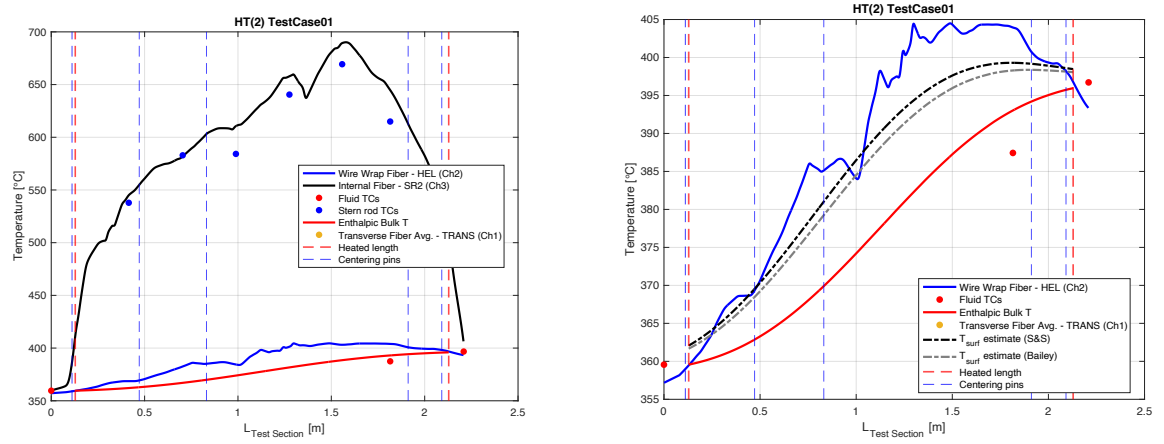

Figure B8: HT(2) Test Case 01 temperatures (Pe = 397, $\dot{q}$ = 25.7 kW).

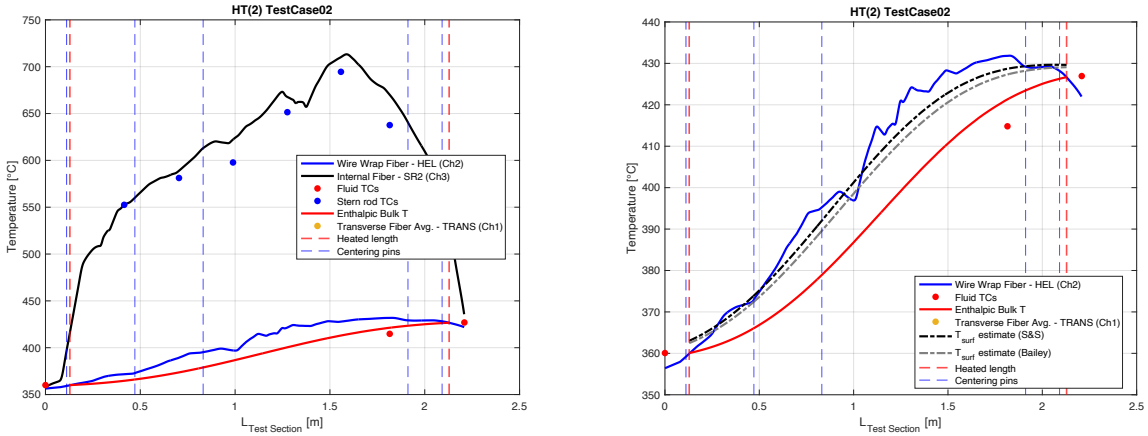

Figure B9: HT(2) Test Case 02 temperatures (Pe = 220, $\dot{q}$ = 25.7 kW).

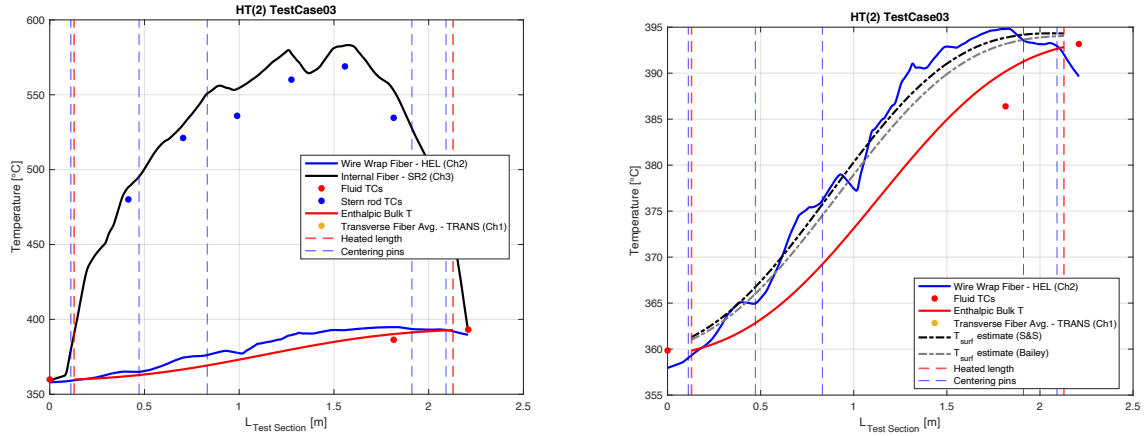

Figure B10: HT(2) Test Case 03 temperatures (Pe = 220, $\dot{q}$ = 13.0 kW).

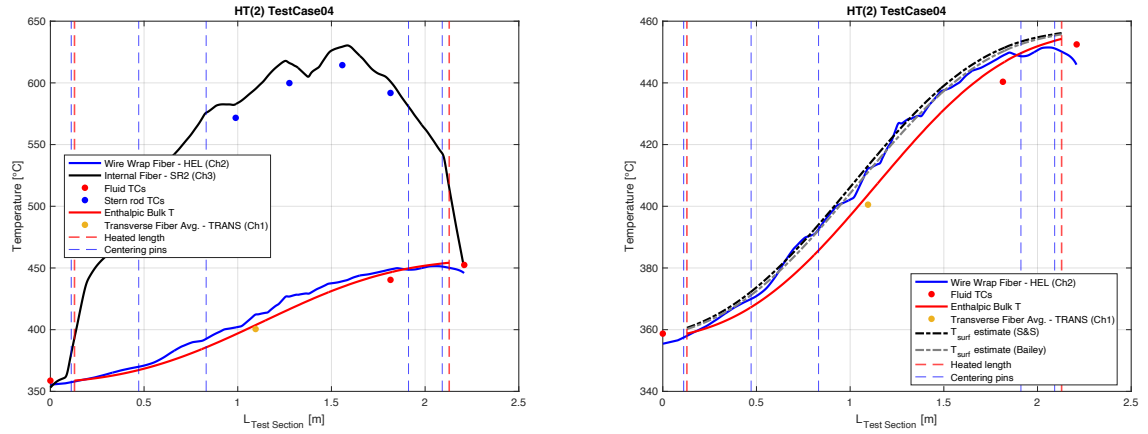

Figure B11: HT(2) Test Case 04 temperatures (Pe = 83, $\dot{q}$ = 13.8 kW).

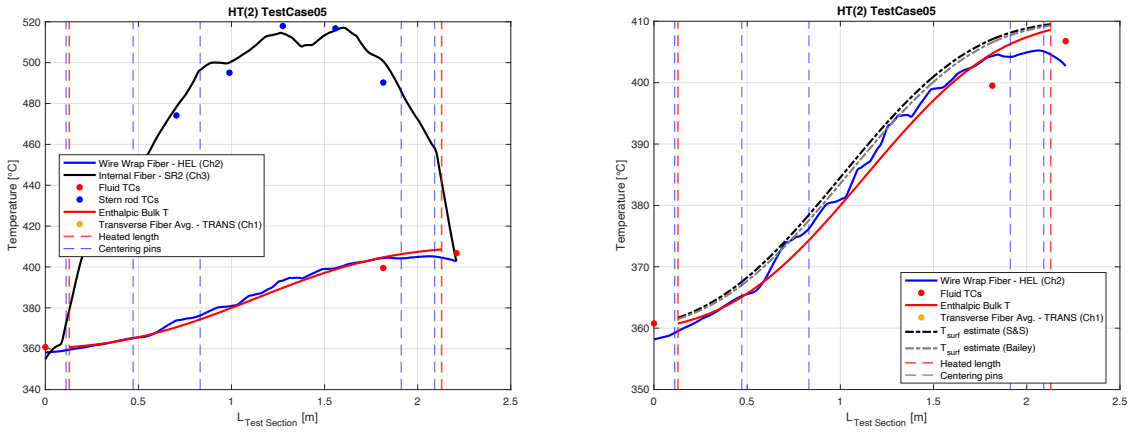

Figure B12: HT(2) Test Case 05 temperatures (Pe = 82, $\dot{q}$ = 7.0 kW).

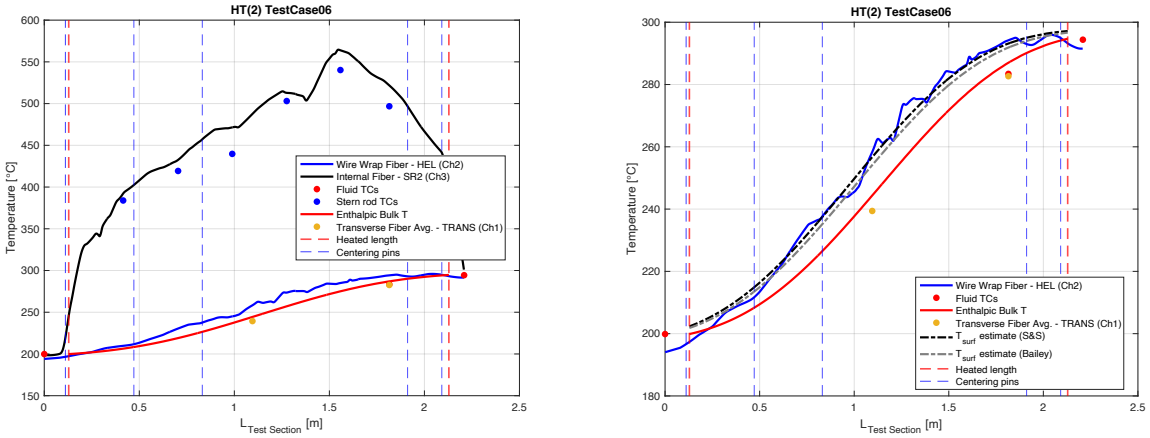

Figure B13: HT(2) Test Case 06 temperatures (Pe = 115, $\dot{q}$ = 21.5 kW).

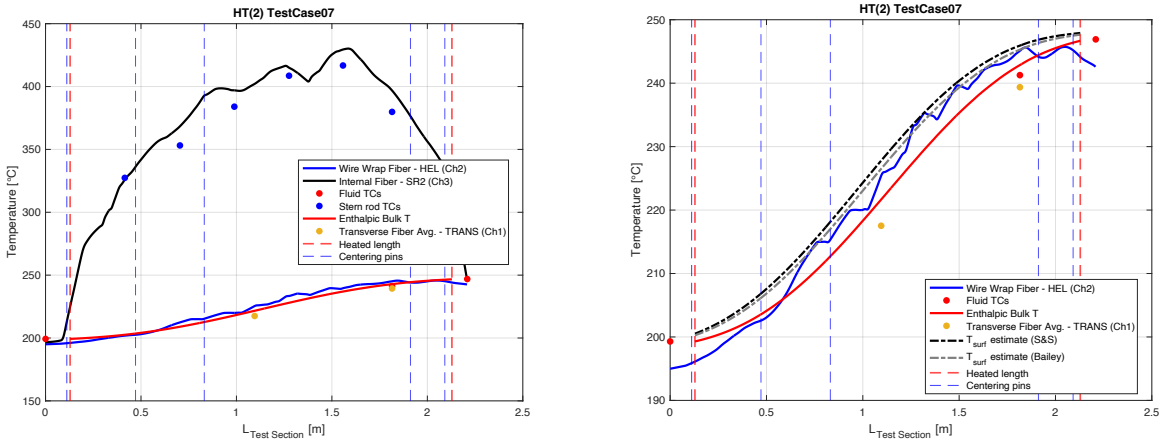

Figure B14: HT(2) Test Case 07 temperatures (Pe = 114, $\dot{q}$ = 10.9 kW).

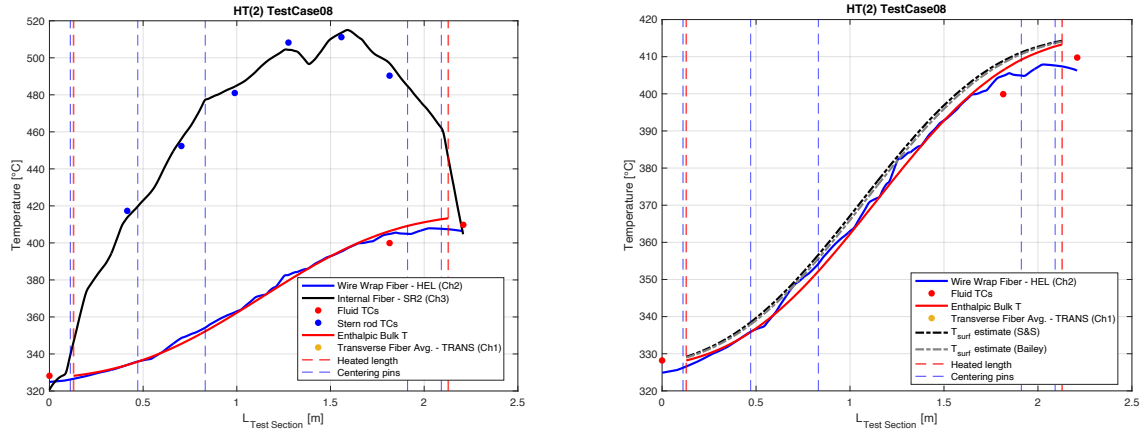

Figure B15: HT(2) Test Case 08 temperatures (Pe = 47, $\dot{q}$ = 7.1 kW).

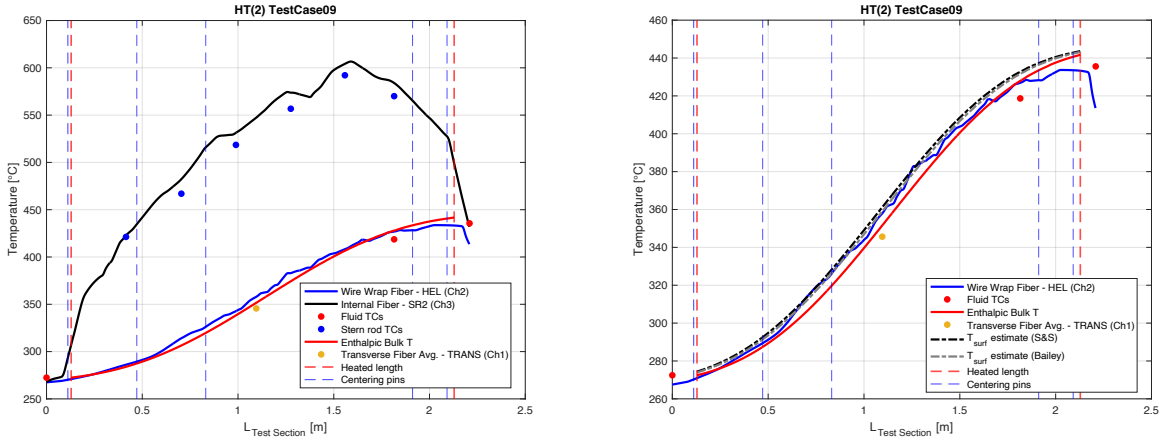

Figure B16: HT(2) Test Case 09 temperatures (Pe = 46, $\dot{q}$ = 13.9 kW).

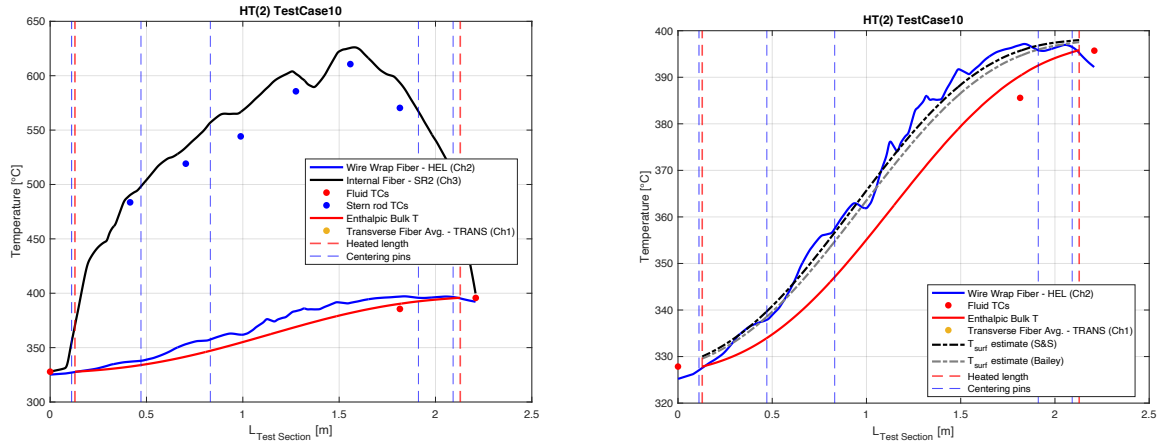

Figure B17: HT(2) Test Case 10 temperatures (Pe = 145, $\dot{q}$ = 17.8 kW).

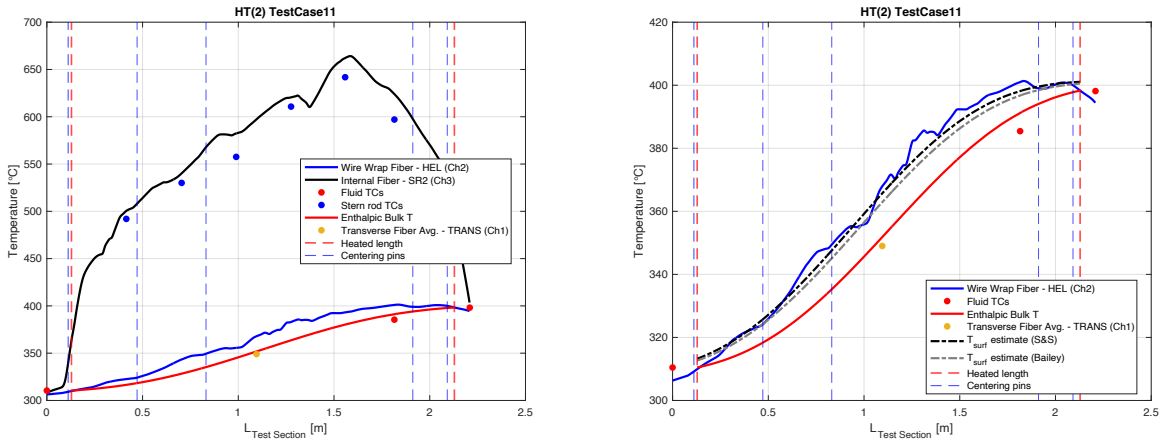

Figure B18: HT(2) Test Case 11 temperatures (Pe = 145, $\dot{q}$ = 23.0).

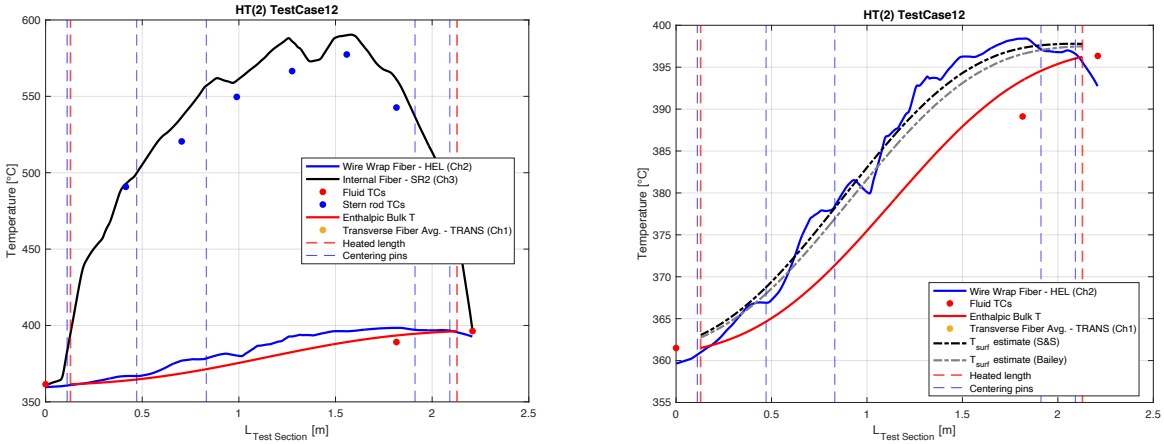

Figure B19: HT(2) Test Case 12 temperatures (Pe = 219, $\dot{q}$ = 13.6 kW).

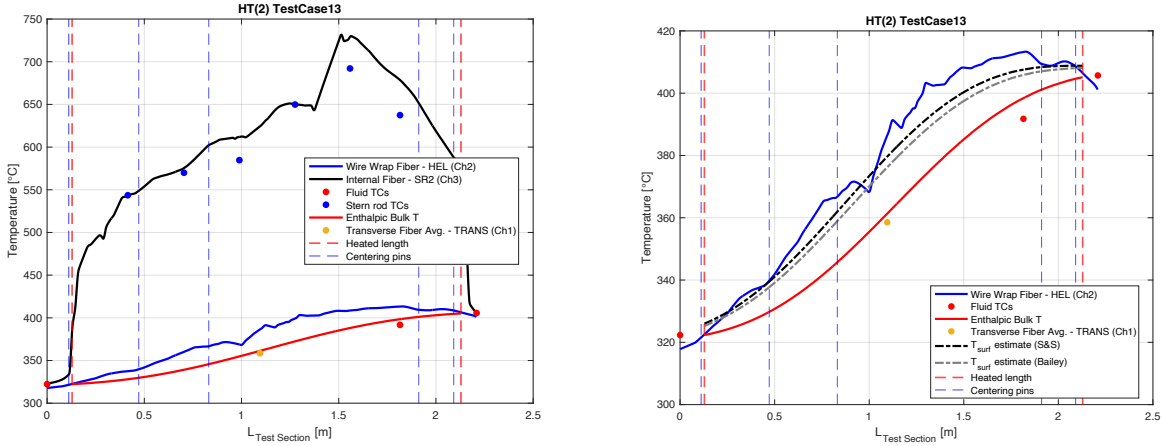

Figure B20: HT(2) Test Case 13 temperatures (Pe = 220, $\dot{q}$ = 32.6 kW).

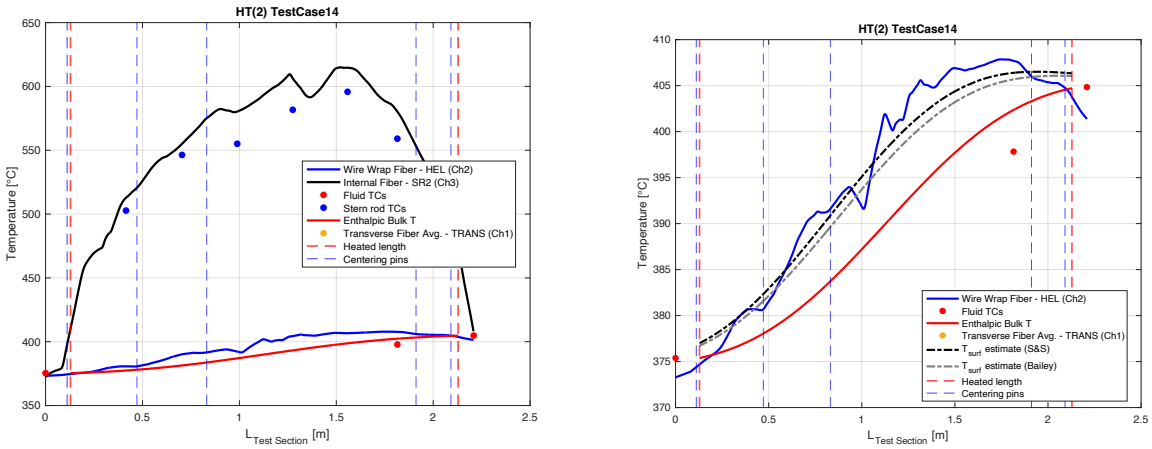

Figure B21: HT(2) Test Case 14 temperatures (Pe = 290, $\dot{q}$ = 15.0 kW).

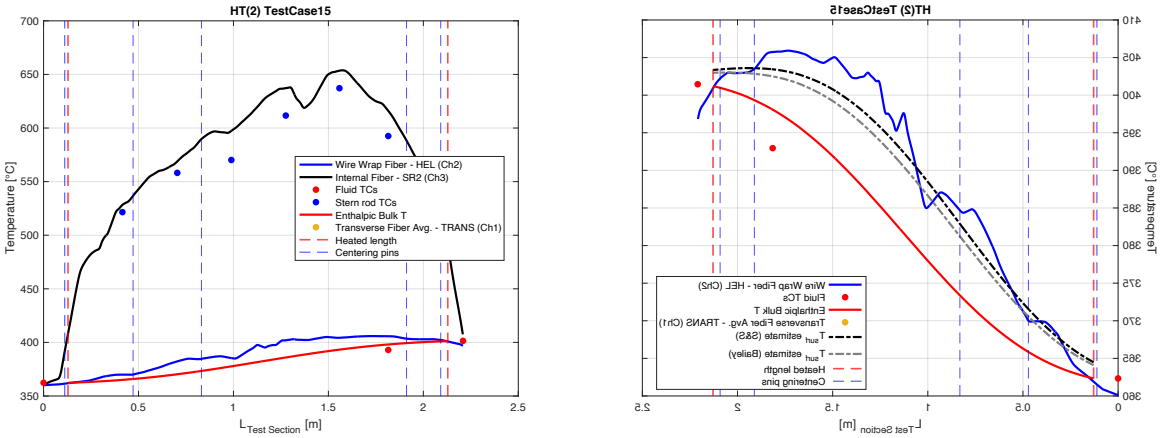

Figure B22: HT(2) Test Case 15 temperatures (Pe = 292, $\dot{q}$ = 20.1 kW).

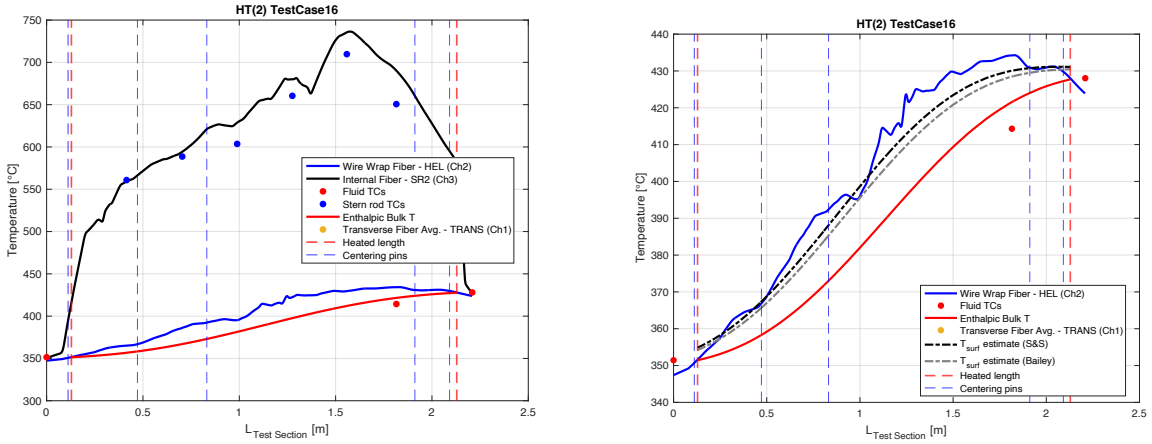

Figure B23: HT(2) Test Case 16 temperatures (Pe = 222, $\dot{q}$ = 29.8 kW).

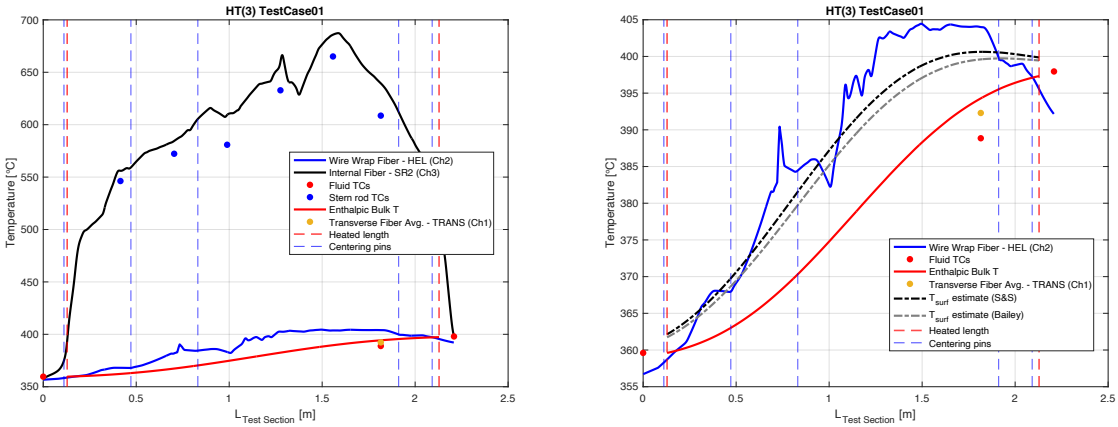

Figure B24: HT(3) Test Case 01 temperatures (Pe = 383, $\dot{q}$ = 25.7 kW).

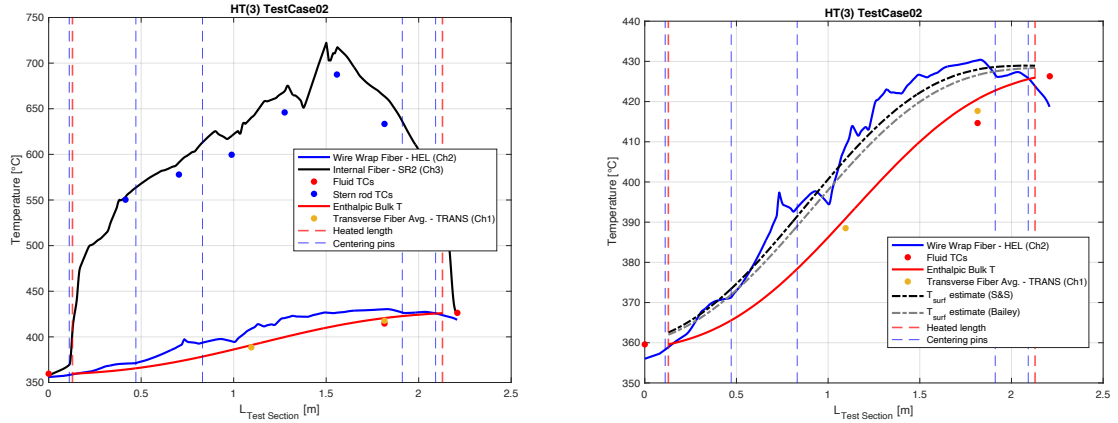

Figure B25: HT(3) Test Case 02 temperatures (Pe = 221, $\dot{q}$ = 25.7 kW).

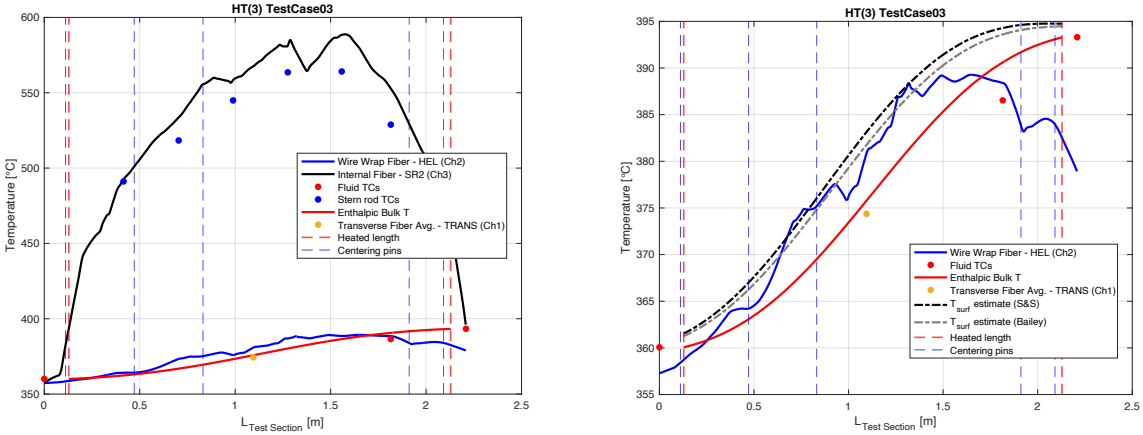

Figure B26: HT(3) Test Case 03 temperatures (Pe = 219, $\dot{q}$ = 13.0 kW).

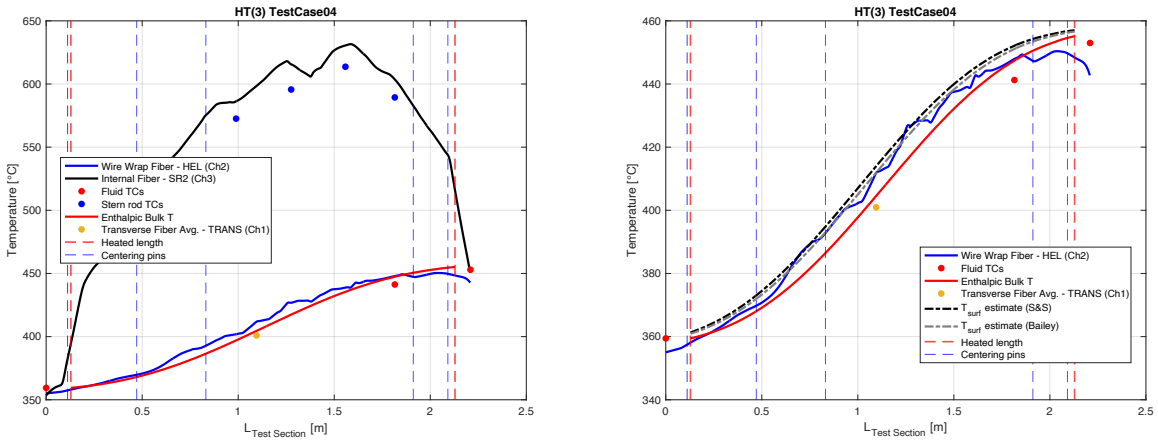

Figure B27: HT(3) Test Case 04 temperatures (Pe = 83, $\dot{q}$ = 13.9 kW).

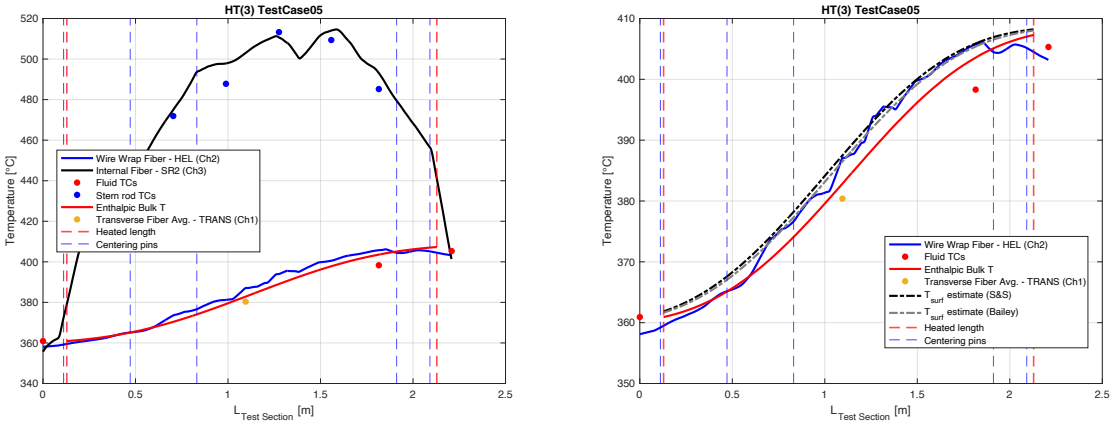

Figure B28: HT(3) Test Case 05 temperatures (Pe = 85, $\dot{q}$ = 7.0 kW).

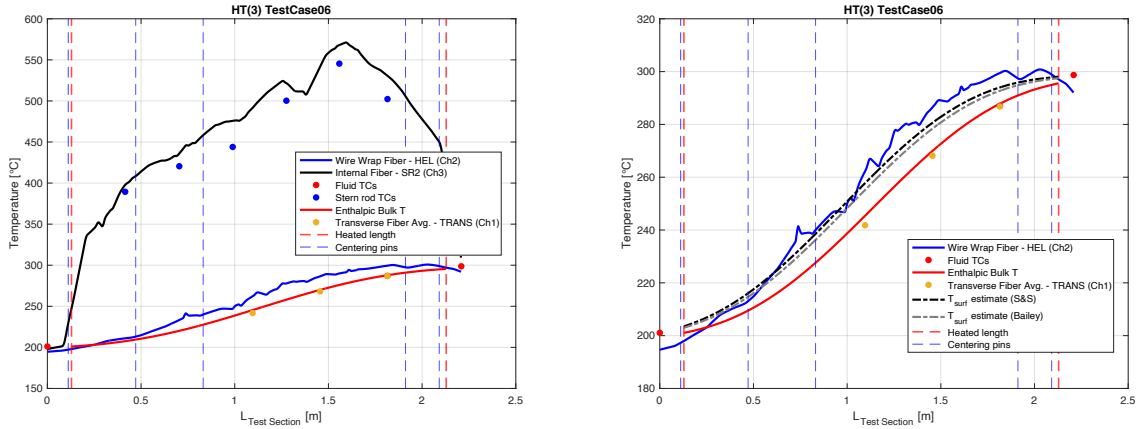

Figure B29: HT(3) Test Case 06 temperatures (Pe = 116, $\dot{q}$ = 21.5 kW).

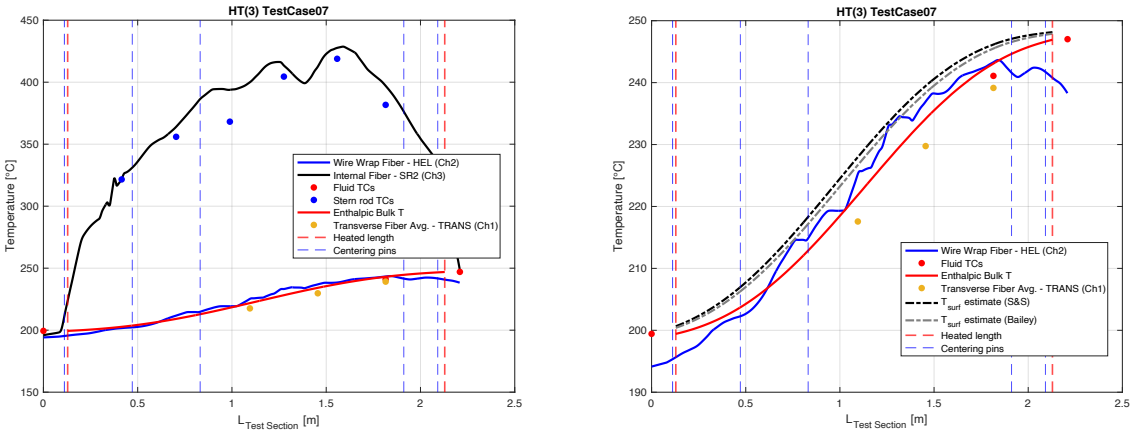

Figure B30: HT(3) Test Case 07 temperatures (Pe = 114, $\dot{q}$ = 10.9 kW).

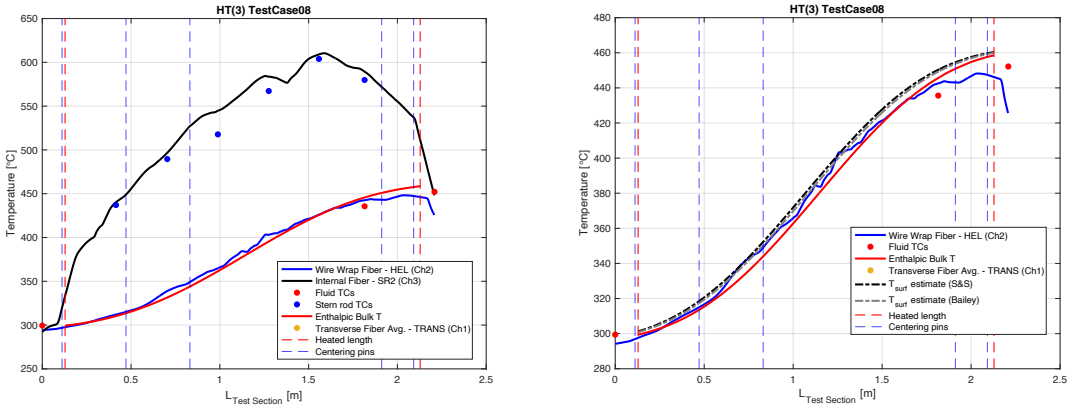

Figure B31: HT(3) Test Case 08 temperatures (Pe = 47, $\dot{q}$ = 13.3 kW).

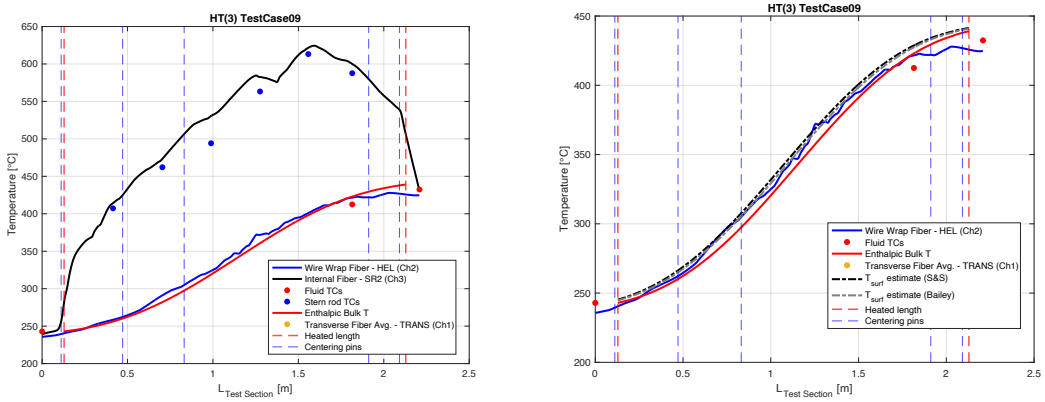

Figure B32: HT(3) Test Case 09 temperatures (Pe = 48, $\dot{q}$ = 17.0 kW).

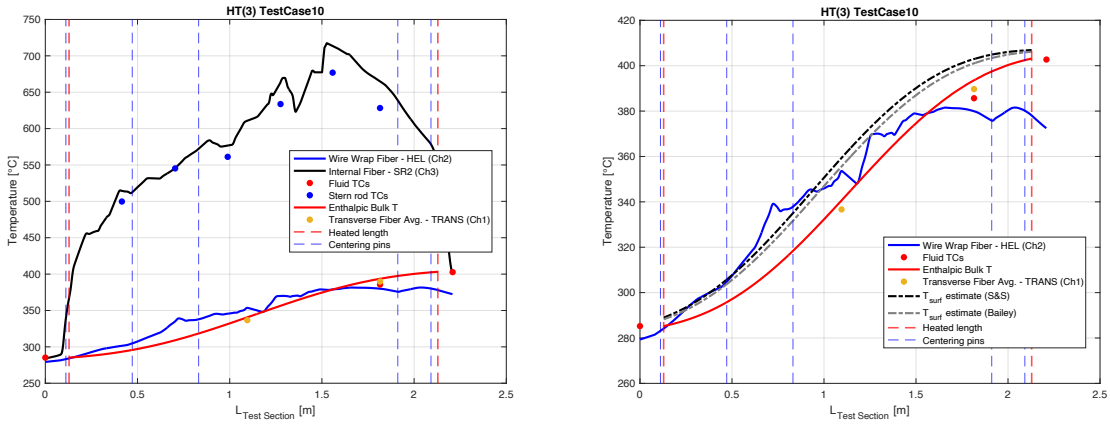

Figure B33: HT(3) Test Case 10 temperatures (Pe = 146, $\dot{q}$ = 31.4 kW).

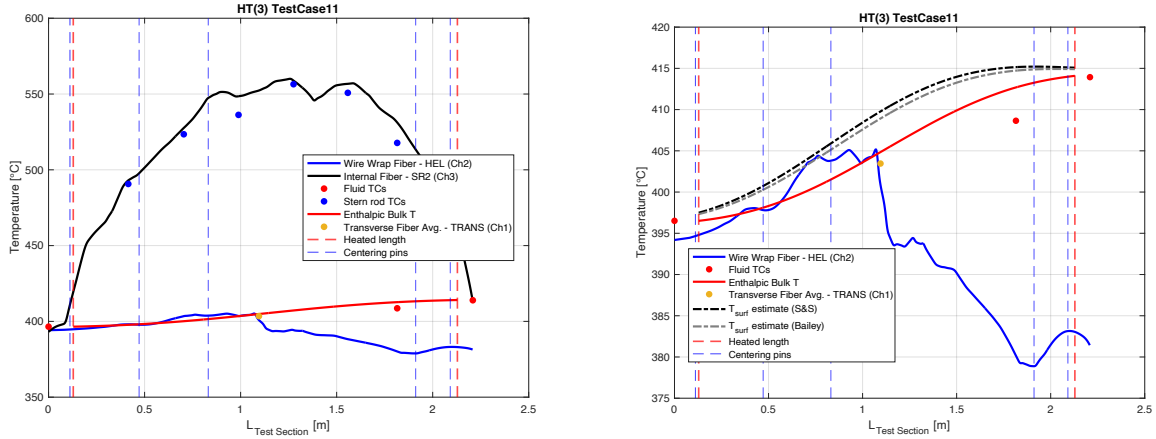

Figure B34: HT(3) Test Case 11 temperatures (Pe = 297, $\dot{q}$ = 9.1 kW).

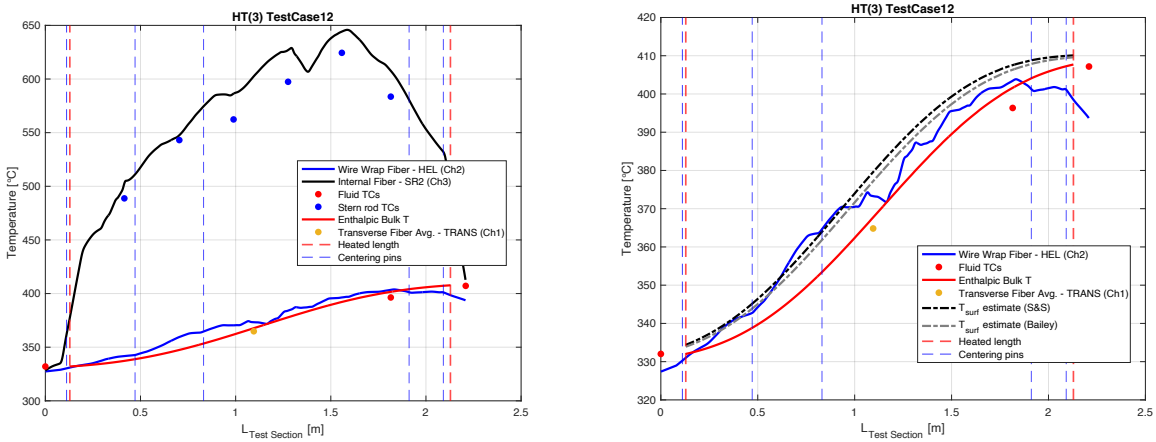

Figure B35: HT(3) Test Case 12 temperatures (Pe = 143, $\dot{q}$ = 19.4 kW).

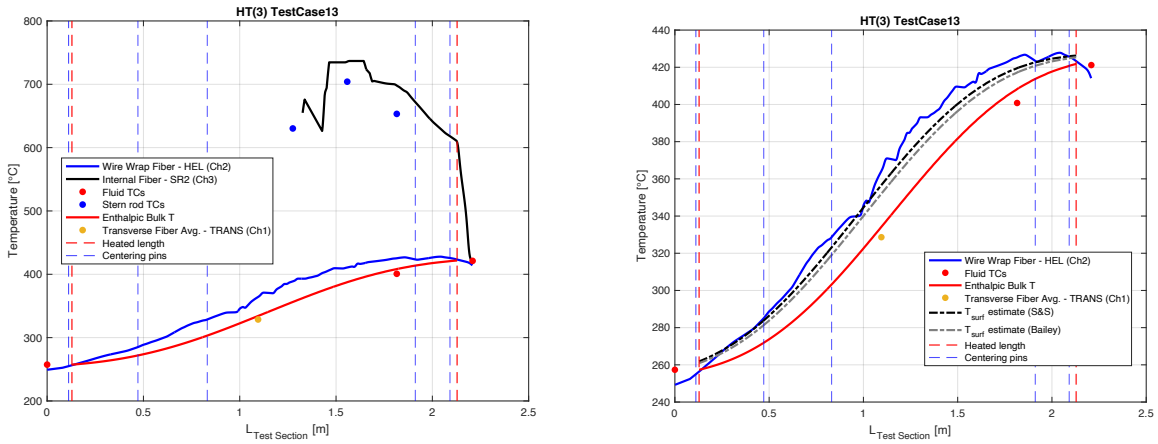

Figure B36: HT(3) Test Case 13 temperatures (Pe = 123, $\dot{q}$ = 36.8 kW).